Materials Science and Engineering R 39 (2002) 143–222

R Reports: *A Review Journal*

www.elsevier.com/locate/mser

Recent progress of molecular organic electroluminescent materials and devices

L.S. Hung[a,*], C.H. Chen[b]

[a]*Center of Super-Diamond and Advance Films (COSDAF) and Department of Physics & Materials Science, City University of Hong Kong, Hong Kong, China*

[b]*Department of Applied Chemistry and Microelectronics & Information Systems Research Center, National Chiao Tung University, Hsinchu 300, Taiwan, ROC*

Abstract

Electroluminescent devices based on organic materials are of considerable interest owing to their attractive characteristics and potential applications to flat panel displays. After a brief overview of the device construction and operating principles, a review is presented on recent progress in organic electroluminescent materials and devices. Small molecular materials are described with emphasis on their material issues pertaining to charge transport, color, and luminance efficiencies. The chemical nature of electrode/organic interfaces and its impact on device performance are then discussed. Particular attention is paid to recent advances in interface engineering that is of paramount importance to modify the chemical and electronic structure of the interface. The topics in this report also include recent development on the enhancement of electron transport capability in organic materials by doping and the increase in luminance efficiency by utilizing electrophosphorescent materials. Of particular interest for the subject of this review are device reliability and its relationship with material characteristics and interface structures. Important issues relating to display fabrication and the status of display development are briefly addressed as well.

Keywords: Electroluminescence; Organic light-emitting devices; Carrier injection; Efficiency; Stability; OLED-based displays

1. Introduction

Organic electroluminescence (EL) is the electrically driven emission of light from non-crystalline organic materials, which was first observed and extensively studied in the 1960s [1,2]. In 1987, a team in Kodak introduced a double layer organic light-emitting device (OLED), which combined modern thin film deposition techniques with suitable materials and structure to give moderately low bias voltages and attractive luminance efficiency [3,4]. Shortly afterwards, in 1990 the Cambridge group of Friend announced a conducting polymer-based LED [5,6]. Since then, there have been increasing interests and research activities in this new field, and enormous progress has been made in the improvements of color gamut, luminance efficiency and device reliability. The growing interest is largely motivated by the promise of the use of this technology in flat panel displays. As a consequence, various OLED displays have been demonstrated. In this article, the reader will find a description of the latest trends in organic EL research covering all the new

* Corresponding author. Present address: Department of Physics and Materials Science, City University of Hong Kong, Tat Chee Avenue, Kowloon, Hong Kong, China. Tel.: +852-2788-7433; fax: +852-2788-7830.
E-mail address: aplshung@cityu.edu.hk. (L.S. Hung).

0927-796X/02/$ – see front matter
PII: S0927-796X(02)00093-1

achievements and most important data, but the description is confined to molecular organic EL materials and devices.

The design of EL materials for used in OLEDs is critical to device performance. Great strides have been made towards the development and improvement of molecular materials for display applications. Intense research in both academia and industry over the last 3–4 years has yielded OLEDs with remarkable color fidelity, device efficiencies and operational stability.

Charge injection and transport are the limiting factors in determining operating voltage and luminance efficiency. In OLEDs, the hole current is limited by injection, and the electron current is strongly influenced by the presence of traps owing to metal–organic interactions. In order to enhance carrier injection the selection of efficiently electron-injecting cathode materials and the use of appropriate surface treatments of anodes are of great importance. The current statues of charge injection and transport will be discussed in this review.

The efficiency of an OLED is determined by charge balance, radiative decay of excitons, and light extraction. Significant progress has been made recently in developing phosphorescent emitters via triplet–triplet energy transfer, and high-efficiency OLEDs in various colors have been demonstrated. Light extraction is determined by the device structure and the refractive indices of the composed layers. Current research activity is directed toward various surface modifications that can increase extraction efficiency, while the problem of light-trapping remains unsolved in terms of its application to displays.

The most critical performance characteristic for OLEDs is the device operational lifetime. Continuous operation of OLEDs generally leads to a steady loss of efficiency and a gradual rise in bias voltages. Although OLEDs have achieved long operational stability, the material issues underlying the EL degradation are not fully understood. There are many studies of degradation process, and an overview will be presented in this article.

The remarkable advance in OLEDs has led to its application to flat panel displays. The promise of low-power consumption and excellent emissive quality with a wide viewing angle is unique among display technologies. At the moment, passive monochrome and multicolor displays are commercially available, and active-matrix full-color displays have been demonstrated. Some important issues relating to display fabrication and the status of display development will also be described.

2. Background

2.1. Device configuration and operation

An OLED has an organic EL medium consisting of extremely thin layers (<0.2 μm in combined thickness) sandwiched by two electrodes. In a basic two-layer OLED structure, one organic layer is specifically chosen to transport holes and the other organic layer is specifically chosen to transport electrons. The interface between the two layers provides an efficient site for the recombination of the injected hole–electron pair and resultant electroluminescence.

When an electrical potential difference is applied between the anode and the cathode such that the anode is at a more positive electrical potential with respect to the cathode, injection of holes occurs from the anode into the hole-transport layer (HTL), while electrons are injected from the cathode into the electron-transport layer (ETL). The injected holes and electrons each migrate toward the oppositely charged electrode, and the recombination of electrons and holes occurs near the junction in the luminescent ETL. Upon recombination, energy is released as light, which is emitted from the light-transmissive anode and substrate.

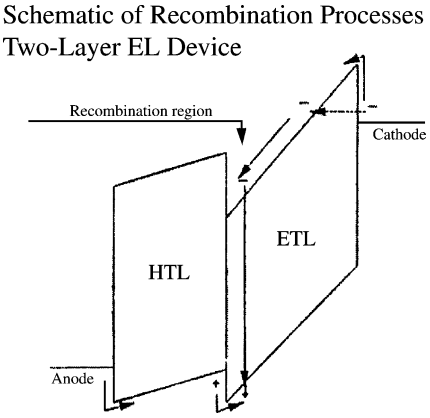

Fig. 1. Energy level diagram of a two-layer OLED.

The heterojunction should be designed to facilitate hole-injection from the HTL into the ETL and to block electron injection in the opposite direction in order to enhance the probability of exciton formation and recombination near the interface region. As shown in Fig. 1, the highest occupied molecular orbital (HOMO) of the HTL is slightly above that of the ETL, so that holes can readily enter into the ETL, while the lowest unoccupied molecular orbital (LUMO) of the ETL is significantly below that of the HTL, so that electrons are confined in the ETL. The low hole mobility in the ETL causes a build up in hole density, and thus enhance the collision capture process. Furthermore, by spacing this interface at a sufficient distance from the contact, the probability of quenching near the metallic surface is greatly reduced.

The simple structure can be modified to a three-layer structure, in which an additional luminescent layer is introduced between the HTL and ETL to function primarily as the site for hole–electron recombination and thus electroluminescence. In this respect, the functions of the individual organic layers are distinct and can therefore be optimized independently. Thus, the luminescent or recombination layer can be chosen to have a desirable EL color as well as a high luminance efficiency. Likewise, the ETL and HTL can be optimized primarily for the carrier-transport property.

The extremely thin organic EL medium offers reduced resistance, permitting higher current densities for a given level of electrical bias voltage. Since light emission is directly related to current density through the organic EL medium, the thin layers coupled with increased charge injection and transport efficiencies have allowed acceptable light emission to be achieved at low voltages.

2.2. Materials

The advantages of organic materials over inorganic materials are their excellent color gamut and high fluorescence efficiency. Light is produced in organic materials by the fast decay of excited molecular states, and the color of light depends on the energy difference between those excited states and the molecular ground level. Many materials show intense photoluminescence with near unity quantum yield, while the EL efficiency is limited by the probability of creating non-radiative triplet exited states in the electron–hole recombination.

Most organic materials support preferentially the transport of either electrons or holes with their mobilities in the range of 10^{-8} to 10^{-2} $cm^2/(V\ s)$. Electron mobility in organic materials is generally orders of magnitude lower than hole mobility. The most important electron-transport material is tris(8-hydroxyquinolinato)aluminum (Alq_3) with its molecular structure shown in Fig. 2, and the

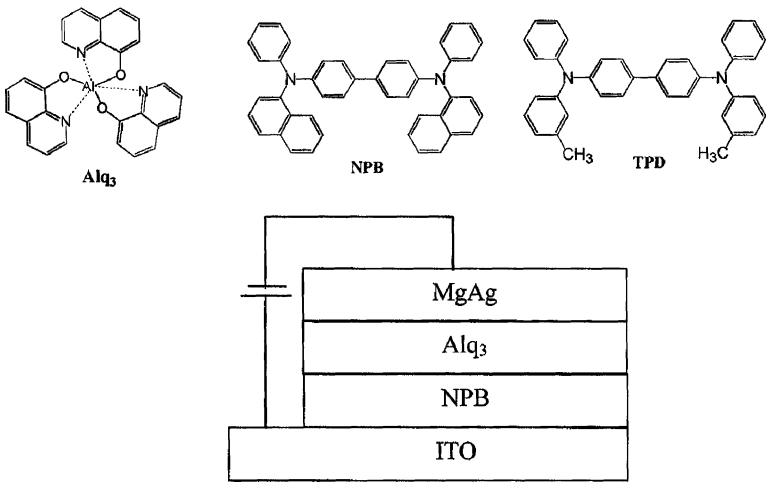

Fig. 2. Common electron and hole-transport materials and a two-layer OLED.

electron mobility in Alq_3 strongly depends on electric field with a value of approximately 10^{-6} cm^2/(V s) at 4×10^5 V/cm. Alq_3 is also used as an emissive material, which emits in the green with a broad emission peaking at 530 nm. Other EL colors can be obtained by doping a small amount of specific guest molecules in Alq_3 or by choosing different organic fluorescent materials as emitters. In some cases, doping also enhances luminance efficiency by reducing non-radiative decay.

There are several materials that have been preferred as hole-transport materials (HTMs). Among them, *N*,*N*′-diphenyl-*N*,*N*′-bis(3-methylphenyl)(1,1′-biphenyl)-4,4′-diamine (TPD) and *N*,*N*′-bis(l-naphthyl)-*N*,*N*′-diphenyl-1,1′-biphenyl-4,4′-diamine (NPB) have been studied extensively. The hole-transport materials in Fig. 2 have a glass transition temperature below 100 °C and a hole mobility in the range of 10^{-3} to 10^{-4} cm^2/(V s). In OLEDs, the hole current dominates the total current, owing to efficient hole-injection and sufficiently high hole mobilities.

A barrier for electron injection is commonly present at the metal–organic contact when the work function of the metal is larger than the LUMO of the organic materials, and thus the use of a low-work function metal is highly desirable to facilitate the injection of electrons. Mg alloyed with a small amount of silver is a commonly used cathode. Mg is a relatively stable metal with a work function of 3.66 eV, which is sufficiently low for it to be useful as an electron-injecting electrode. The small amount of Ag assists the Mg deposition by presumably providing nucleating sites on the alloyed film during co-sublimation.

The hole-injecting contact requires a metal of high work function to match with the HOMO of the organic material. All OLEDs rely on the transparent and conductive indium tin oxide (ITO) as the anodic material to facilitate hole-injection while permitting light to exit the device in an effective manner. The work function of ITO ranges from 4.5 to 5.0 eV, strongly depending on the methods of surface treatment. Treatments of ITO glass substrates using UV ozone or oxygen plasma substantially increase its work function and consequently enhance hole-injection from the ITO anode into the HTL.

2.3. Device preparation

Vacuum evaporation by resistive heating is most appropriate for depositing molecular materials. Organic vapor phase deposition (OVPD) has also been demonstrated to deposit organic materials on large substrates [7]. It is also common to deposit cathode materials using the same vacuum

evaporation from filaments. For the deposition of high-temperature metals one may employ e-beam evaporation or sputtering. The latter is particularly useful for large substrates and high throughput production. However, OLEDs are extremely sensitive to radiation, and special care needs to be taken. In e-beam deposition, a magnetic field is applied across the substrate to repel electrons and ions. In sputter deposition, a buffer layer is required to minimize the radiation damage inflicted on the OLED organic layer stack.

Typical device fabrication occurs by the following sequence: devices are grown on glass slides pre-coated with transparent ITO with a sheet resistance of 15–100 Ω/□. Substrates are ultrasonically cleaned in detergent solution, followed by thorough rinsing in deionized water. They are then cleaned in organic solvents and dried in pure nitrogen gas. After cleaning, the ITO glass is subject to an oxygen treatment either using UV ozone or oxygen plasma to enhance hole-injection. Single heterostructure devices (Fig. 2) are formed by sequential high vacuum (10^{-5} to 10^{-6} Torr) vapor deposition of a hole-transport layer such as NPB, followed by an electron-transport layer of Alq_3, previously purified by temperature gradient sublimation. Deposition is carried out by thermal evaporation from a baffled Ta crucible at a nominal deposition rate of 0.2–0.4 nm/s. An electron-injecting electrode of approximately 10:1 Mg:Ag volume ratio is subsequently deposited by co-evaporation from separate Ta boats at a vacuum of 10^{-5} Torr. The device preparation is completed with encapsulation in a dry argon box.

OLEDs are constructed using glassy and amorphous organic films and thus provide significant advantages in device fabrication and cost reduction. They are pronouncedly different in structures from inorganic LEDs consisting of epitaxial semiconductor thin films.

2.4. Analytical tools

2.4.1. Electrical and optical properties

Absorption, excitation and luminescence spectra are determined with a spectrophotometer. Current–voltage and luminance–current characteristics are measured by using a radiometer and a digital voltmeter. Typical current–voltage and luminance–current characteristics of a device with 75 nm of NPB, and 70 nm of Alq_3 are shown in Fig. 3. The voltage required for light emission is strongly dependent on the thickness of the Alq_3.

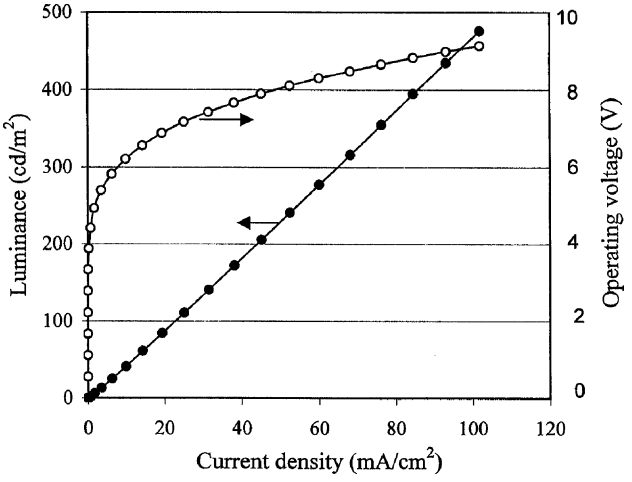

Fig. 3. Luminance and operating voltage vs. current density measured on an Alq_3-based OLED.

In OLEDs we distinguish the quantum efficiency (η) and the luminous efficiency (η_p). The quantum efficiency η is defined as the ratio of the number of emitted quanta to the number of charge carriers. Quantum efficiency is an important quantity, which reflects the comprehensive result of the EL process, but the luminous efficiency has a more technical significance, which is the ratio of the luminous flux emitted by the device and the consumed electric power.

2.4.2. Metal–organic interfaces

Ultraviolet photoelectron spectroscopy (UPS) and X-ray photoelectron spectroscopy (XPS) are commonly used to determine the nature of the metal–organic interfaces [8]. Samples are illuminated with light, and the kinetic energy distribution of photogenerated electrons is analyzed. With a relatively low photon energy of 21.2 eV, UPS is employed to measure the ionization potential of organic materials and the work function of metals. With relative high photon energy in the range of 1 keV, XPS is employed to determine the elements present in the near surface region and provides subtle information on chemical bonding.

2.4.3. Carrier mobilities

Both time-of-flight (TOF) and transient EL are utilized to measure carrier mobilities [9,10]. The TOF method determines the flight time, which is needed for single sign charges generated near one surface of a sample to move across the sample to the other side. A short pulse of strongly absorbed light generates the free charge carriers. The sample is sandwiched between two electrodes (one semitransparent) to allow application of a constant electric field. In transient EL analysis, EL from a testing OLED is investigated with the materials of interest as a carrier-transport layer. Using a voltage pulse as an excitation source, the delay time for the EL is measured and interpreted as the carrier transit time across the carrier-transport layer.

3. Molecular organic electroluminescent materials

The phenomenon of organic electroluminescence was first discovered by Pope in 1963 [11]. But, the development of organic light-emitting device (or diode) known as today's OLED technology actually began in the Chemistry Division of Kodak Research Laboratories in the late 1970s by Tang and coworkers. Their research led eventually to the discovery of the first efficient multi-layered organic electroluminescent device based on the concept of the heterojunction architecture [12,13] which was followed by the disclosure of the doped emitter using the highly fluorescent organic dyes for color tuning and efficiency enhancement [14,15]. Since then, tremendous progress has been made in the field of organic electroluminescence, particularly in recent years and commercialization activity is well underway. One of the key enablers in the history of OLED advancement can be attributed to the continuing discovery of new and improved electroluminescent materials which were made possible by the dedication and ingenuity of many organic chemists who provide the design and skilled synthesis. Indeed, from small molecules, oligomers to conjugated polymers, intense research in both academia and industry has yielded OLEDs with remarkable color fidelity, device efficiencies and operational stability.

This part of the review is written primarily from an organic chemist's perspective highlighting some of the most significant development of small molecular materials published in the last three years (through 2001). These will include the coverage of hole-injection, hole transport, electron transport and host emitting materials as well as RGB and miscellaneous fluorescent dopants. At the end of this section, a special section is devoted to the progress made on the triplet emitter harvesting

the organic phosphorescent emission. For complementary readings, the readers are referred to two recent review articles published in January and June of 2000 by Shirota [16] on *Organic materials for electronic and optoelectronic devices* and by Mitschke and Bauerle [17] on *The electroluminescence of organic materials*, respectively. For the sake of continuity, several representative reviews prior to 1999 are cited here for further reference [18–24]. For readers who are more interested in polymeric electroluminescent materials whose design features in certain respects are similar to those of small molecules, a fair number of excellent reviews are also included in the reference section [25–28].

3.1. Hole-injection materials

Oxidation of the ITO surface by O_2 plasma, CF_4/O_2 plasma [29] or UV ozone treatment can reduce the carrier injection energy barrier, remove residual organic contaminants and get its work function up to near 5 eV which is still about 0.5 eV lower than most of the HOMO of the hole-transport materials. A layer of hole-injection material (sometimes referred to as ITO or anode buffer layer) which reduces the energy barrier in-between ITO/HTL is therefore beneficial to enhancing charge injection at the interfaces and ultimately improving power efficiency of the device. Thus, hole-injection can be promoted by introduction of new hole-transport layers with optimized HOMO levels and by inserting a thin layer of copper phthalocyanine (CuPc) [30], starburst polyamines [31], polyaniline [32,33] and SiO_2 [34] between the ITO/HTL interface. In addition, HTLs doped with oxidizing agents such as $FeCl_3$ [35], iodine [36], tetra(fluoro)-tetra(cyano)quinodimethane (TF-TCNQ) [37] and tris(4-bromophenyl)aminium hexachloroantimonate (TBAHA) [38] have been reported as effective materials for hole-injection (see examples in Fig. 4). The latter can also be dispersed in a polymeric matrix to improve surface roughness as well as thermal stability [39]. One of the widely used polymers for promoting hole-injection is poly(3,4-ethylenedioxythiophene)–poly(styrene) known as PEDOT/PSS which has been found to be useful in a hybrid OLED architecture combining both the advantages of polymer LED (PLED) and multi-layered small molecule OLED [40]. PEDT/PSS is an aqueous gel dispersion. The hydrated gel particles are formed by PSS interlinked by PEDT chains. Like CuPc, PEDOT/PSS as hole-injection layer can smooth the ITO surface, reducing the probability of electrical shorts, decreasing the turn-on voltage and prolonging the operation lifetime of the device [41]. One of the potential drawbacks of using PEDOT/PSS is its acidity which could get as high pH as $\sim$3. However, by modifying particle size distribution and increasing the materials resistivity, a new formulation promoted by Bayer AG is reported to be able to reduce crosstalk in passive-matrix OLEDs [42].

Nuesch et al. found that surface treatment using grafting of molecules [43] and adsorption of acids or bases [44] on ITO could also modify its work function. In the case of 2-chloroethylphosphonic acid, a self-assembled monolayer (SAM) can be readily formed on the ITO substrate which significantly reduced the threshold voltage of a standard OLED device of [ITO/TPD/Alq_3/Al] [45]. Later, it was found by using polar adsorbate molecules with the dipole oriented outward from the surface, an artificial dipolar layer was formed and the work function is increased. With this method the threshold voltage for light emission could be reduced by 4 V and the maximum luminance increased by a factor of 3.5, giving an overall performance superior to that using the stable Mg:Ag counter electrode [46].

Recently, p-doped aromatic diamines have been found to be excellent injection materials such as $SbCl_5$-doped *N*,*N*′-bis(*m*-tolyl)-1,1′-biphenyl-4,4′-diamine (TPD) thin film [47] as well as the amorphous starburst amine, 4,4′,4″-tris(*N*,*N*-diphenylamino)triphenylamine (TDATA) doped with a very strong acceptor TF-TCNQ by controlled co-evaporation [48]. Multi-layered OLEDs consisting of [ITO/TF-TCNQ (2%):TDATA (100 nm)/TPD (10 nm)/Alq_3 (65 nm)/LiF (1 nm)/Al] achieved a

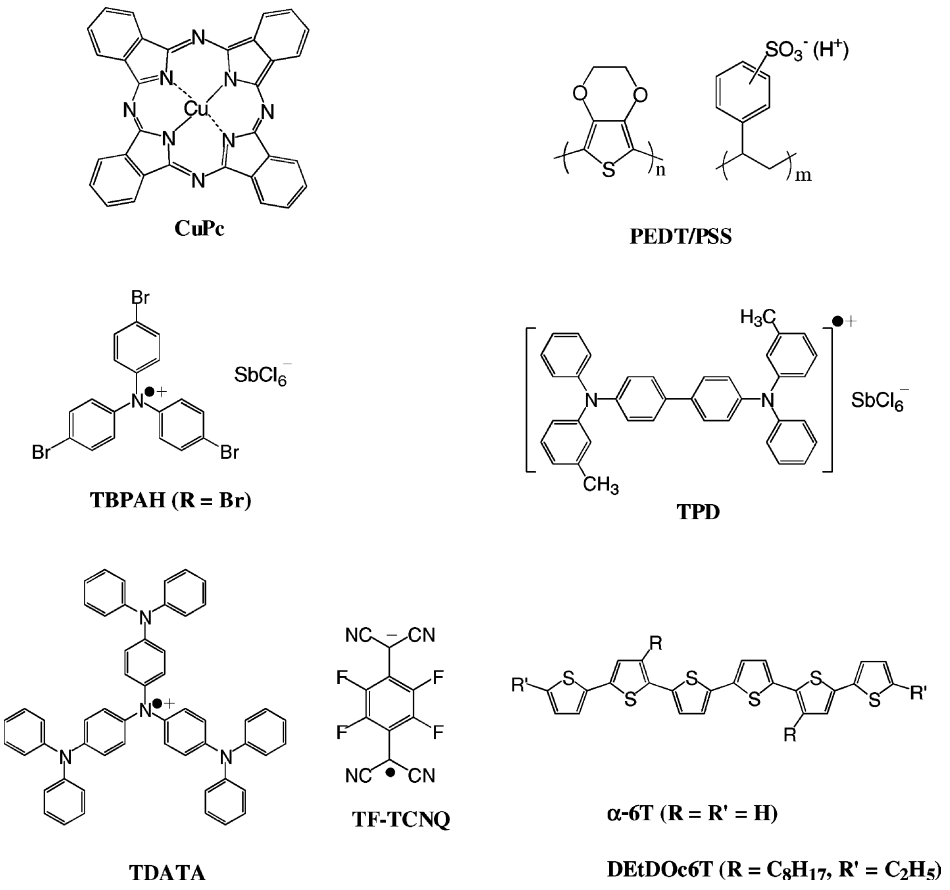

Fig. 4. Hole-injection materials.

very low operating voltage of 3.4 V for obtaining 100 cd/m^2 at 9.1 mA/cm^2. Another notable example of an anode buffer layer is α-sexithiophene (α-6T) which at an optimal thickness of 60 nm has been shown to improve EL efficiency and lower operating voltage [49]. Since the oxidation potential of oligothiophenes can be readily tuned by lengthening π-conjugation and by regiospecific substitution, e.g. DetDOc6T [50], the doped oligothiophenes can also be expected to be useful as injection materials for electroluminescence.

3.2. Hole-transport materials

Ever since the discovery of using *tri*-arylamines with a "*bi*-phenyl" center core as the hole-transport layer which greatly improved both EL efficiency and operational stability of OLED [51], most of the new HTM developed seemed to have all evolved around this theme. The creativity of synthetic chemists as well as material scientists throughout the world continue to provide the OLED device community with their ever improved products having superb properties and elegant design. By far, one of the most widely used HTM in OLED is still NPB. One of the reasons for its popularity is because sublimed NPB can be manufactured readily and is thus abundantly available even though its T_g at 98 °C is a trifle low which may affect its morphological stability at high operating temperature. Therefore, studies on the design and synthesis of new HTMs have been continually focused on finding materials with high thermal and thin film morphological stabilities and on finding

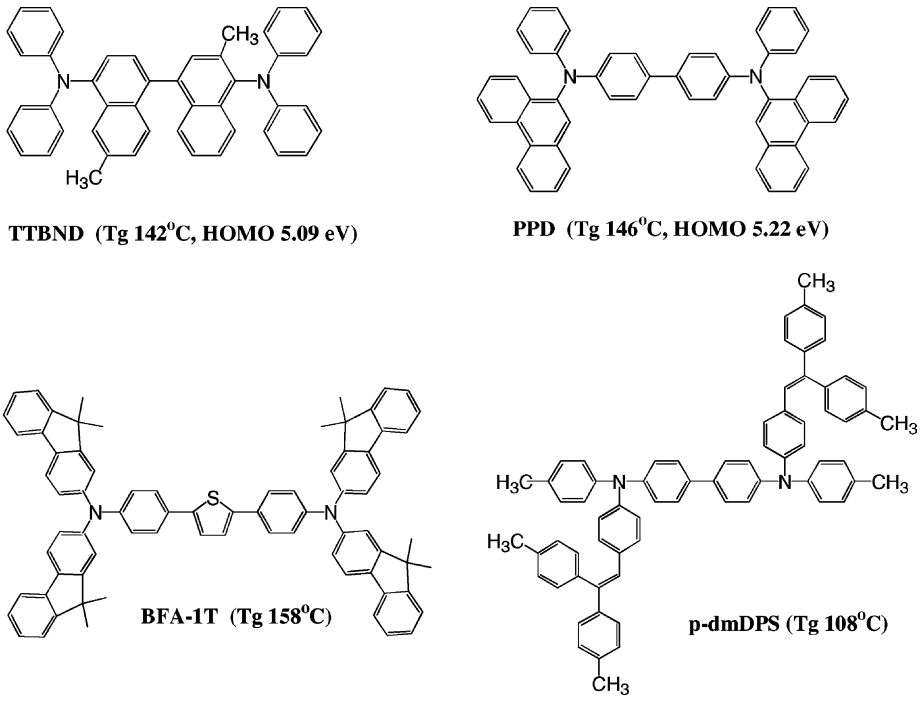

Fig. 5. Biphenyl diamine derivatives.

ways to control and optimize carrier injection and transport. These approaches to molecular design can be roughly categorized into biphenyl diamine derivatives; starburst amorphous molecular glass; *spiro*-linked biphenyl diamines and miscellaneous examples as follows:

1. *Biphenyl diamine derivatives*: Heat treatment of organic multi-layers has been found to cause an interdiffusion between organic layers in OLED [52] which ultimately effects the stability of the device. Therefore, to increase the T_g of HTM is critical in obtaining a more thermally durable display. Using thermodynamical consideration, Sato has proposed a molecular design rule according to which high T_g materials can be obtained by increasing the number of π-electrons and by decreasing rotational moment by placing a heavy moiety at the center of the molecule [31]. Fig. 5 shows the various structures of HTMs with a biphenyl diamine related core along with its reported T_g (°C) and I_p (eV) values for comparison [53,54]. Another variation of NPB is to substitute α-naphthyl with distyryl groups as in *p*-dmDPS [55] which has a T_g of 108 °C and showed an enhanced luminance and improved *I–V* characteristics in the presence of CuPc as hole-injection layer in a device consisting of [ITO/CuPc (10 nm)/HTM (50 nm)/Alq_3 (50 nm)/LiF/Al].
2. *Starburst amorphous molecules*: The formation of pinhole free thin film morphology can be assured if the HTMs can form stable amorphous glasses with high T_gs. The guidelines for the design of amorphous molecular materials as provided by Shirota et al. [56] are: (1) to increase the number of conformers together with non-planar molecular structure; (2) to introduce bulky and heavy substituents as to enlarge molecular size for attaining and maintaining the stability of the glassy state; (3) to increase T_g by the incorporation of a rigid moiety or an intermolecular hydrogen bonding site into non-planar molecules and by increasing the molecular weight. Based on these guidelines, Fig. 6 shows the various general molecular structures that have been synthesized in the laboratory of Shirota. This can be exemplified by the glass of *p*-MTDAB which

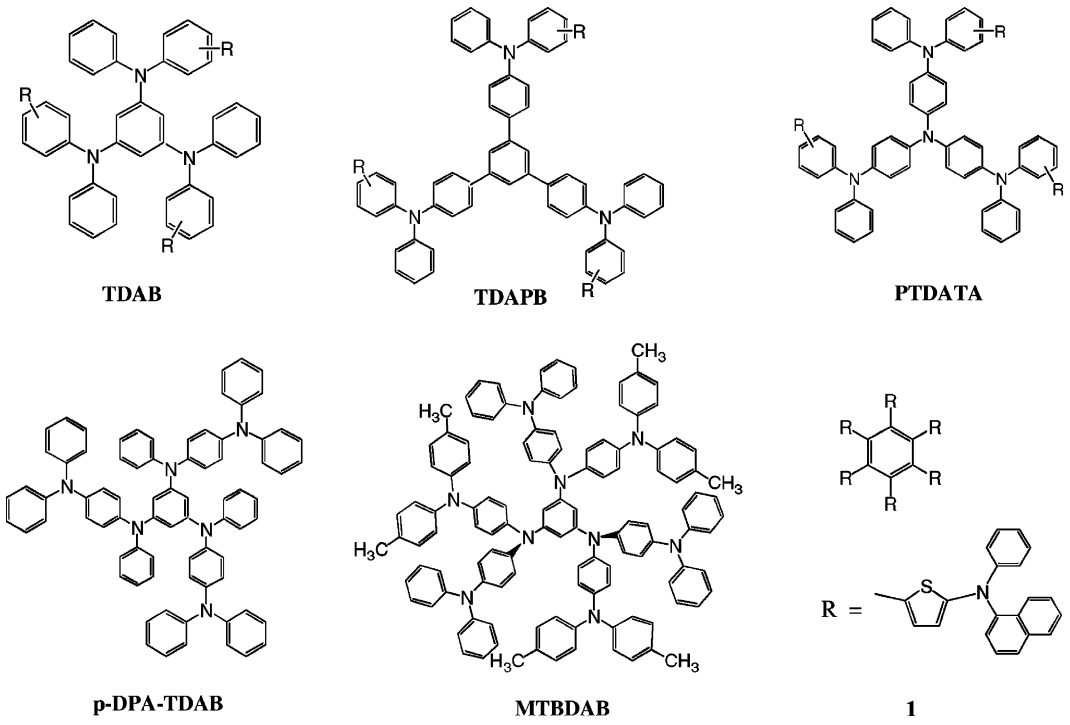

Fig. 6. Starburst amorphous hole-transport materials.

tends to crystallize in several months on standing whereas the amorphous glasses of *p*-DPA-TDAB and MTBDAB are very stable without any crystallization even on heating above their T_gs. A similar idea has been expanded by using a π-rich thiophene system coupled onto the benzene nucleus [57,58]. In Tao's approach, e-rich thienyl ring [59] next to the nitrogen atom can effectively lower the oxidation potential of HTM which could be useful for mediating hole-injection in a double HTL device [60]. In *hexakis*[(diarylamino)thienyl]benzene (**1**) shown in Fig. 2, it is worth noting that it was synthesized in one scoop by a palladium-catalyzed six-fold arylation of hexabromobenzene using Stille's cross-coupling reaction in good yield.

3. *Spiro-linked molecules*: The concept of enhancement of thermal stability of the amorphous state of HTMs and augmentation of T_gs has been introduced by Salbeck et al. [61] via a spiro center with a 90 °C molecular architecture. It has been shown by TOF technique that *spiro*-linked HTM such as *spiro-m*TTB shown in Fig. 7 increased hole mobility [62] and improved EL performance [63] as compared to the parent non-*spiro* analogs. The advantage of T_gs and other thermal properties and solid PL are compared in Table 1.

   An unsymmetrical *spiro*-compound with a high T_g of 122 °C (shown as *spiro*2) [64] can be synthesized by coupling 2,7-bis(diphenylamino)-9-fluorene with 2-lithio-4,4′-di(*t*-butyl)biphenyl, followed by acid-catalyzed *spiro*cylization of the resulting alcohol [65]. In a device structure of [ITO (160 nm)/HTM (60 nm)/Alq_3 (60 nm)/LiF (0.5 nm)/Al (150 nm)], *spiro2* reached a luminance efficiency of 6.1 cd/A and 3.6 lm/W at a drive voltage around 6 V and a luminance of 300 cd/m^2. The authors attributed the enhancement of its EL efficiency to the extreme non-planar conformation and steric hindrance which are effective in suppressing exciplex formation in the two-layer device.

4. *Miscellaneous examples* (Fig. 8): HTM can also serve as the emissive material in a two-layer OLED device if the exciton can be generated in the HTL. The fluorescent pyrene-substituted

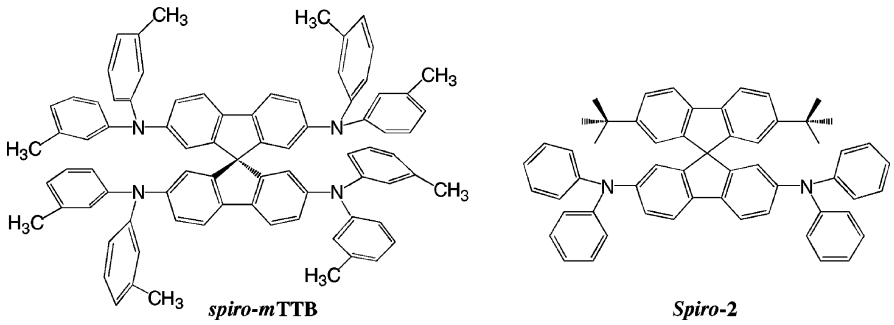

Fig. 7. Example of *spiro*-linked hole-transport materials.

Table 1
Comparison of thermal and solid PL properties of *spiro*-HTMs with NPB

HTM	NPB	*Spiro*-NPB	*Spiro*-TAD
Molecular weight	588.8	1185.5	985.3
T_g (°C)	98	147	133
T_m (°C)	290	294	276
T_{sublim} (°C at 4×10^{-5} mbar)	310	430	355
λ_{max} (PL film)	440	450	405

carbazole derivative **2** (T_g 184 °C), which can be synthesized in high yield by palladium coupling reaction between *N*-(pyrenyl)aniline and 3,6-dibromocarbazole using tris(dibenzylideneacetone)dipalladium ($Pd(dba)_2$) catalyst [66] and a sterically hindered ligand P(*t*-Bu)$_3$ in the presence of sodium *t*-butoxide in reluxing toluene displayed a green emission at 530 nm. Later it was found 2-(di-*tert*-butylphosphino)-*o*-biphenyl was a better ligand than P(*t*-Bu)$_3$ to promote the palladium-catalyzed amination of aryl halides and sulfonates for the synthesis of unsymmetrical triarylamines [67]. Their device had a two-layer structure of [ITO/HTM (50 nm)/TPBI (50 nm)/Mg:Ag] in which TPBI [1,3,5-tris(*N*-phenylbenzimidazol-2-yl)benzene] served as electron-transport layer [68] as it is a more effective hole blocker than Alq_3 to confine the charge recombination in the HTL [69]. Efficient blue-green emission with $\lambda_{max} = 490$ nm from hole transporting dibenzochrysene derivatives (DBC) [70] has been observed in a device of [ITO/DBC (60 nm)/Alq_3 (60 nm)/LiF (0.5 nm)/Al (150 nm)]. Closer examination of their reported EL spectra in which there was a shoulder near 530 nm tailing into 600 nm revealed that the green portion of the emission could conceivably originate from charge recombination in the e-transport Alq_3 layer. This is another piece of evidence of the bipolar nature of Alq_3 which transports

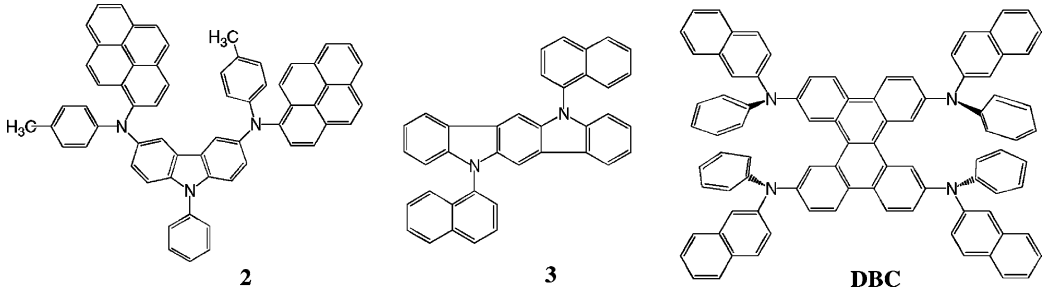

Fig. 8. Miscellaneous hole-transport materials.

electrons but does not appear to block holes as effectively as TPBI. In addition, Popovic and coworkers at Xerox [71] showed rather convincingly that holes injected into Alq_3 which are trapped to form radical cations $[Alq_3]^{+\bullet}$ could be one of the major causes for device degradation. In their experiments [72], a dual-layer device with rubrene doping in both hole-transport NPB and electron-transport Alq_3 showed extrapolated life of over 50,000 h at the current density of 25 mA/cm^2 and an initial luminance of 100 cd/m^2, that is 100× better than the device without doping. The same authors have recently confirmed that the increase in OLED stability by means of doping the HTL is found to be associated with changes in bulk HTL properties rather than interfacial properties, in agreement with the OLED degradation mechanism based on the instability of the Alq_3 cationic species [73]. Further studies using time-resolved fluorescence measurements [74] show that the decrease in the PL quantum efficiency is associated with a decrease in the lifetime of the Alq_3 excited states, thus revealing the nature of the degradation products as luminescence quenchers.

High T_g HTMs based on 5,11-(diaryl)indolo[3,2-*b*]carbazoles (**3**) have been reported by Hu et al. [75] with one of the best derivatives **2** having a T_g of 164 °C as shown in Fig. 3. Finally, it is worth noting that TPD, a morphologically unstable HTM with a low T_g can be dispersed up in concentrations to 75 wt.% into the high T_g transparent polymers to form solid solutions which can be spin-coated as thin films (80 nm) and used as thermally and morphologically stable HTL [76].

3.3. Electron-transport and host emitting materials

To date, the most widely used electron-transport and host emitting material in OLEDs is still Alq_3. This is because Alq_3 is thermally and morphologically stable to be evaporated into thin films, easily synthesized and purified, molecularly shaped to avoid exciplex formation (e.g. with NPB at the interface), and green fluorescent to be a good host emitter. Arguably, it is still one of the most robust electron-transport backing layers in OLED, particularly with the help of the hole blocker to trap the hole carriers from injecting into Alq_3 [77] or doping with lithium or other alkali metals [78] to assist electron injection to lower the drive voltage [79]. But, it has also many shortcomings such as quantum efficiency, mobility, bandgap and the ashing problem during sublimation. Studies toward the understanding of its molecular packing [80], photodegradation [81], electron drift mobility [82], transport phenomenon [83], excited state [84], fluorescence by ZINDO calculation [85] and electric field-dependent quenching of EL [86] are continuing. It has been found by the time-of-flight technique that the drift mobility of electrons in Alq_3 is increased by about two orders of magnitude (to 10^{-4} cm^2/(V s)) as the deposition rate decreased from 0.7 to 0.2 nm/s. The electron drift mobility in Alq_3 is found to increase linearly with the square root of the applied electric field.

There were also attempts to improve the quantum efficiency, thermal stability and thin film morphology of Alq_3 by structural modifications as shown in Fig. 9. Tris(5-hydroxymethyl-8-quinolinolato)aluminum (AlOq) [87] was reported to form a more uniform amorphous thin film than Alq_3 by slow vacuum deposition and the device [ITO/PVK/AlOq/Al] also emitted green light with better efficiency. This improvement was attributed to the hydroxymethyl groups attached to the C-5 positions of quinoline which, due to intermolecular hydrogen bondings, could lead to the formation of super molecular structures in AlOq thin film. An unsymmetrically substituted bis(5,7-dichloro-8-quinolinolato)-(8-quinolinolato)aluminum ($Alq(Clq)_2$) [88] was prepared by first reacting 8-hydroxyquinoline and triethylaluminum in refluxing benzene to form $Alq(C_2H_5)_2$ as a yellow solid which could be further reacted with 2 eq. of 5,7-dichloro-8-quinoline to precipitate the product in 61% yield. The emission of $Alq(Clq)_2$ is slightly bathochromicly shifted from that of Alq_3.

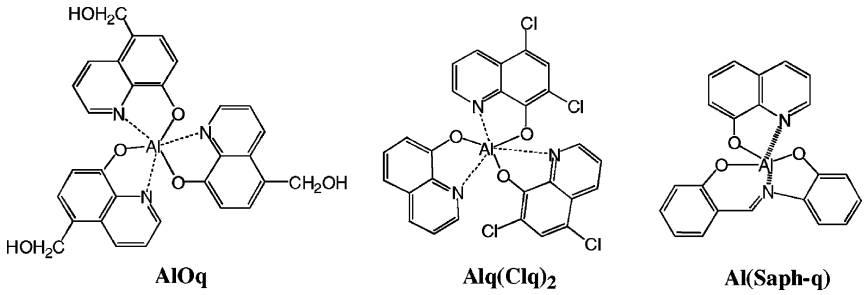

Fig. 9. Modified Alq_3 molecules.

Comparison of the EL λ_{max} for Alq_3, $Alq(Clq)_2$ and $Al(Clq)_3$ indicates that the extent of the red shift increases nearly linearly as the number of Clq ligands increases. Another tridentate unsymmetrical (salicylidene-*o*-aminophenolato)(8-quinolinolato)aluminum (Al(Saph-q)) [89] could be prepared by simply reacting $AlCl_3 \cdot 6H_2O$ and 8-hydroxyquinoline (1 eq.) in ethanol in the presence of piperidine followed by another equivalent of salicylidene-*o*-aminophenol. The glassy solid (Al(Saph-q)) was reported to have a higher T_g (226 °C) and to be thermally more stable than Alq_3. It was however difficult to understand why the intermediate of dichloro(8-quinolinolato)aluminum could simply be formed by mixing of $AlCl_3 \cdot 6H_2O$ and 8-hydroxyquinoline (1 eq.) without the contamination of Alq_3 as usually unsymmetrical Alq_2q^* could only be prepared using a hindered q-ligand as in 2-methylquinoline [90].

Other metal chelates which showed decent device performances and interesting fluorescent properties are shown in Fig. 10. Sano et al. at Sanyo [91] have prepared several kinds of 2:1 complexes with 8-hydroxyquinoline derivatives and a variety of metal ions, such as Be, Mg, Ca, Sr, Sc, Y, Cu or Zn. Amongst them, the beryllium complex (Beq_2) was found to be the most fluorescent (520 nm) in the green and the zinc complex (Znq_2) was found to have a strong yellow fluorescence (556 nm). They have also synthesized bis(10-hydroxybenzo[*h*]qinolinato)beryllium ($Bebq_2$) which has a very strong green fluorescence at λ_{max} 515 nm, a high melting point (368 °C), electron-transport property and achieved a luminance efficiency of 6.1 cd/A in a device of [ITO/TPD (50 nm)/$Bebq_2$ (50 nm)/Mg:In

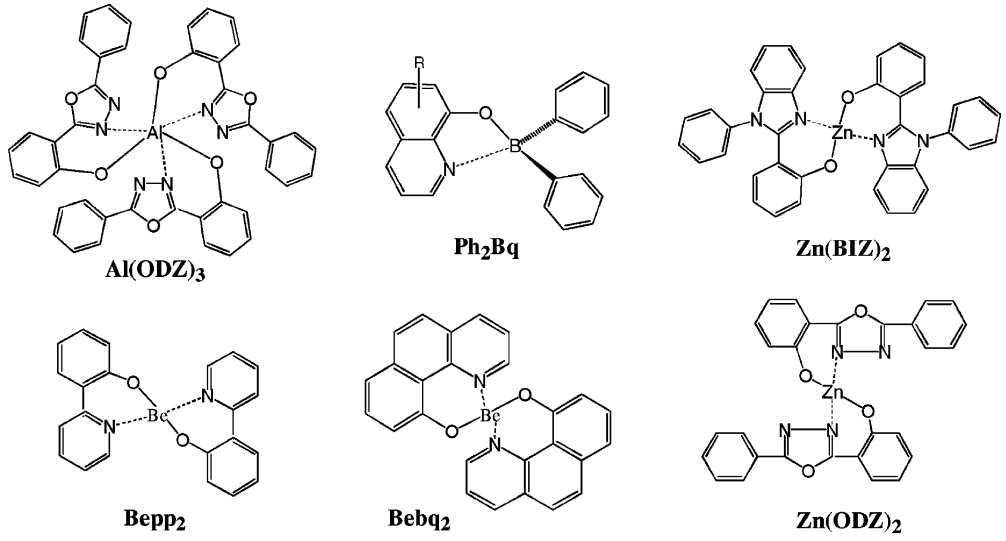

Fig. 10. Fluorescent metal chelates.

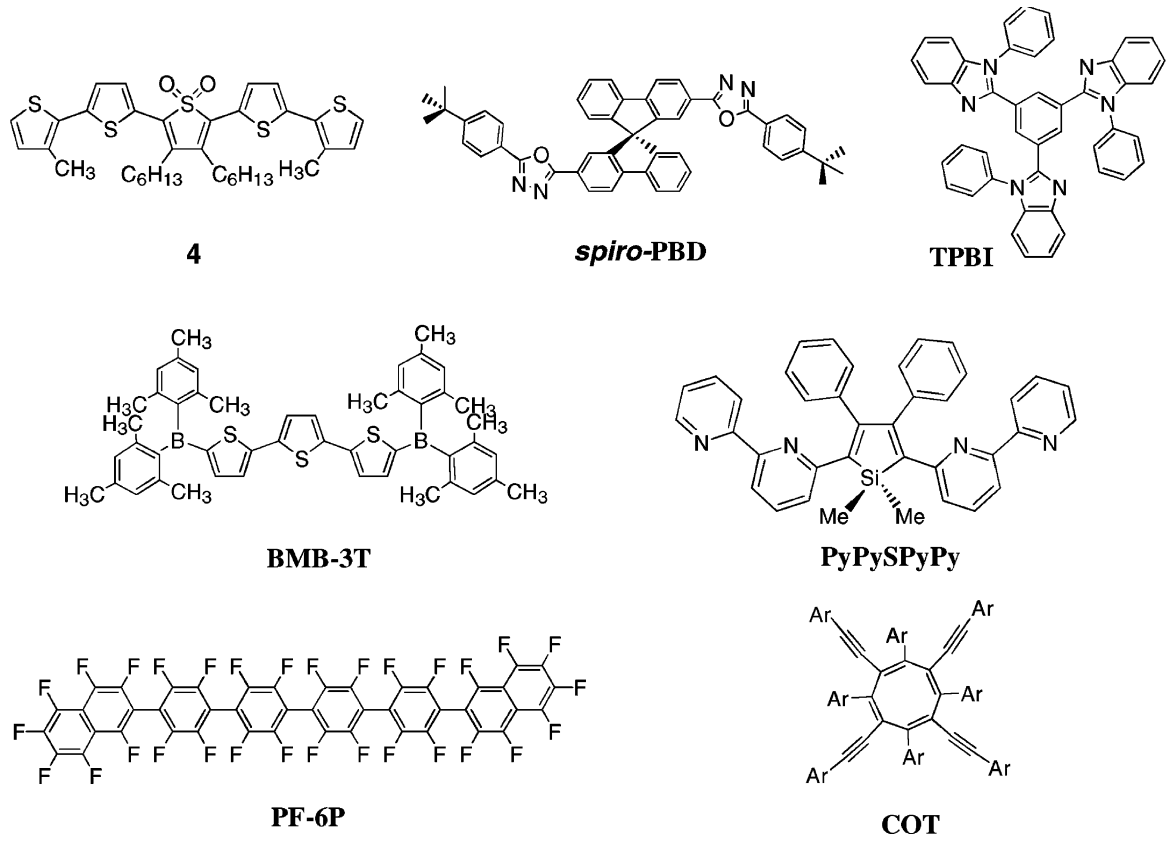

Fig. 11. Novel electron-transport materials.

(200 nm)]. The highly fluorescent bis[2-(2-hydroxyphenyl)pyridine]beryllium ($Bepp_2$) [92] as electron-transport emitter in [ITO/NPB (60 nm)/$Bepp_2$ (50 nm)/LiF (1 nm)/Al (200 nm)] was found to emit in the blue (445 nm) with a turn-on voltage of 3 V and a maximum luminance efficiency reaching 3.8 cd/A at 33 cd/m^2 and a maximum luminance of 15,000 cd/m^2 at drive voltage of 12 V. In their device, however, it was difficult to discern the origin of the blue emission which could come from both NPB and $Bepp_2$ layers. The diphenylboron analogs of Alq_3 (Ph_2Bq_2) have also been synthesized and their solution PLs were about 15 nm shorter and their quantum efficiencies were higher than those of the corresponding Alq_3 derivatives [93]. By combinatorial approach, (8-hydroxyquinolinolato)-lithium (Liq) and (2-methyl-8-hydroxyquinolinolato)lithium (LiMeq) have been found to be useful emitter and electron injection/transport materials [94].

Recently, the 2-(2-hydroxyphenyl)-5-phenyloxadiazole (ODZ) and 1-phenyl-2-(2-hydroxyphenyl)benzimidazole (BIZ) have been found to be useful bidentate ligands for aluminum and zinc chelations [95]. The most interesting chelates are $Zn(ODZ)_2$, $Zn(BIZ)_2$ and $Al(ODZ)_3$ as they all could serve as host electron-transport emitters in the blue.

In addition to metal chelates, there were a number of innovative approaches to the design of n-type organic semiconductors for use in OLEDs as electron-transport materials. Not all of them have been proven to work in devices. Fig. 11 represents a structural glossary of what have been published lately.

One of the most widely used electron-transport and hole blocking materials is 2-biphenyl-4-yl-5-(4-*t*-butylphenyl)-1,3,4-oxadiazole (PBD) which has been branched, *spiro*-linked [96] and

starbursted to prevent from crystallization in thin films. In oligothiophene, it was shown that by substituting with electron-withdrawing and bulky dimesitylboryl groups as in BMB-3T [97,98] could produce a superior electron-transport emitter. This concept was further demonstrated in thiophene/thienyl *S*,*S*-dioxide oligomer which has a high solid-state quantum efficiency (37%) and was used as electron-transport emitter in composite OLED [99] with substantial improvement of both the turn-on and operating voltages in comparison to conventional polythiophene-based OLEDs. Similar to electron-deficient oligothiophenes, perfluorinated oligo(*p*-phenylene)s have been shown to be efficient n-type semiconductors for OLED [100]. The perfluoro-2-naphthyl-substituted *PF-6P* which could be synthesized by organocopper cross-coupling reactions was reported to be a better electron-transport material than Alq_3 [101]. In a device of [ITO/TPTE (60 nm)/Alq_3 (40 nm)/PF-6P (20 nm)/LiF (0.5 nm)/Al (160 nm)] the luminance and current density were higher than those of Alq_3 above 4.5 V and reached 19,970 cd/m^2 at 10 V.

Tao et al. [102] revived 2,2′,2″-(benzene-1,3,5-triyl)-tris(1-phenyl-1*H*-benzimidazole) (TPBI) as an excellent electron-transport and hole blocker material in device [ITO/NPB/TPBI/Mg:Ag]. With an intermediate layer of CBP inserted between the NPB and TPBI layers, hole transport into the TPBI layer was assured [103]. The synthesis and characterization of *tetra*aryl-, *tetra*arylethynyl- and *octa*aryl-cyclooctatetraenes (COTs) as well as their use as electron-transport materials in OLEDs were reported by Thompson and coworkers [104]. These COTs are capable of forming highly stable glasses ($T_g > 177$ °C) and have a sufficiently wide energy bandgap (>3 eV) for fabricating blue-emitting OLEDs. Another class of electron-transport materials for OLEDs is 2,5-diarylsiloles [105]. It was reported that the bipyridylsilole derivative, PyPySPyPy, showed higher electron-transporting abilities than that of Alq_3 [106]. The efficiency of a device consisting of [ITO/TPD/Alq_3/PyPySPyPy/Mg:Ag] reached 2.2 lm/W at 3.4 V with a half-life 3× longer than that of the controlled device without PyPySPyPy under constant current drive.

3.4. Fluorescent dopants

One of the key developments in the advancement of OLED display technology can be attributed to the discovery of the guest–host doped emitter system [107]. This is because a single host material with optimized transport and luminescent properties may be used together with a variety of highly fluorescent guest dopants leading to EL of desirable hues with very high efficiencies. Another advantage of the doped emitter system in OLED is the enhancement of its operational stability by transferring the electrogenerated exciton to the highly emissive and stable dopant site thus minimizing its possibility for non-radiative decay [108]. This doping principle has recently been successfully extended to the exploitation of highly phosphorescent materials leading to nearly 100% internal EL efficiency [109]. We will discuss highlight of fluorescent RGB dopant developments in the following sub-sections and devote the last section to the review of the phosphorescent triplet emitter.

3.4.1. Green

The green fluorescent dopant was amongst the first to be successfully demonstrated in a commercial product and it is also by far the most efficient. One of the best green dopants is 10-(2-benzothiazolyl)-1,1,7,7-tetramethyl-2,3,6,7-tetrahydro-1*H*,5*H*,11*H*-[*l*]benzo-pyrano[6,7,8-*ij*]quinolizin-11-one, known as C-545T [110–112] which belongs to the highly fluorescent class of coumarin laser dyes. By virtue of its structural coplanarity, the *julolidine* donor situated at carbon #7 aligns its p-orbital of nitrogen to overlap with the π-orbitals of the phenyl ring for more effective conjugation which results in increasing its relative PL quantum yield (η) to 90%. It is believed that the

enhancement of η is obtained by diminishing non-radiative deactivation of the excited state by reducing the internal mobility and, since the single C–N bond often is the weakest linkage in such a molecule, the enhanced conjugation of the julolidine system is expected to also improve dye stability [113]. The four strategically positioned methyl groups in C-545T are important as *steric spacers* to minimize the dye–dye interaction at high concentration that leads to quenching of the fluorescence. Later, the Kodak group discovered that by substituting *t*-butyl groups at the benzothiazolyl ring as in C-545TB [114], the concentration quenching problem could be further suppressed and the thermal property was also greatly improved (T_g enhanced to 142 °C from 100 °C) without compromising its emissive color. In addition, in the device of [ITO/CuPc (15 nm)/NPB (75 nm)/Alq_3 + 1% dopant (35 nm)/Alq_3 (35 nm)/Mg:Ag (200 nm)], the luminance efficiency could be significantly increased from 10.5 cd/A (C-545T) to 12.9 (C-545TB) at a drive current density of 20 mA/cm^2 and with a 1931 CIE color coordinates of $x = 0.30$; $y = 0.65$.

One of the more interesting results in subsequent research was found in C-545MT [115,116] where an extra methyl group was substituted at the C-4 position of C-545T. When doped in Alq_3 as green emitter in OLED, C-545MT has the unusual property of resistance to concentration quenching and the sustaining of its EL luminance efficiency (~7.8 cd/A) over a wide range of doping concentration from 2 to 12%, which is more than 10 times that of C-545T (Fig. 12). Single crystal XRD evidence (Fig. 13) suggested that the difference in doping behaviors could be linked to the

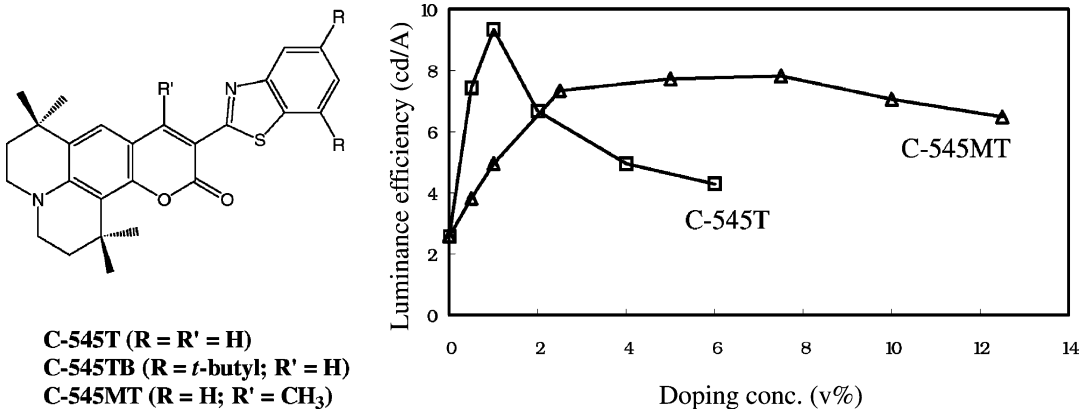

Fig. 12. Comparison of luminance efficiency vs. doping concentration of C-545T and C-545MT.

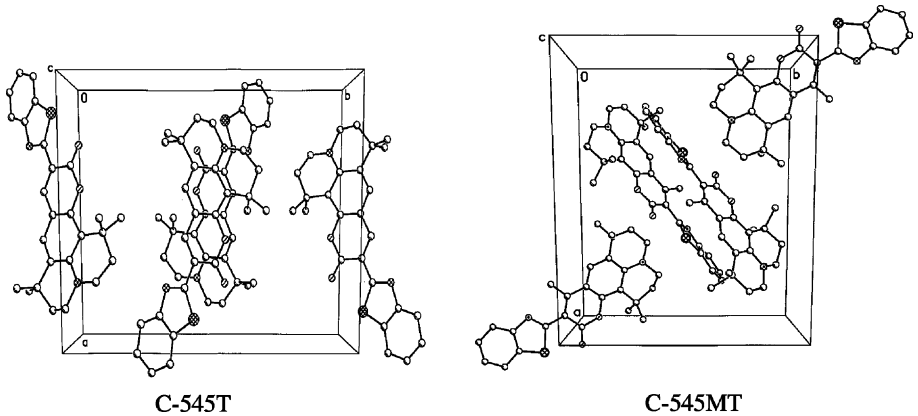

Fig. 13. Comparison of molecular packing in unit cells.

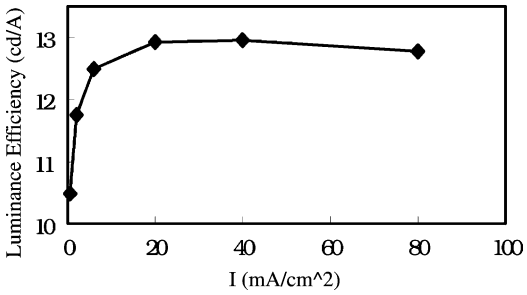

Fig. 14. Luminance Efficiency of C-545TB vs. current density.

difference in molecular packing as well as volume of unit cell of the perspective dopant crystals. The twisted molecular geometry of C-545MT which is distorted by the steric effect of C(4)-methyl substituent could prevent the undesirable molecular aggregation from occurring at high concentration thus delaying the onset of quenching. Additional advantage of this particular series of coumarin dopants can be found from C-545TB in Fig. 14 with its nearly flat response of luminance efficiency (cd/A) with respect to a wide range of drive current conditions at an optimal doping concentration of about 1%. This is particularly desirable for the passive-matrix displays where the system would need to be capable of very high luminance at low voltage and have a ''flat'' cd/A response with respect to drive voltage.

In studying the effect of the location and width of doping region on efficiency using 3-(2-benzothiazolyl)-7-(diethylamino)-2*H*-1-benzopyran-2-one (C-6), it was found that [117] the recombination zone was 10 nm thick near the doped emitter/hole-transport layer interface and dopant molecules behaved as carrier traps and hopping sites in the Alq_3 hosted emitter layer. Other notable green dopants exemplified in Fig. 15 are *N*,*N*′-diethylquinacridone (DEQ) [118] which was shown to be thermally durable in the doped device with temperature-independent quantum efficiency; imidazolidinone **4** derived from the green fluorescent protein of *Aequorea* [119]; 1-aryl-2-(5-dithoacetal-*S*,*S*-dioxide ketenyl-2-thienyl)-5-(2-thienyl)pyrrole (**5**) [120] and organolanthanide phosphor, (*t*-bu-PMP)$_3$Tb(Ph_3P=O) [121].

3.4.2. Red

Among the RGB dopants used in OLED, red emission, due to its low efficiency, remains to be the weakest link in realizing the full potential of an active-matrix [122] and passive dot matrix [123] full-colored OLED display. Research in search of a good red has established a target specification of luminance efficiency of over 4 cd/A, a saturated color with CIE coordinates approaching ($x = 0.65$; $y = 0.35$) and a device lifetime of over 10,000 h at an initial luminance of 300 cd/m^2 under constant current drive. To date, few dopants in the red can meet all of these goals. One of the best that comes close is 4-(dicyanomethylene)-2-*t*-butyl-6-(1,1,7,7-tetramethyljulolidyl-9-enyl)-4*H*-pyran better

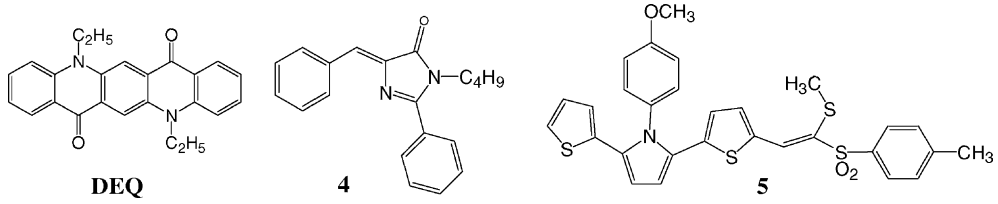

Fig. 15. Non-coumarin green fluorescent dopants.

known as DCJTB [124]. In 1999, the luminance efficiency of DCJTB as reported by Sanyo/Kodak was 1 cd/A for the 2.4 in. LTPS AMOLED. The luminance of red was a factor of 10 lower than the green. When a white emission was demanded, the red component occupied more than half of the power consumption. Later, it was found by adding rubrene as an emitting assist dopant, the energy transfer from Alq_3 to DCJTB could be achieved more efficiently leading to a desired saturation with 2.2 cd/A efficiency [125]. Further, by adding a carrier trap dopant in Alq_3 layer or as a separate layer in the device to adjust the charge balance, Hamada [126] of Sanyo reportedly has achieved an EL efficiency of 2.8 cd/A for DCJTB doped emitter. The exact device structure disclosed was [ITO/NPB (150 nm)/2% DCJTB + 6% NPB + 5% rubrene in Alq_3 (37.5 nm)/Alq_3 (37.5 nm)/LiF/Al (200 nm)] which produced a saturated red emission at λ_{max} 632 nm with a $CIE_{x,y} = [0.65, 0.35]$ at a drive voltage of 8.5 V with a luminous power efficiency of 1.03 lm/W [127]. Because of the extra NPB dopant in the emitter layer to trap the excess $[Alq_3]^+$, the device was demonstrated to be very stable attaining an operating half-life of ~8000 h. The EL efficiency of DCJTB doped Alq_3 emitter has been found to also decrease markedly with increasing current density—a phenomenon that is not observed in the corresponding green coumarin dopants. This phenomenon is attributed to the quenching of excited singlet $[DCJTB]^*$ by cationic species, either $[DCJTB]^+$ or possibly $[Alq_3]^+$, but not the corresponding anionic species [128]. Recently, a double heterostructure with narrow recombination zone [129] has been proposed to increase the red EL efficiency, but did little to improve that of DCJTB. It appears that there is still ample room for improvement of the EL efficiency of DCJTB once the quenching mechanism of this remarkable dopant is understood.

An alternative dopant in the same class is the *i-propyl* derivative DCJTI [130] which is easier to synthesize and more amenable to large scale production without compromising its EL efficiency and chromaticity. Recently, it was reported [131] that an 8-methoxy-substituted derivative (DCJMTB) doped in tris(8-hydroxyquinolinolato)gallium (Gaq_3) host matrix at 1% in a device structure of [ITO/TPD(80 nm)/DCJMTB%:Gaq_3 (60 nm)/Gaq_3 (20 nm)/Mg:Ag (200 nm)] achieved a luminance efficiency of 2.64 cd/A at 20 mA/cm^2 with a power efficiency of 0.72 lm/W and CIE color coordinates of ($x = 0.63$; $y = 0.36$). The same dopant in Alq_3 could only get 1.91 cd/A with the same chromaticity. The improved performance in Gaq_3 host was rationalized as due to the better energy level matching between the host and the dopant which enhanced carrier injection and confinement from Gaq_3 to DCMTB. Similar dopants based on the chromene [132] were much less efficient, however. Replacing the *julolidyl* donor in DCJTB with a lesser donating *diphenylamino* group as in 4-(dicyanomethylene)-2-*t*-butyl-6-(*p*-diphenylaminostyryl)-4*H*-pyran (DCTP) [133] which shifts the PL emission to yellow at λ_{max} 564 nm with a quantum yield of 94%. Its EL efficiency at 2% doping in Alq_3 reached 5.3 cd/A and 1.6 lm/W at 11 V and 20 mA/cm^2 with a $CIE_{x,y}$ of 0.47; 0.51.

As shown in Fig. 16, other notable red dopants published in the last three years were: 3-(dicyanomethylene)-5,5-dimethyl-1-[(4-dimethylamino)styryl]cyclohexene (DCDDC) [134], 6-methyl-3-[3-(1,1,6,6-tetramethyl-10-oxo-2,3,5,6-tetrahydro-1*H*,4*H*,10*H*-11-oxa-3*a*-azabenzo[*de*]-anthracen-9-yl)acryloyl]pyran-2,4-dione (AAAP) [135], 6,13-diphenylpentacene (DPP) [136] and 3-(*N*-phenyl-*N*-*p*-tolylamino)-9-(*N*-*p*-styrylphenyl-*N*-*p*-tolylamino)perylene [(PPA)(PSA)Pe-1] [137]. DCDDC was claimed to exhibit an EL spectra with a full width at half maximum (FWHM) of 70 nm when doped in [ITO/PVK:TPD/DCDDC:Alq_3/Mg:Ag]. Judging by the EL spectra recorded at various doping concentration, the energy transfer was rather poor. Dopant AAAP appeared to be a novel structure, but presumably due the presence of too many ketonic carbonyl groups, its luminance efficiency was too low to be attractive. The more interesting DPP was reported to exhibit a narrow emission spectrum when doped at 0.55 mol% into Alq_3 giving rise to a saturated red peak, centered around 625 nm, with a CIE chromaticity coordinates of [$x = 0.63$; $y = 0.34$]. The advantage of DPP

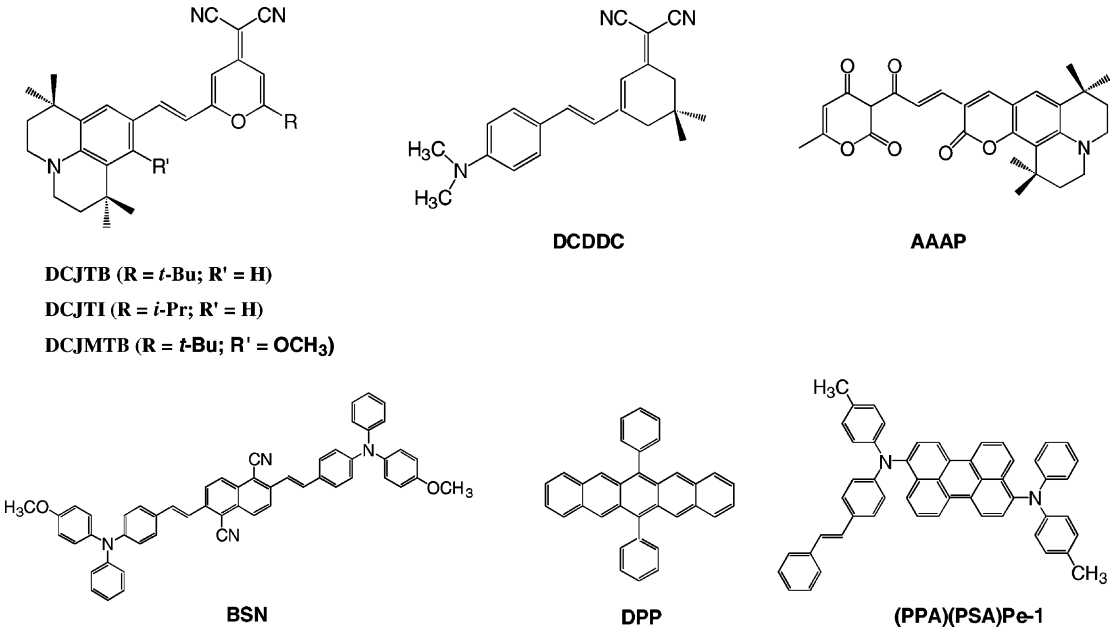

Fig. 16. Typical red fluorescent dopants.

appears to rest in its relatively stable external EL quantum efficiency at around 1% over a wide range of drive current density of 1–100 mA/cm^2 that is ideal for passive as well as active display applications. The disadvantage of this dopant seems to come from the intrinsic properties of its EL and solid PL emissions which contain several vibronic structures at 680 and 740 nm (shoulder) that are too close to the edge of the infrared spectrum. As a result, DPP's luminance is compromised in the region where eyes are least sensitive. A new perylene derivative, 3-(*N*-phenyl-*N*-*p*-tolylamino)-9-(*N*-*p*-styrylphenyl-*N*-*p*-tolylamino)perylene ((PPA)(PSA)Pe-1) designed with separated functionalities of luminescent center and carriers transport units was found to produce a red emission with 1.0 cd/A at 100 cd/m^2 in a triple-layered device of [ITO/starburst amine (25 nm)/(PPA)(PSA)Pe-1 (60 nm)/Alq_3/Mg:Ag (140 nm)]. The styryl substituent gives rise to a shoulder at 620 nm in addition to its λ_{max} emission peaking at 580 nm which shifts the $CIE_{x,y}$ coordinate from the usual orange emission to a more saturated red at ($x = 0.64$; $y = 0.35$). Like DPP, the EL efficiency of many of these perylene derivatives with *styryl* substituents are almost independent of the drive current density. It is reasoned that when the voltage applied to a device increases, the higher carrier mobility of the styrylphenyl-amino-substituted perylene makes the increase in electric field strength in the light-emitting layer smaller. As a result, there will be little change in the distribution of the charge recombination zone in a light-emitting layer with steady electric field strength.

One of the more exciting developments in red emitter was recently disclosed by Sony [138]. The 1,1′-dicyano-substituted bis-styrylnaphthalene derivative (BSN) has a film absorption at λ_{max} 507 nm and a strong PL at λ_{max} 630 nm with a quantum efficiency of 0.80. It has good thermal properties with $T_g = 115$ °C, $T_c = 161$ °C and $T_m = 271$ °C and was reported to form a good amorphous thin film on evaporation. Solid-state photo-ionization measurements place its LUMO at 2.93 eV and HOMO at 5.38 eV which favors the efficient recombination of electrons and holes to take place within the emitter layer. In a device of [ITO/2-TNATA/NPB/BSN/Alq_3/Li_2O/Al], BSN as a red emitter without dopants displays an impressive luminous efficiency of 2.8 cd/A at 500 cd/m^2 with CIE $x, y = 0.63, 0.37$. This red emission apparently can be further improved to the saturated

color of CIE $x, y = 0.66, 0.34$ by Sony's proprietary top emission adaptive current drive structure (TAC) demonstrated in their 13 in. LTPSi active-matrix TOLED prototype display. It was disclosed further that the color of this device was apparently not affected by the drive current. Thus, BSN rivals the best of doped red fluorescent emitters of today. A similar red electroluminescent dye D-CN based on the bis(styryl) nucleus and synthesized by the bis-Knoevenagel condensation of 1,4-phenylenediacetonitrile and 2 eq. of 4-formyl-4′-methoxytriphenylamine has also been reported recently [139]. A trinuclear zinc(II) complex with six 2-[2-(4-cyanophenyl)ethenyl]-8-quinolinolato bidentate ligands (Zn_3(2-CEQ)$_6$) [140] was found to have a strong solid PL at λ_{max} 600 nm and a quantum efficiency of 0.32 with an excited state lifetime of 2.40 ns. This bulky metal complex, if thermally sublimable, could be an interesting host material for use as a red doped emitter.

There were many studies on getting sharp and saturated emission from europium complexes by varying the ligand designs. These dopants however usually have low efficiencies and brightness. Representative examples are: europium tris(dibenzoylmethide)(triphenylphosphine oxide) (Eu(DBM)$_3$(TPPO)) [141,142], europium tris(thienoyl-trifluoroacetone)(phenanthroline) (Eu(TTFA)$_3$(phen)) 121 and europium tris(dibenzoylmethide)(1-ethyl-2-(2-pyridyl)benzimidazole) (Eu(DBM)$_3$(EPBM)) [144]. The fabrication of an OLED device using an ytterbium (III) complex, tris(dibenzoylmethanato)(monobathophenanthroline)Yb(III) [145] as a near-IR emitting material around 900–1100 nm region for application in optical fiber communications has also been reported.

3.4.3. Blue

The blue doped emitter in OLED often necessitates the judicious selection or design of an appropriate blue host material which has a wide enough bandgap energy and a set of matching LUMO/HOMO level to effect the sensitization. Several examples are shown in Fig. 17. For full-color OLED displays [106], the target to shoot for is around 4–5 cd/A depending upon the color purity which can be from the CIE coordinates of ($x = 0.14$–0.16) and ($y = 0.11$–0.15). It appears that there are a number of blue dopant/host systems that can achieve this efficiency with CIE $x = 0.15$; $y = 0.15$. But, the status of their device operational lifetimes leaves much to be improved [146]. In commercial circles, one of the best blue emitters used in OLED is believed to have been patented by Idemitsu Kosan Co. based on the basic structure of *distyrylarylene* (DSA) host doped with a hole transporting amine-substituted DSA dopant [147,148]. This doped blue emitter reportedly could achieve a luminous efficiency of >6 lm/W at 100 cd/m^2 with a lifetime of continuous DC operation of >30,000 h and the shelf storage stability is >500 h at 85 °C [149]. The corresponding CIE coordinates were unfortunately not disclosed and the exact nature of the structures remained a heavily guarded trade secret. However, most people in the OLED materials research community should have realized by now that the best dopant/host molecules are probably not what were disclosed in the open literature (e.g. BCzVBi/DPVBi) [150]. TDK in efforts of developing the white OLED emission has also disclosed a blue host material based on phenylanthracene derivatives (PAD). The details of these structures are also sketchy [151]. Kodak also disclosed its doped blue emitter based on 9,10-di(2-naphthyl)anthracene (β-DNA) and *tetrakis*(*t*-butyl)perylene (TBPe) [152] which in the device structure of [ITO/CuPc (15 nm)/NPB (60 nm)/DNA + 2% TBPe (30 nm)/Alq$_3$ (35 nm)/Mg:Ag (200 nm)] reached a luminance efficiency of 3.2 cd/A at 20 mA/cm^2 with a cyanish blue emission of CIE coordinates of $x = 0.154$; $y = 0.232$. Since DNA could effectively transport holes due to its relatively high HOMO, it was not clear whether some of the emission might have come from some of the leakage of holes that recombined in the Alq$_3$ electron-transport layer. By replacing Alq$_3$ with a hole blocking, electron-transport material TPBI, the same device achieved an impressive EL efficiency of 5 cd/A at the same drive condition with an improved blue emission of

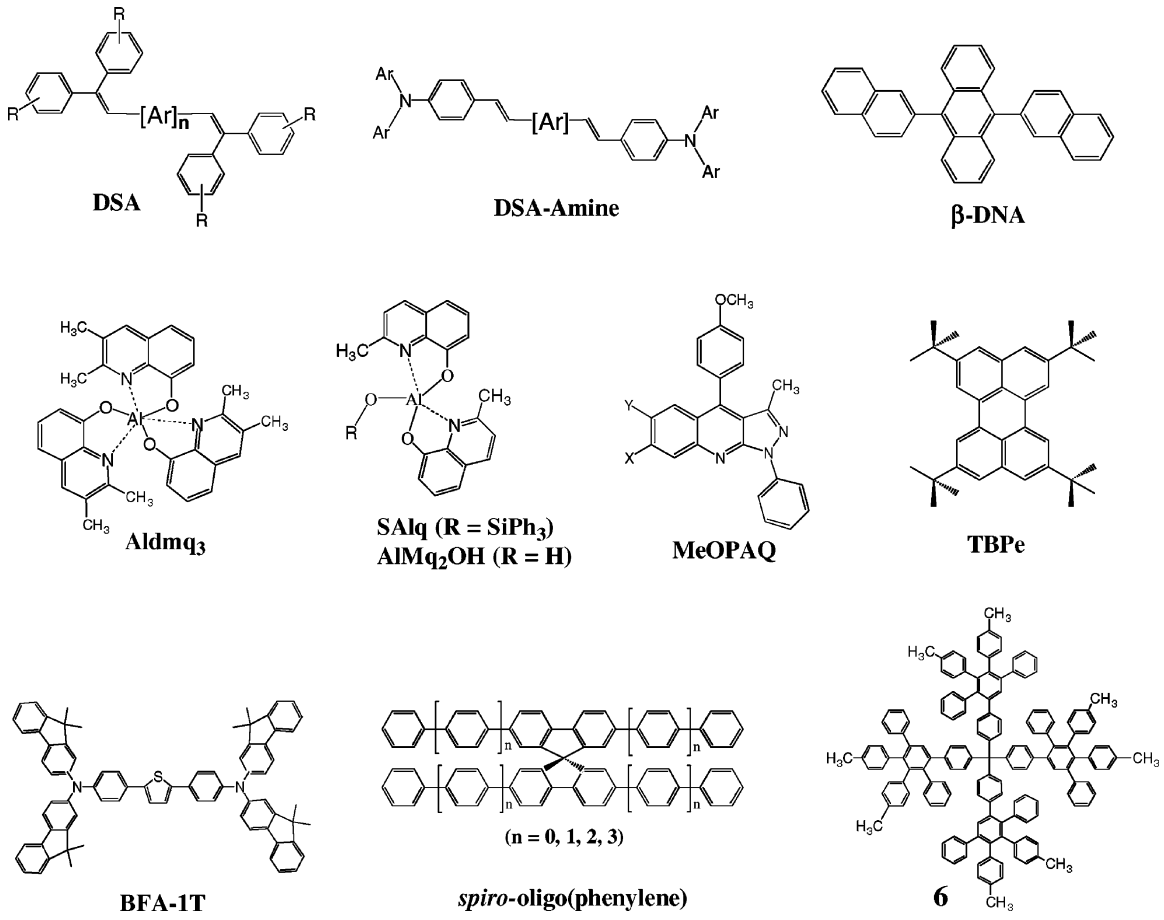

Fig. 17. Typical blue host and doping materials.

CIE $x = 0.137$; $y = 0.203$. The bulky TBPe was reinvestigated by doping in bis(2-methyl-8-quinolinolato)(*p*-phenylphenolato)aluminium (III) (B-Alq) and found to be more resistant to concentration quenching than the parent perylene. As a result, the constancy of EL color and efficiency are preserved by using the stericly hindered TBPe as a blue dopant [153]. The non-planar blue-emitting TPBI host also could prevent the exciplex formation of dopant BMB-2T with TPD in the device of [ITO/TPD/TPBI:BMB-2T/TPBI/Mg:Ag] [154] where a pure blue emission peaking at 446 nm with CIE coordinates of $x = 0.15$; $y = 0.12$ was obtained with an efficiency of <1 cd/A.

Many hole transporting materials such as NPB, PPD, TTNND described previously are capable of emitting in the blue. Here, in order to prevent holes from recombination elsewhere, insertion of a hole blocking layer (HBL) such as Salq [53] and TPBI [155] in OLED often becomes necessary to enhance the EL efficiency and maintaining the purity of the blue emission. There were a number of novel pyrazoline derivatives [156] that have been used as emitters in blue OLED, but their performance was not remarkable. Other notable examples of blue-emitting amorphous materials as shown in Figs. 17 and 18 are: 2,5-bis{4-[bis-(9,9-dimethyl-2-fluoreyl)amino]phenyl}thiophene (BFA-1T) [157], *spiro*-oligo(*p*-phenylene) [96], 9,10-bis[(2″,7″-di-*t*-butyl)-9′9″-*spiro*bifluorenyl]anthracene (TBSA) [158], terfluorene [159] and the triphenylsilyl-substituted derivative PhTPAOXD [160]. Many of these novel materials which have very high glass transition temperatures (with the *spiro*-terfluorene championing at $T_g = 296\ ^\circ C$) can act as efficient blue emitters without needing a

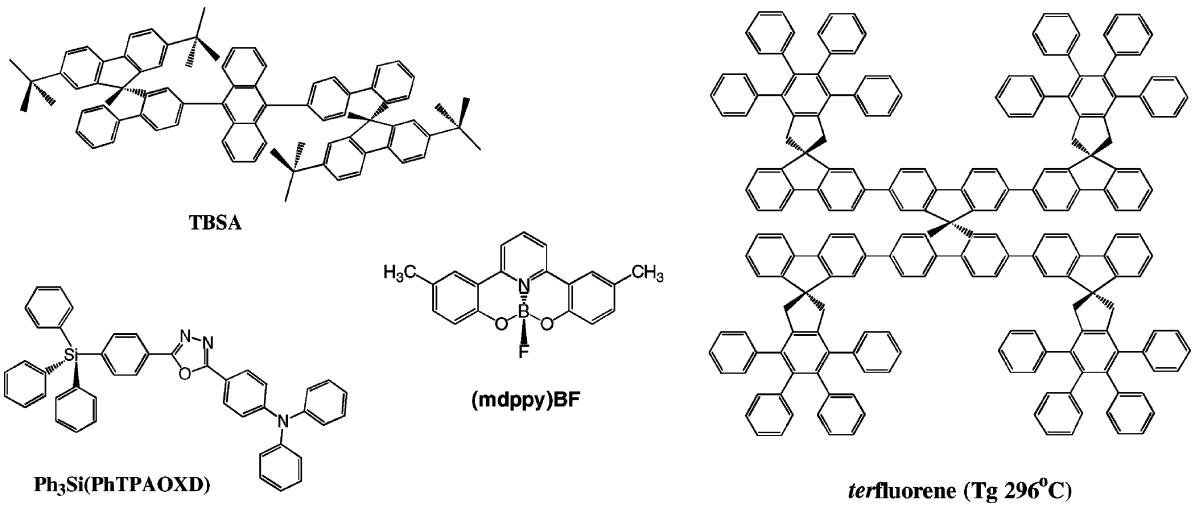

Fig. 18. Miscellaneous blue-emitting materials.

dopant. The bis(*spiro*bifluorenyl)anthracene (TBSA) is reported to achieve a luminous efficiency of 1.22 lm/W (3 cd/A) at a drive voltage of 7.7 V and a brightness of 300 cd/m^2 in the device of [ITO/CuPc (20 nm)/NPB (50 nm)/TBSA (20 nm)/Alq_3 (30 nm)/LiF (1 nm)/Al]. The CIE color of this emission is $x = 0.15$; $y = 0.11$ which is claimed to be the nearest to the NTSC standard ever reported for a blue OLED.

Finally, a blue fluorescent boron complex of the dianion of 1,6-bis(2-hydroxy-5-methylphenyl)pyridine, (mdppy)BF (solid PL $\lambda_{max} \sim 450$ nm) has recently been reported to produce highly efficient white organic EL from a double-layered device [161]. The ligand (H_2mdppy) was prepared by the reaction of 2,6-dibromopyridine and the Grignard reagent from 2-bromo-4-methylanisole in THF with [$NiCl_2$(dppe)] as catalyst (dppe = $Ph_2PCH_2CH_2PPh_2$) followed by demethylation in molten pyridinium chloride. Reaction of H_2mdppy with 1 eq. of BF_3 in benzene gave the boron complex, (mdppy)BF. The white EL, whose spectrum is very broad spanning the entire visible spectrum from 400 to 700 nm, is said to have been caused by exciplex emissions formed at the interface between NPB and (mdppy)BF. It is interesting to note that this simple device [ITO/NPB (60 nm)/(mdppy)BF (60 nm)/LiF (1 nm)/Al (200 nm)] with only one emitting material could achieve an efficiency of 1.5 lm/W (3.3 cd/A) and a luminance of 620 cd/m^2 at a current density of 20 mA/cm^2 and a driving voltage of 7 V with a white color of $CIE_{x,y} = [0.30, 0.36]$.

Enhanced blue electroluminescence from vapor deposited *p*-sexiphenyl (**6p**) layer has been observed in [ITO/TPD (60 nm)/**6p** (50 nm)/Mg:Ag] device structure [162]. *p*-Sexiphenyl was reported to be 5 times more electron-transporting but 10 times worse fluorescent than Alq_3. 4-(*p*-Methoxyphenyl)-3-methyl-1-phenylpyrazol-5-one (MeOPAQ) [163] doped in TPBI in the presence of a hole blocker, *N*,*N*-bis(carbazolyl)-4,4′-biphenyl (CBP), in the device of [ITO/NPB/CBP/TPBI:MeOPAQ/TPBI/Mg:Ag] reached a luminance efficiency of 3.8 cd/A at 25 mA/cm^2 and CIE of $x = 0.19$; $y = 0.16$.

An efficient blue emitter based on bis(2-methyl-8-quinolinolato)aluminum(III) hydroxide ($AlMq_2OH$) [164] was observed without dopant in a device consisting of [ITO (72 Ω/□)/CuPc (10 nm)/NPB (50 nm)/$AlMq_2OH$ (80 nm)/LiF (0.7 nm)/Al (80 nm)] which achieved a luminance efficiency of 5.03 cd/A at 80 mA/cm^2. The EL emission centered at 485 nm with FWHM of 80 nm might appear greenish. $AlMq_2OH$ which was made by mixing a 1:2.2 equivalent ratio of aluminum acetate in DI water to 8-hydroxyquinaldine in absolute alcohol (80% yield) was surprisingly quite

stable with an onset degradation temperature of 424 °C and could be train-sublimed at 10^{-6} Torr. Another tridentate aluminum chelates, tris(2,3-methyl-8-hydroxyquinolinolato)-aluminum(III) ($Aldmq_2$) [165] was reported to emit blue light in a device consisting of [ITO/TPD/$Aldmq_2$/Mg:Ag] with a EL emission λ_{max} 470 nm and a FWHM of 90 nm. The luminance efficiency was however, low and judging by the EL curve shape, the emission looked greenish. Finally, an elegantly designed and meticulously synthesized shape-persistent polyphenylene dendrimer **6** from Mullen's laboratory [166] deserves citation for possible application in the OLED as blue host material.

3.5. Triplet emitting materials

One of the key developments in the advance of modern OLED sciences and technology is the discovery of *electrophosphorescence* which lifts the upper limit of the internal quantum efficiency of the usual fluorescent dopant-based devices from 25% to nearly 100%. Phosphorescence is inherently a slower and less efficient process, but triplet states constitute the majority of electrogenerated excited states (∼75%), so the successful utilization of the triplet manifold to produce light should undoubtedly increase the overall luminance. The design and synthesis of triplet emitting materials containing heavy-metal complexes, where strong spin-orbit coupling leads to singlet–triplet state mixing which removes the spin-forbidden nature of the radiative relaxation of the triplet state, are therefore particularly important in achieving high-efficiency electrophosphorescence in OLEDs. Several examples are shown in Fig. 19. One of the first examples of triplet emitting device is based on the red 2,3,7,8,12,13,17,18-octaethyl-12*H*,23*H*-porhine platinum(II) (PtOEP) [167] which achieved an external quantum yield of 5.6% doped in CBP [168]. But, the relatively long

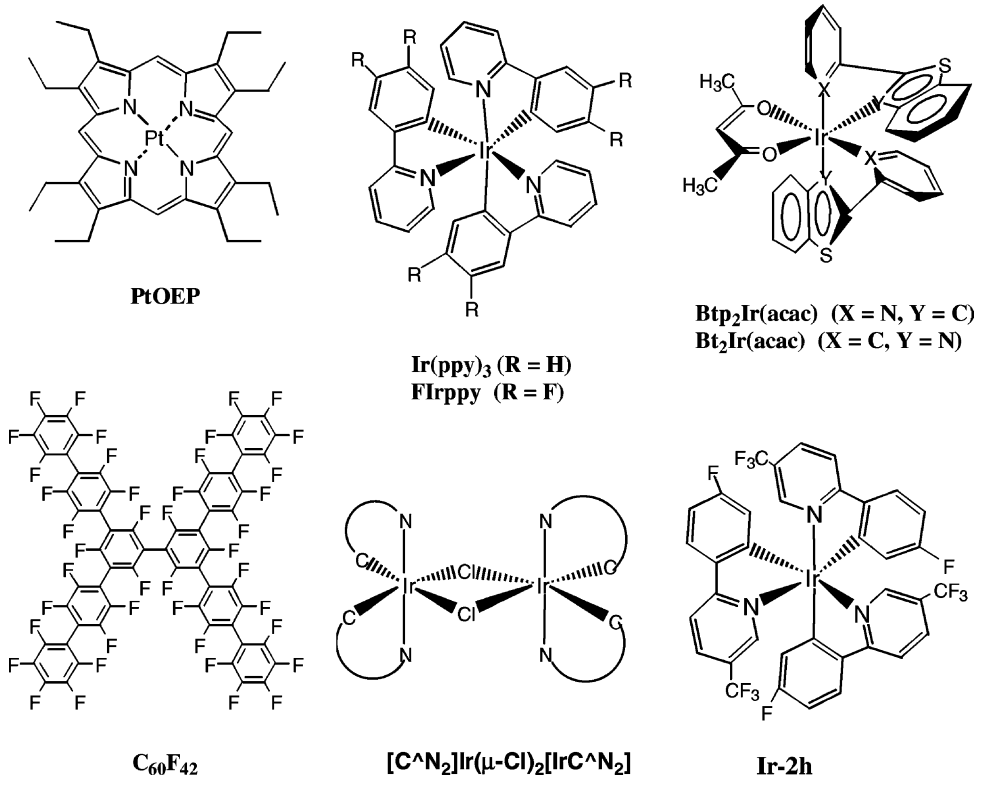

Fig. 19. Triplet emitting materials and related intermediates.

phosphorescence lifetime (~50 μs) of PtOEP tends to result in triplet–triplet annihilation at high current [109]. Lanthanide europium (Eu) complexes also show triplet emission and have been used in red electroluminescent devices [169]. Later it was found that the red triplet phosphor, bis(2-(2′-benzo[4,5-*a*]thienyl)pyridinato-N,$C^{3'}$) iridium(acetylactonate) ($Btp_2Ir(acac)$) [170] with a shorter phosphorescence lifetime (~4 μs) leads to a significant improvement in η_{ext} reaching 2.5% at high current density of 100 mA/cm^2 as compared to PtOEP. The red EL spectrum of $Btp_2Ir(acac)$ has a maximum at $\lambda_{max} = 616$ nm with additional intensity peaks at 670 and 745 nm and the CIE coordinates are $x = 0.68$; $y = 0.32$.

An even shorter lifetime (~1.8 μs) has recently been reported for Os complexes which were used as red electrophosphorescent dopants blended in poly(*N*-vinylcarbazole) and 2-*t*-butylphenyl-5-biphenyl-1,3,4-oxadiazole as the emitting layer in a polymer LED [171]. The emission peaks of the reported Os complexes, ranging from 620 to 650 nm, can be tuned by changing the structures of the ligands because the emission originates from triplet metal-to-ligand charge-transfer excited state. The osmium complexes trap both electrons and holes, which facilitates the direct recombination of holes and electrons on the dopant sites. The peak external quantum efficiency and brightness achieved from the complexes were 0.82% and 970 cd/m^2 with $CIE_{x,y} = 0.65, 0.33$.

One of the best electrophosphorescent green materials is *fac*-tris(2-phenylpyridine)iridium ($Ir(ppy)_3$) [172] which when doped into CBP host exhibits peak external quantum and power efficiencies of 28 cd/A and 31 lm/W, respectively. At 100 cd/m^2, the external quantum and power efficiencies of 26 cd/A and 19 lm/W were reached at a drive voltage of 4.3 V. By further optimization of materials and device architecture, the efficiencies of the green triplet emitter based on $Ir(ppy)_3$ can be improved to nearly double (38 lm/W) [173] at the voltage of 4 V and a luminance of 105 cd/m^2. A tris-*ortho*-cyclometalated iridium complex based on pinene-substituted 2-phenylpyridine ($Ir(mppy)_3$) has recently been found to reduce concentration quenching because the sterically hindered pinene spacer in the phosphor molecule minimizes molecular aggregation or interaction [174].

One of the keys to highly efficient phosphorescent emission in OLEDs is to confine the triplet excitons generated within the emitting layer. Thus, by employing starburst perfluorinated phenylene ($C_{60}F_{42}$) as both hole and exciton blocking layer, and a starburst hole-transport material of 4,4′,4″-tris(*N*-carbazolyl)triphenylamine as a host matrix for the $Ir(ppy)_3$ dopant in the emitter, a maximum external quantum efficiency reaches to 19.2%, and the efficiency is sustained over 15% even at high current densities of 10–20 mA/cm^2 which is better than the brightness of fluorescent tubes for lighting. The onset voltage of the electroluminescence is as low as 2.4 V and the peak power efficiency reaches 72 lm/W which fulfills the promise of OLED as a potential low-power display device [175]. This performance can be attributed to the efficient transfer of both singlet and triplet excited states of the host to $Ir(ppy)_3$, leading to high internal efficiency. Another advantage of $Ir(ppy)_3$ is that it has a short phosphorescent decay time of <1 μs which reduces saturation of the phosphor at high drive current conditions. In addition to emission from the iridium dopant, it is possible to transfer the exciton energy also to a fluorescent dye by Förster energy transfer. The Ir dopant in this case acts as a sensitizer, utilizing both singlet and triplet excitons to efficiently pump a fluorescent dye [109] and thus avoiding the quenching of phosphorescence by triplet–triplet annihilation. Based on $Ir(ppy)_3$-sensitized DCJ fluorescence in CBP host matrix, high-efficiency yellow double-doped OLEDs [176] with external quantum efficiency of 4.1% and EL efficiency of 11 cd/A (3.1 lm/W) have been achieved at a drive current of 10 mA/cm^2.

The latest news on the operational lifetime of the green $Ir(ppy)_3$ and the red $Btp_2Ir(acac)$ doped emitters under constant DC drive as defined by $T_{1/2}$ (50% of initial brightness) are ~10,000 h ($L_0 = 500$ cd/m^2) and ~2000 h ($L_0 = 100$ cd/m^2), respectively. It was further disclosed that further

improvement of operational lifetime of the red $Btp_2Ir(acac)$ to ~10,000 h is possible by optimizing the architecture of a mixed-layer comprising a hole transporter, an electron transporter and a phosphorescent dopant as the emissive layer [177].

All of the iridium chelates can be synthesized by *cyclometalation* using $IrCl_3 \cdot nH_2O$ onto an appropriate ligand such as 2-phenylbenzoxazole, 2-phenylbenzothiazole, 2-phenylpyridine and 2-phenylquinoline [178]. These reactions produce chloride-bridged dimers, $[C^{\wedge}N_2]Ir(\mu\text{-}Cl)_2[Ir\ C^{\wedge}N_2]$ which can be transformed into a variety of different octahedral iridium(III) complexes $[C^{\wedge}N_2]Ir(LX)$. Judicious choice of the cyclometalating ligand $[C^{\wedge}N]$ can lead to a variety of colors of emission that range from green to red. Recently, DuPont researchers have developed a new synthesis of organometallic iridium complexes that can be prepared in one step by heating $IrCl_3 \cdot nH_2O$ in excess $[C^{\wedge}N]$ ligand in the presence of a catalytic amount of silver trifluoroacetate as promoter [179]. By this method, they have synthesized a variety of fluorinated and trifluoromethylated derivatives with emissions ranging from λ_{max} 506 to 595 nm. It was claimed that by replacing C–H bonds to C–F bonds by fluorination, there are several potential benefits: (1) the C–H bond is an effective promoter for radiationless decay of an excited state. Replacing it with a C–F bond of lower vibrational frequency can reduce the rate of radiationless deactivation and enhance the PL efficiency; (2) fluorinated compound usually can be sublimed better for thin film deposition; (3) introduction of C–F bond or CF_3 group can alter the molecular packing and minimize the self-quenching behavior; (4) fluorination can enhance the electron mobility; (5) HOMO/LUMO levels can be modified by fluorination and thus allow the optimization of carrier injection and the tuning of EL color. As a matter of fact, one of the bluest emissive triplet complexes reported is *fac*-tris[2-(4,5′-difluorophenyl)pyridine-C'^2,N] iridium(III) known as Firppy [180] which has $\lambda_{max} = 500$ nm in polystyrene with a quantum yield of ~22% and a triplet lifetime of ~4.5 μs. It was also shown for the first time that the *fac*-tris[5-fluoro-2-(5-trifluoromethyl-2-pyridinyl)phenyl-C,N]iridium (Ir-2h) could be fabricated as a triplet host emitter without the use of CBP [181]. Thus, using Al as the cathode, *Ir-2h* as the luminescent layer, 4,7-diphenyl-1,10-phenanthroline (DPA) as the electron-transport layer and bis[4-(*N*,*N*diethylamino)-2-methylphenyl]-(4-methylphenyl)methane (MPMP) as hole-transport layer on top of ITO/glass, intense electroluminescence at 525 nm with an efficiency of 20 cd/A and a maximum radiance of 4800 cd/m^2 was achieved.

To date, the bluest phosphorescent iridium complex is Firpic [182] which was reported by Thompson and his associates at Universal Display Corp. in the recent ICEL-3 conference (Fig. 20). In their device of [ITO/NPB/CBP + Firpic/BAlq/Mg:Ag], the external quantum efficiency was reported to reach 5.5% with EL efficiencies of 5 lm/W and 12 cd/A at 100 cd/m^2. Its EL emission peaks at 470 nm with a CIE coordinates of $x = 0.14$; $y = 0.30$ which is still somewhat cyan in color, but definitely bluer than those of Firppy. In the poster, it was also disclosed that a *t*-butyl-*iso*cyanide

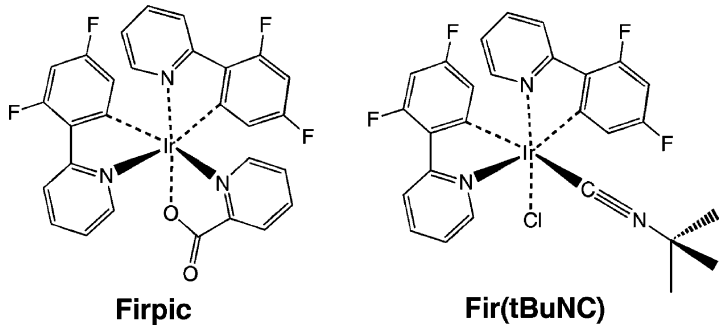

Firpic **Fir(tBuNC)**

Fig. 20. Blue-emitting phosphorescent materials.

(*t*-BuNC) ligated iridium complex (Fir(tBuNC)Cl) actually had a triplet blue photoluminescence peak at 450 nm in methylene chloride. But, unfortunately it was too unstable to be fabricated into a device. Both of these new blue iridium complexes were isolated as a mixture of *facial* and *meridonal* isomers.

Finally, by controlling exciton diffusion in the multi-layered OLED devices using 6% Firpic/CBP as the blue emitter, 8% $Bt_2Ir(acac)$/CBP as the yellow and 8% $Btp_2Ir(acac)$/CBP as the red emitters, high-efficiency white phosphorescent OLEDs have been reported just before submission of this review [183]. One of these white OLED devices which attained a maximum external quantum efficiency of $5.2 \pm 0.5\%$, maximum EL efficiency of 11 ± 1 cd/A, a maximum luminous efficiency of 6.4 ± 0.6 lm/W with $CIE_{x,y} = [0.37, 0.40]$ at 10 mA/cm^2 and a maximum luminance of 31,000 cd/m^2 at 14 V, is among the best ever reported to date [184–186].

It should also be mentioned that there appears to be growing interest and research effort in the academia to develop dendrimers which contain site-isolated chromophores [187] that can control charge-transport, exciton formation, fluorescence and intermolecular interaction [188]. These giant dendritic molecules synthesized by building convergently from a highly functionalized core through several generations have been demonstrated to form single-layered devices by solution processing. Although much work still needs to be done before this idea can be materialized and proven device worthy, the best performance of such dendritic OLED reported to date is based on the green phosphorescent *fac*-$Ir(ppy)_3$ cored dendrimers [189] shown in Fig. 21. A first generation dendrimer doped into the wide-gap 4,4′-bis(*N*-carbazolyl)biphenyl (CBP) host was shown to display a peak external quantum efficiency of 8.1% (28 cd/A) at a brightness of 3450 cd/m^2 and 5 mA/cm^2.

4. Charge injection and transport

In OLEDs, both operating voltage and luminance efficiency of the devices strongly depend on effective charge injection from the electrodes to the organic medium and charge transport in the organic materials. In general, to achieve the lowest possible voltage it is necessary to have Ohmic interfaces between the organic layers and the charge-injecting contacts and to maximize the drift mobility of both types of carriers. Furthermore, charge injection and charge transport also play an important role in optimizing the device efficiency of an OLED. An unbalanced injection results in an excess of one carrier type that does not contribute to light emission, and it can also result in an enhanced non-radiative recombination because of interactions of excitons with the charge carriers.

In general, the two processes are difficult to disentangle on the basis of the electrical characteristics of OLEDs. The charge-injection contacts are studied with three methods in the

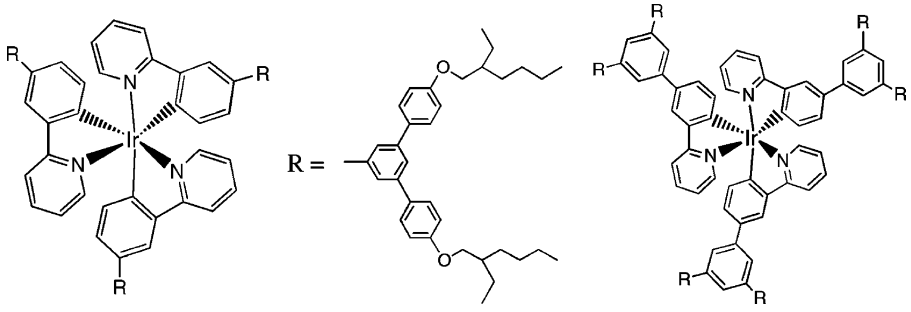

Fig. 21. Dendrimers of first and second generation containing $Ir(ppy)_3$.

literature: (1) determining the interfacial electronic structure and chemistry by photoelectron spectroscopy, (2) measuring the current–voltage (*I–V*) characteristics of a single-carrier device, and (3) comparing the device performance before and after some modifications.

Injection of charge from most electrode materials requires overcoming a barrier at the electrode/organic interface, and the nature of the interface is of paramount importance in determining device performance. Photoelectron spectroscopy has been extensively employed to determine the electronic structure and chemistry at the metal/organic interfaces. Dipoles, chemical reaction, and atomic diffusion are commonly observed in the near interface region. As a consequence, the determination of the carrier injection barrier is not a simple matter of calculating the difference between the metal work function and the energy levels of the organic solid owing to the presence of interfacial dipoles and chemical reaction.

The current that flows through a depleted semiconductor can either be limited by the semiconductor bulk or by its contact with an electrode. In the first case, the contact makes available as much current as the semiconductor bulk demands and the current is limited by intrinsic transport properties of the semiconductor. This is the space charge limited current (SCLC). By comparing the current measured in an electron- or hole-only device to the current calculated for SCLC, one can determine whether the contact is Ohmic or is injection limited. In conventional OLEDs, the hole current is limited by injection, and the electron current is strongly influenced by the presence of traps, owing to metal–organic interactions.

The vast majority of contact injection work reported in this review has been carried out on an OLED configuration. Namely, devices with and without some electrode modifications were tested side by side, and changes in the device performance were attributed to such modifications.

When both the cathode and anode are perfectly injecting, carrier mobility in organic materials becomes a limiting factor for voltage reduction. Moreover, even the current is limited by charge injection; the rate of injection is still proportional to the charge mobility in the organic material. Thus, developing new materials with high carrier mobilities and increasing electrical conductivities of organic materials by doping are particularly important.

4.1. Interface structures and chemistry

4.1.1. Energy level alignment

At metal/organic interfaces, the hole and electron barriers (ϕ_h and ϕ_e) depend on the position of the HOMO and LUMO of the organic film with respect to the metal Fermi level (E_F). When assuming vacuum level (VL) alignment, ϕ_h would be the difference between the ionization potential, IP and the metal work function ϕ_M, and ϕ_e would be the difference between ϕ_M and the electron affinity EA of the organic film. The values of IP and E_F can be separately determined for the metal and organic film by UPS, and the value of EA is usually estimated from the value of IP and the HOMO/LUMO gap obtained from optical measurements.

In the actual systems, the assumption of a common vacuum level is not valid [190]. For almost all the interfaces formed by depositing organic materials on metal surfaces under ultrahigh vacuum conditions, a dipole layer is formed at the metal–organic interface, owing to various origins such as charge transfer across the interface, redistribution of electron cloud, interfacial chemical reaction, and other types of rearrangement of electronic charge [191]. With such interfacial dipole formation, there will be an abrupt shift of the electrical potential across the dipole layer, leading to a shift Δ of the virtual VL at the interface. The value of Δ is determined by the magnitude of the dipole.

The schematic of an organic–metal energy diagram with and without interface dipole is given by Kohn and their coworkers, and reproduced in Fig. 22. The electronic structure is illustrated in

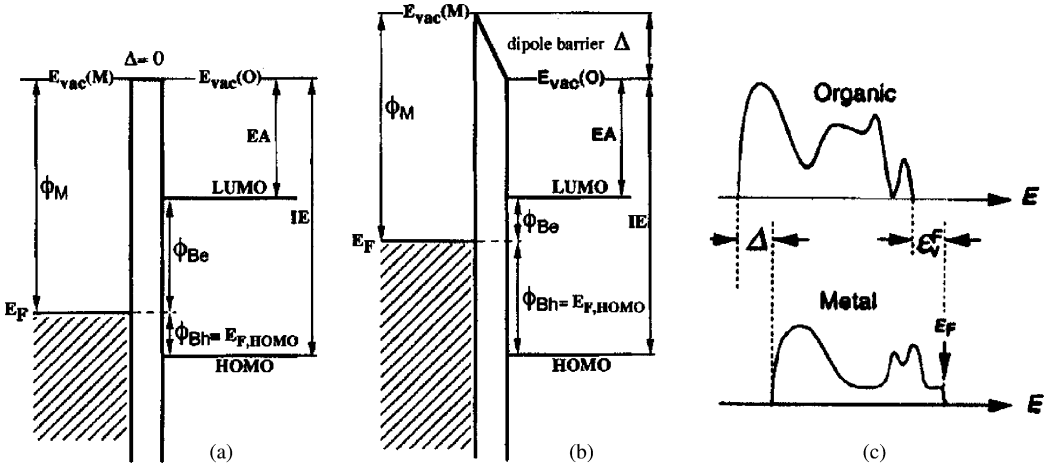

Fig. 22. Schematic of an organic–metal interface energy diagram (a) without and (b) with an interface dipole and (c) UPS spectra of metal and organic [190,191].

Fig. 22a corresponding to the alignment of vacuum levels across the interface ($\Delta = 0$) and giving $\phi_h = \text{IP} - \phi_M$ and $\phi_e = \phi_M - \text{EA}$. In the finite dipole case of Fig. 22b, ϕ_h and ϕ_e are given by $\text{IP} - \phi_M + \Delta$ and $\phi_M - \text{EA} - \Delta$, respectively. This modification is of critical importance for carrier injection in OLEDs. The commonly observed energy level alignment in Fig. 22b corresponds to a positive change on the organic side and a negative charge on the metal side at the interface.

The interface dipole scenario was originally proposed by Seki and coworkers [192,193] and has received extensive support from other research groups [194–196]. The energy level at metal–organic interfaces is determined in ultrahigh vacuum by UPS with $h\nu = 21.22$ or 40.08 eV. The metals of interest are evaporated on silicon, and then the organic–metal interfaces are formed by incremental molecular beam evaporation of organics. Fig. 22c represents the UPS spectra of metal and organic. For metals the right-hand cutoff shows the Fermi edge and the left-hand cutoff corresponds to the vacuum level. By depositing increasing amount of organic materials the emission from the metal becomes suppressed and the spectrum is changed to that of the organic materials. The right-hand cutoff now corresponds to the HOMO of the organic materials, and the shift from the Fermi edge of the metal gives the relative position of the HOMO from the Fermi level of the metal ($E_{\text{F,HOMO}}$ in Fig. 22b). The shift of the left-hand cutoff corresponds to the lowering vacuum level by the deposition of the ultrathin organic film.

Experiments by a number of research groups indicate that dipoles are found at all metal–organic interfaces, while the dependence of the interface dipole magnitude on the metal work function varies from organic to organic [190,197,198]. The experimental values of $E_{\text{F,HOMO}}$ are plotted in Fig. 23 as a function of metal work function for two organic materials. The commonly used electron-transport and hole-transport materials are Alq_3 and *N*,*N*′-diphenyl-*N*,*N*′-bis(l-naphthyl)-1,1′biphenyl-4,4″ diamine (α-NPD), respectively. The HOMO levels are arbitrarily aligned at $E = 0$, and the LUMO levels are positioned according to the optical gap of each material. The oblique dashed line represents the zero-dipole. The presence of dipoles at the metal–organic interface shifts the surface vacuum level to lower energy, facilitating the escape of electrons from the surface. In the literature two trends are clear: (1) depositing the organic layer on metals always causes the lowering of the VL and (2) the shift is mostly a monotonic function of ϕ_M.

Despite the evidence presented by the groups of Seki and Kahn, others have proposed that the UPS data can be explained by band bending [199,200]. Therefore, it is essential to study the initial

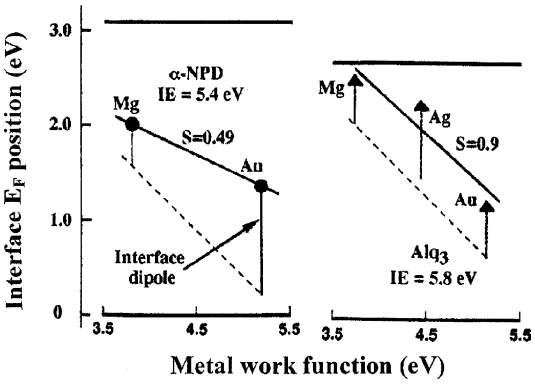

Fig. 23. Plot of $E_{F,HOMO}$ as a function of metal work function for α-NPD and Alq_3 [190].

stages of interface formation and the shifting of energy levels over some distance in the organic film. In the study of three different metal-quinolate derivatives (Gaq_3, Alq_3, and $Almq_3$) on Ag using photoelectron spectroscopy, consistent results were observed at all three interfaces, which exhibited strong energy level shifts within the first molecular layer, followed by a nearly 'flat-band' condition [201]. Therefore, the energy levels observed after the first layer is completed could be used to describe charge injection barriers. The results are similar to the finding by Seki et al. [202]. In their experiments, Au, Ag, Cu, Mg or Ca was evaporated on Si substrate, and then TPD was deposited in a stepwise manner. The energy separation between the E_F of the metal and the IP of the organic layer ($E_{F,HOMO}$) was measured as a function of layer thickness by using a Kelvin probe. In all cases, a sharp initial decrease was observed corresponding to the vacuum level shift and then the separation remained unchanged up to 100 nm. The sharp initial decrease indicates the formation of a dipole layer that has been established in UPS studies. The lack of thickness dependence suggests the absence of band bending.

In UPS analysis, the metal–organic interface is formed in UHV. For examining the effect of atmosphere, a metal substrate prepared under UHV condition was exposed to air for a short period, and reloaded into the UHV system before depositing organic films on it. The results for interfaces formed by depositing TPD on air-exposed metal surfaces also showed an initial sharp drop and a flat distribution with increasing thickness [202]. The values of the VL shift for TPD are shown in Fig. 24, in comparison with the values for clean metal surfaces. The absolute values of the initial drop are significantly reduced from those for clean substrates, possibly due to the passivation of the metal

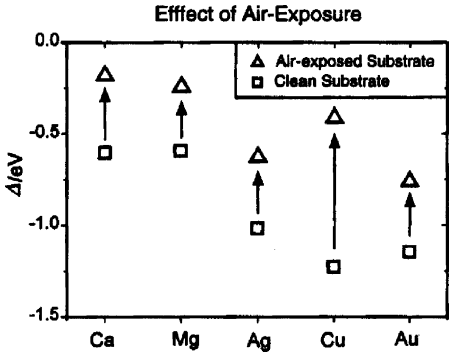

Fig. 24. The effects of exposing the metal surface to air prior to the deposition of TPD [202].

surface either by oxidation or contamination in air. These results clearly demonstrate the importance of atmosphere for interface formation and related electrical properties. However, the magnitude of the VL shift is still quite large, indicating that the interfacial dipole formation is also important in real devices.

In the literature, the studies of organic thin films on metals are much more common than the reverse. In general, the interfaces formed are not equivalent. In OLEDs, Alq_3 is extensively used as the electron-transport/emissive material and MgAg is commonly used as the electron-injecting cathode. The morphology and chemistry of interfaces between these two materials depend on their deposition sequence. Alq_3 deposited on Mg forms a more abrupt interface than Mg deposited on Alq_3, which reacts with the core of the molecule and diffuses into the organic layer [203]. The asymmetry is explained as being due to the differences in heats of adsorption and surface bond strengths of the organic and the metal. When depositing an organic on a metal, the strongly bonded surface atoms are not affected by the low-energy organic molecules, which are typically evaporated at relatively low temperatures. In contrast, the molecules in an organic film form a weakly bonded van der Waals solid, which are easily disturbed by the deposition of energetic metal atoms from an evaporation source at elevated temperatures. This is a very important factor, but makes the analysis of the data rather complicated. Moreover, the conventional OLED structure is formed by deposition of a cathode metal onto an organic layer. Thus, it is not clear that the results on systems prepared in the reverse order have some significant relevance to the performance of actual devices with a conventional structure.

4.1.2. Interactions at metal–organic interfaces

The use of a low-work function metal (K, Na, Li, Mg and Ca) cathode is highly desirable for forming an effective electron-injecting contact, however, these metals are poorly suited because of their high chemical reactivity. The study of such an interface between these metals and the organic film Alq_3 revealed strong interactions [204–206]. Mason et al. compiled data generated in different research groups and mad a comparison and interpretation [207]. In Fig. 25A, the low binding energy (BE) region of the UPS spectra is shown for the five metals on Alq_3. In all cases, the original HOMO

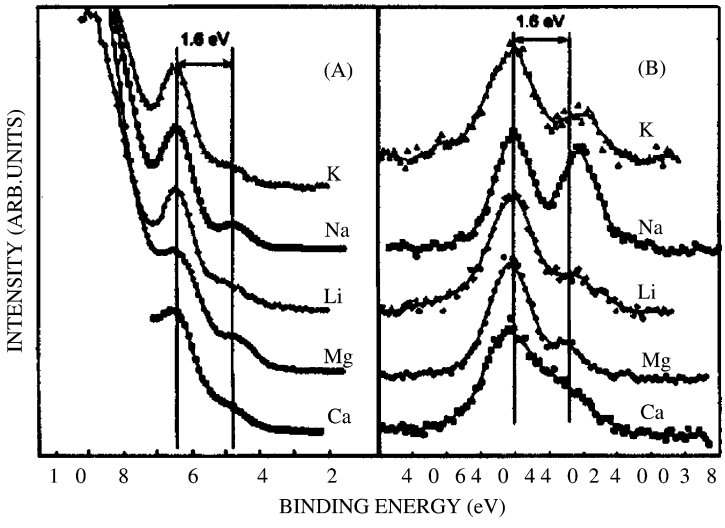

Fig. 25. (A) The HOMO region of Alq_3 after deposition of group I and group II metals and (B) the N 1s region for the same series of metals [207].

level is shifted to higher binding energy, and a new gap state is formed in the forbidden gap at an energy of ~1.6 eV above the shifted HOMO level. Combined with theoretical calculation, the results indicate the reaction of the metals with Alq_3 to form Alq_3^- anions. The other common spectral feature is the splitting of the N 1s spectra (Fig. 25B) for the same set of five metal overlayers on Alq_3.

If the deposition of Ca is increased above a critical coverage of 0.4 nm, a destructive reaction occurs in which the metal appears to attack at the phenoxy oxygen and destroy the Alq_3 molecular structure [208,209]. Unlike Ca, Mg shows no evidence of destructive reaction regardless of the amount of metal deposited [210]. Theoretical studies indicate that the Mg–Alq_3 interaction is mainly related to the disturbance of the aluminum atomic orbital, rather than a direct contribution of Mg [211].

The results indicate that the alkali and alkaline earth metals are too reactive for use in device fabrication. From the standpoint of commercial device fabrication, there would be significant advantage to utilize a pure Al cathode. In addition, UPS studies of Alq_3 deposited on Al show a very small barrier to electron injection. However, Al makes a fairly poor cathode in Alq_3-based devices when compared to the commonly used MgAg cathode. In an effort to understand the relatively poor electron injection in Al/Alq_3-based devices, Le et al. [212] have studied the interface formation produced from Al deposition onto Alq_3. All core levels of oxygen, nitrogen and carbon in XPS analysis showed significant broadening and shifting to higher binding energy with increasing aluminum deposition. A detailed analysis suggested that aluminum reacts preferentially with the quinolate oxygen, and then with nitrogen. The experimental results are consistent with their quantum chemical calculation using density-functional theory (DFT). In UPS analysis, deposition of an aluminum layer as thin as 0.02 nm induced a significant change in the valence spectrum of Alq_3 and formed new states, which extended into the energy gap. The features of the Alq_3 structure have virtually vanished after deposition of 0.07 nm aluminum. Both the XPS and UPS are consistent with a destructive reaction between Al and Alq_3, which is expected to cause poor device performance.

Deep Al penetration into Alq_3 has also been revealed by Rutherford backscattering (RBS) measurements on a sample consisting of a graphite substrate, an Al intermediate layer (3 nm), and an Alq_3 surface layer (35 nm) [213]. RBS profiling revealed Al atoms in the surface region with an amount of $\sim 1.6 \times 10^{15}$ per cm^2 (or ~0.25 nm). Photoluminescence measurements indicated that the Al penetration had a strong correlation with Alq_3 photoluminescence quenching.

4.2. Cathodes

4.2.1. Elemental metals

As the determination of the electron injection barrier is not a simple matter of calculating the difference between the metal work function and the electron affinity of the organic solid owing to the presence of interfacial dipoles, it is of great interest to find how well electron injection is correlated with the work function of the cathode. Stossel and coworkers have investigated the Alq_3-base OLEDs prepared at 5×10^{-9} mbar with the cathode work function ranging from 2.63 to 4.70 eV [214,215]. It is clear in Fig. 26 that the lower the work function of the metal is, the higher the current density will be, while the use of a metal having a work function below 3.6 eV offers no additional benefits to the luminance efficiency as compared to Mg. It is postulated that the Alq_3 layer adjacent to the cathode might be altered due to interactions with the highly reactive metals, and consequently an increased fraction of excitons is returning to ground non-radiatively. It is also evident in Fig. 26 that the efficiencies of the devices prepared at HV condition (9×10^{-6} mbar) are considerably lower

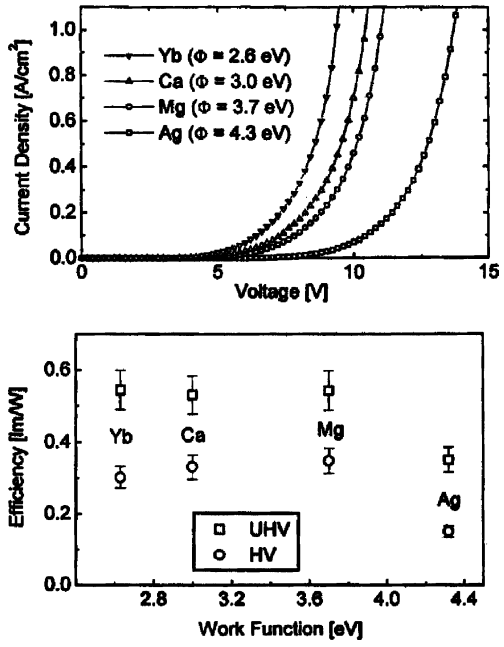

Fig. 26. Upper part: current–voltage characteristics of OLEDs prepared under UHV and lower part: luminance efficiency of OLEDs prepared under UHV and HV [215].

than that measured on the devices fabricated at UHV conditions. By referring to the work by Seki, this decrease is attributed to the reduction in the magnitude of interfacial dipoles, which unfavorably affects electron injection [202]. The results clearly demonstrate that in spite of strong interactions at the electrode/organic interface, the size of the barriers for carrier injection still qualitatively scales with the electrode work function.

4.2.2. Metal alloys and compounds

The attempt to use Ca, K, and Li for effective cathode materials revealed that they exhibit poor corrosion resistance and high chemical reactivity with the organic medium. Thus, a variety of low-work function metal alloys such as Mg–Ag and Al–Li are used for cathodes.

4.2.2.1. Mg–Ag. Mg–Ag with a volume ratio of 10:1 is commonly used as a low-work function electron-injecting cathode on Alq_3. The addition of Ag into Mg considerably improves its chemical stability in the atmosphere and increases its sticking coefficient onto Alq_3 upon deposition [107]. Mg experiences no substantial diffusion under device operation and has no significant effects on luminance decay with operation time.

Mg on Alq_3 forms a broader interface than Alq_3 on Mg and reacts with the core of the Alq_3 molecule. One previous study reported highly asymmetric *I–V* characteristics for glass/MgAg/Alq_3/MgAg structures fabricated under 10^{-5} Torr vacuum. The results showed that the electron current injected from the top metal electrode is two to three orders of magnitude larger at equal voltage than the current injected from the bottom electrode. It was suggested that the asymmetry was the result of the disruption of the organic layer by the deposition of the metal, and that the injection enhancement was in part due to defects induced by the deposition of MgAg on Alq_3. However, a recent study revealed symmetric *I–V* characteristics when the structure of glass/MgAg/Alq_3/MgAg was fabricated under stringent vacuum conditions [216].

4.2.2.2. Li–Al. Li is a low-work metal and considered as an effective cathode to achieve efficient electron injection in OLEDs, however, Li can strongly react with Alq_3 and is highly reactive under ambient conditions. When a bilayer cathode of Li (0.3 nm)/Al (120 nm) is acting as an electron-injecting contact on an Alq_3-based OLED, the devices failed within seconds at a constant brightness of several hundreds cd/m^2 [217]. This is attributed to Li diffusion into the organic films, which creates non-radiative recombination centers.

One solution is to use a relatively stable alloy of Al–Li in the formation of electron-injecting contacts. The devices having a Li-doped Al cathode show improved electron injection and durability, while it is difficult to achieve a cathode with a desirable concentration of Li (around 1%) because of a pronounced difference in vapor pressure between Li and Al. Sputtering deposition is then employed for the formation of Li-doped Al cathodes in OLEDs. Since OLEDs are sensitive to radiation damage caused by the sputtering process, a buffer layer of CuPc is utilized to minimize the radiation damage inflicted on the OLED organic layer stack during the cathode deposition [218]. Although the CuPc layer forms an electron-injection barrier with the underlying Alq_3 layer, Li diffusion from the cathode materials into CuPc and subsequent accumulation at the CuPc/Alq_3 interface lead to the reduction of the injection barrier. The device prepared by sputtering deposition of an Al–Li cathode on a layered structure of ITO/NPB/Alq_3/CuPc exhibited almost identical characteristics to the control device with a thermally evaporated MgAg cathode on Alq_3. The devices showed superior operational stability with a half-life time greater than 3800 h at 20 mA/cm^2. The excellent device performance, the compatibility and applicability to alloy materials, and the simplified deposition process make sputtering very attractive in cathode preparation for high-throughput production [219].

4.2.2.3. Alkali metal compounds/Al. Alkali compounds have been combined with a capping Al layer to form an efficient electron injector. With an optimal thickness of 0.3–1.0 nm, both voltage reduction and efficiency enhancement were observed for Li_2O, $LiBO_2$, K_2SiO_3 or Cs_2CO_3 [220]. Those compounds were believed to decompose during deposition and produce Li_2O, K_2O, and Cs_2O at the Alq_3/Al interface, respectively. As compared to thermally evaporated Li–Al, device performance is more reproducible because the optimal quantity (0.3–1.0 nm) of the alkali metal compounds can be readily controlled in OLEDs. Similar effects were observed when using alkali metal acetates (CH_3COOM), where M = Li, Na, K, Rb, and Cs [221].

The physical origin of the improved EL characteristics is not certain at present, but it is most likely due to the dissociation of alkali metal oxides at the Alq_3/Al interface. The released alkali metal atoms may react with Al to lower its work function, resulting in enhanced electron injection. As a consequence, it leads to more balanced charge injection and higher EL efficiencies.

4.2.3. Al_2O_3/Al

Besides the use of an ultrathin intermediate layer of alkali compounds, a 1.2 nm thick Al_2O_3 interposed between Alq_3 and Al was also reported to improve electron injection and luminance efficiency [222–224]. Since Al_2O_3 is chemically stable, the improvement is attributed to electron tunneling and removal of exciton-quenching gap states that are intrinsic to the Alq_3/Al interface. An alternative explanation comes from UPS measurements on an Al/Al_2O_3/Alq_3 structure by depositing Alq_3 on an air-posed Al surface [225]. The energy difference between the Fermi level of the Al layer and the LUMO edge of the Alq_3 layer was determined to be 0.4 eV for the Al/Al_2O_3/Alq_3 interface and 0.6 eV for the Al/Alq_3 interface. Thus, interposing an Al_2O_3 buffer layer between Alq_3 and Al can reduce the electron injection barrier, and consequently enhance electron injection in OLEDs.

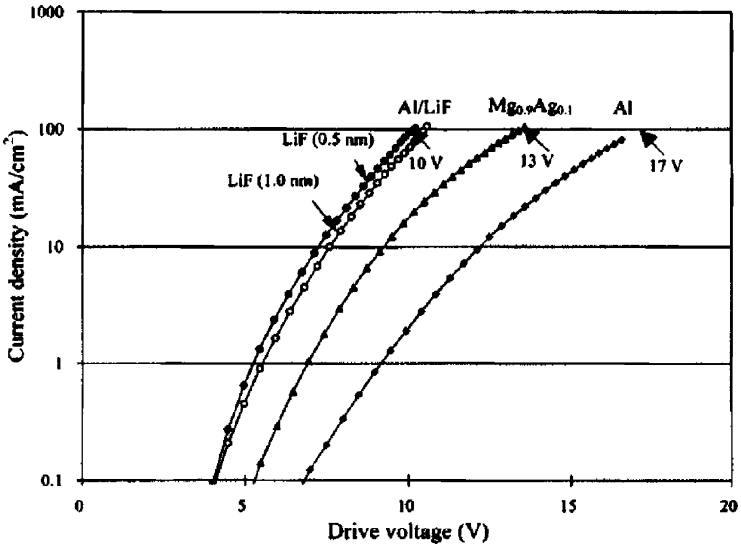

Fig. 27. Current–voltage characteristics of three OLEDs using Al, MgAg, and LiF/Al as a cathode, respectively [226].

4.3. Fluoride/Al

4.3.1. LiF/Al

4.3.1.1. Bilayer cathode. LiF exhibits pronounced differences from those reactive alkali metal compounds, as it is thermodynamically stable with respect to either Al or Alq_3. Nevertheless, an effective Al cathode for OLEDs could be constructed by interposing a thin (0.1–1.0 nm) LiF layer between Al and Alq_3, despite its high work function [226,227]. Devices with the bilayer electrode showed significantly better *I–V* characteristics and higher EL efficiencies than that with a standard MgAg cathode (see Fig. 27). The cathodes have better chemical stability against atmospheric corrosion and are compatible with Si device processing.

The improvement of device performance by interposing an ultrathin LiF between Al and Alq_3 stimulated a great deal of interest. In OLEDs, the majority carriers are holes, owing to their higher mobilities and typically smaller injection barriers. Thus, lowering the barrier height to electron injection is especially important, as it leads to a better balance of electron and hole currents and results in a dramatic increase of the luminance at a fixed bias voltage.

The bilayer cathode has been applied to various organic materials to form an effective electron injector. For instance, a blue OLED with a LiF/Al cathode on an emissive/electron-transport layer of 4,4′-bis(2,2-diphenylvinyl)-1,1′-biphenyl (DPVBi) had an external quantum efficiency of 1.4%, which represented a 50-fold increase in the device efficiency compared to a device with an Al only cathode [228]. A similar observation was reported in red OLEDs with a Eu-based emitter [143]. In the device of [ITO/TPD/Eu $(TTFA)_3$(phen):PBD/PBD/MgAg], the output was rarely seen even at 15 V, however, external quantum efficiency exceeding 1% and light output higher than 320 cd/m^2 were achieved when a LiF layer was inserted between the PBD and MgAg.

The bilayer Al/LiF on Alq_3 forms a shallow contact with its thickness of 1 nm or less. The formation of such a shallow contact was confirmed by examining a series of OLEDs with a configuration of ITO/NPB/Alq_3/LiF (0.3 nm)/Al/Ag (50 nm), where the thickness of the Al layer was varied from 0.1 to 0.6 nm, and the Ag was used to reduce the sheet resistance of the cathode [229].

An Al/LiF bilayer with an Al layer as thin as 0.1 nm was sufficient to form an effective electron-injecting contact at the Alq_3/Ag interface, as its performance was almost identical to that obtained from a control device having a cathode of LiF (0.3 nm)/Al (100 nm). The results are in good agreement with the experimental findings by various surface analyses, in which pronounced changes in spectra take place by adding a 0.02 nm thick Al layer on Alq_3/LiF. The shallow contact nature of LiF/Al Alq_3 has been utilized for interface engineering to enhance electron injection from a high-work function cathode to Alq_3 and improve electron-transport from a high-electron affinity material to a low-electron affinity material. The use of interface engineering has resulted in the fabrication of various novel OLEDs, including an ITO-free surface-emitting OLED [229], a low-voltage OLED [230], and an OLED exhibiting substantial reduction in ambient-light reflection [231,232].

One of the examples is the use of an oxygen-deficient zinc oxide or an Al–Si oxide to form an absorbing layer between a highly reflective Al cathode and an organic electron-transport layer of Alq. The use of a semitransparent conductive oxide with an ultrathin bilayer of LiF/Al between the absorbing layer and the Alq layer can form an OLED with sufficient reduction in ambient-light reflection from the mirror-like surface of the metal electrode through optical destructive interference. The thin LiF/Al bilayer is of critical importance in this case to enhance electron injection from the absorbing layer into the Alq layer.

As LiF/Al forms an effective electron-injecting contact, it is of great interest to determine whether the contact is Ohmic. Electron injection and transport in an electron-only device formed from Alq_3 sandwiched between two LiF/Al electrodes were investigated [233]. *I–V* characteristics of the devices were compared with those obtained from the device having a MgAg or a pure Al cathode. The current density of the devices with a LiF (0.1–0.2 nm)/Al cathode nearly reached the theoretically predicted values of space charge limited currents at elevated operating voltages. The current is thus dominated by transport properties of the bulk materials rather than injection limited, implying the Ohmic nature of the bilayer cathode on Alq_3.

4.3.1.2. Composite cathodes. A LiF-doped Al layer was utilized as a composite cathode on Alq_3 [234]. The composite electrodes even at a 1% LiF yielded superior device performance, as compared to an Al cathode directly deposited on Alq [235]. From Fig. 28 it is evident that the use of a doped cathode to replace the conventional bilayer electrode of LiF/Al exhibits almost the identical effect on both current–voltage and luminance–current characteristics.

It has also been reported that a device with a LiF-doped Alq_3 layer underlying an Al cathode produced luminance efficiencies slightly lower than that with a LiF/Al cathode, but they were still much higher than a device with an Al cathode [236]. Both cases indicate that LiF needs not to be in the form of a layer for contact formation, as long as the three components of Alq_3, LiF and Al co-exist.

4.3.2. CsF

When replacing LiF by CsF or alkaline earth fluorides [237,238], the effects of CsF on OLEDs are almost identical to that of LiF, while the improvement by the use of alkaline earth fluorides is less significant. The turn-on voltage of OLEDs with alkaline earth fluorides was found to be associated with electronegativity of their metal constituent. Although CsF and LiF bring the same beneficial effects to Alq_3-based OLEDs, the mechanisms differ significantly. CsF reacts with Al to release Cs, whereas the dissociation of LiF in the presence of Al is thermodynamically not allowed, so that the CsF/Al cathode is applicable to more organic materials than LiF. This is particularly true with polymer LEDs.

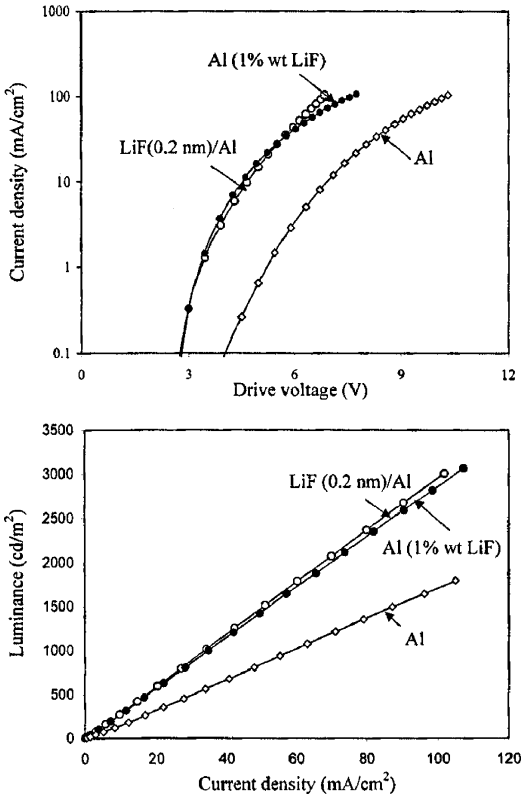

Fig. 28. Current–voltage characteristics (upper part) and luminance–current characteristics (lower part) of OLEDs with an Al cathode containing 1 wt.% LiF, a LiF (0.2 nm)/Al cathode, and an Al cathode, respectively [235].

4.3.3. Mechanisms

Although LiF/Al electrodes are widely used in OLEDs, the underlying mechanisms are still under investigation. Several mechanisms have been proposed in the literature, and are discussed in the following sub-sections.

4.3.3.1. Shift of light-emitting zones. The increased electron injection leads to a shift of the light-emitting zone to a region close to the HTL/ETL interface. This shift was proposed to be the reason for the improvement of emission efficiency as it might cause constructive interference of light in the device [239]. However, as the efficiency enhancement is commonly observed irrespective of the total thickness of Alq_3, the shifting light-emitting zone is not likely to be the dominant mechanism.

4.3.3.2. Tunneling and reduction in gap states. When a LiF layer is added, considerable voltage can be dropped across this layer, which can align the Fermi level of Al with the LUMO of Alq_3 and enable direct tunneling of electrons though the thin LiF layer. Moreover, the use of a thin insulating layer is thought to remove gap states by avoiding a direct contact between Al and Alq_3. Those gap states have been suspected to be one of the physical origins behind the poor performance in Al-base OLEDs [228].

However, neither the tunneling argument nor the gap states scenario can explain the effects of a composite cathode on device performance. In the case of OLEDs with a composite cathode, LiF does not form a continuous film and there is still a direct contact between Al and the Alq_3, therefore, the improvement indicates that some other mechanisms are operating.

4.3.3.3. Interfacial dipoles. UPS has been employed to study electronic structures of Al/LiF/Alq_3 and Al/Alq_3 interfaces. Shifts of the highest occupied molecular orbital level and the vacuum level of the Alq_3 layer due to the presence of a thin LiF layer were observed. A dipole was determined at the Al–Alq_3 interface with a value of 1.0 eV for Alq_3 on Al and 1.6 eV for Alq_3 on Al/LiF [240]. This result implies that a thin LiF layer at the Al/Alq_3 interface is able to reduce the barrier height for electron injection from the Al to Alq_3. However, in a conventional OLED the cathode is formed by depositing Al or LiF/Al onto Alq_3, and thus it is not clear whether the data acquired by UPS have a significant relevance to the performance of actual devices.

4.3.3.4. Lowering Al work function in the presence of water molecules. It has been observed that the effective work function of Al decreases dramatically with less than one monolayer of LiF coverage on the Al surface. One possible explanation is that LiF dissociates during thermal deposition in the presence of water molecules, and forms a Li–Al alloy at the interface. It has also been attributed to the formation of a large dipole at the Al/LiF interface resulting from H_2O chemisorptions [241]. However, a recent study using high-resolution electron energy loss spectroscopy (HREELS) revealed neither the presence of water molecules at the LiF/Al interface nor the dissociation of LiF on Al.

4.3.3.5. Chemical reaction in the presence of water molecules. The mechanisms of enhanced electron injection into the ETL of Alq_3 via LiF interlayers were studied employing secondary ion mass spectroscopy (SIMS) [242]. SIMS depth profiles on a specimen of glass/Alq_3 (100 nm)/LiF (0.5 nm)/Al (100 nm) showed that the ^{19}F rate dropped quickly with increasing depth in the Alq_3, while the ^{6}Li and ^{7}Li signals remained high throughout the whole Alq_3 layer, indicative of a chemical reaction in which fluorine reacted with the Al and the liberated lithium diffused into the Alq_3 layer. As the reaction is thermodynamical, the presence of water is then proposed to account for the release of Li in the presence of Al.

4.3.3.6. Dissociation of LiF in the coexistence of Alq_3, LiF and Al. Mason et al. [207] studied the electronic structure and chemistry of interfaces between Alq_3 and Li, Na, K, Cs, Ca, and Mg by XPS and UPS. Quantum chemical calculations at the density-functional theory level predict that the Alq_3 radical anion is formed upon reaction with the alkali metals. The anion formation results in a splitting of the N 1s core level and formation of a new state in the previously forbidden energy gap. Virtually identical spectra are observed in the Al/LiF/Alq_3 system, leading to the postulation that Alq_3^- anions are formed by releasing Li from LiF when the three constituents are present. Molecular orbital calculations including the modified neglect of differential overlap (MNDO) and the DFT indicate that the release of Li from LiF and the subsequent reaction of Li with Alq_3 to form the Alq_3 anions are energetically favorable [235].

The dissociation of LiF and subsequent formation of the Alq_3 radical anions are reasonable, however, the extremely low ionization cross-section of the Li 1s emission and the binding energy shifts for small metallic clusters make it virtually impossible to determine the chemical state of Li in UPS analysis. HREELS was then employed to investigate the interfacial reaction [235]. In Fig. 29, the HREELS spectrum at the bottom showed the features of Alq_3. After depositing 0.26 nm of LiF on Alq_3, a strong peak assigned to the LiF loss peak appeared at around 62 meV. With 0.23 nm of Al on LiF/Alq_3, pronounced changes took place in the HREELS spectrum. The intensity of the loss peak corresponding to the LiF layer was substantially reduced, while the reduction in the loss peak of Alq_3 was insignificant. The striking difference in the loss peak of the LiF layer before and after Al deposition provides a direct evidence of the dissociation of LiF in the coexistence of Alq_3 and Al with LiF.

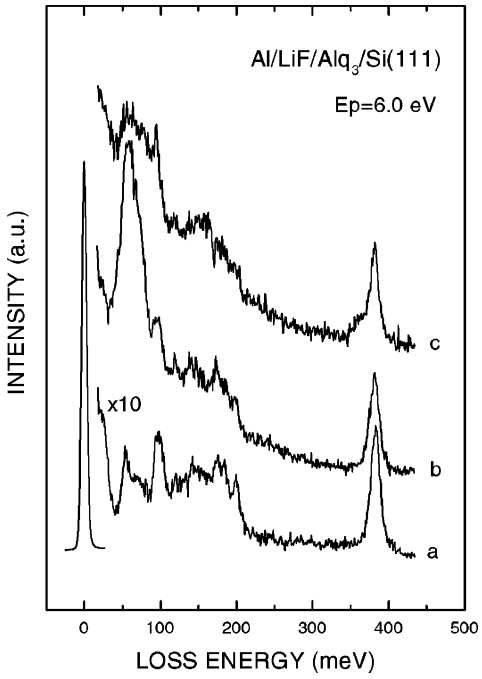

Fig. 29. HREELS spectra of (a) Si/Alq (2 nm), (b) Si/Alq (2 nm)/LiF (0.26 nm) and (c) Si/Alq (2 nm)/LiF (0.26 nm)/Al (0.23 nm) [235].

4.3.4. LiF/Al and CsF/Al on conjugated polymers

As LiF/Al and CsF/Al on Alq_3 form an effective electron injector for OLEDs, their effects on PLEDs have been extensively studied [243–245], and the results provide more insight into its mechanism. With a PLED having an emissive/electron-transport layer of poly(9,9-dioctyl-fluorene) (PFO), strong enhancement of electron injection is observed for CsF/Al on PFO, but the effect is much less significant for LiF/Al on this conjugated polymer. The pronounced differences in electrical properties are associated with their different interfacial chemistry.

UPS and XPS measurements indicate doping takes place when depositing Li on PFO, which is similar to Li on Alq_3. Inclusion of a thin LiF layer between the PFO film and an Al cathode rapidly decreases Al–PFO interactions, however, there is no indication of LiF dissociation at the PFO/Al interface [246]. In contrary, CsF dissociates in contact with Al, and thus Al on PFO/CsF causes PFO doping at the interface by the liberated Cs, resulting in enhanced electron injection [247]. The results clearly support the dissociation model established in the case of LiF/Al on Alq_3.

Recently, several research groups reported a sizable reduction in barrier heights for PLEDs with a LiF/Al cathode although LiF dissociation was unexpected in the devices [248]. Furthermore, both the luminance efficiency and operating voltage remained almost unchanged when the thickness of LiF was progressively increased from 1 to 6 nm. It appears that more work is required to clarify this issue.

4.4. Anodes

In an OLED, the barrier to hole-injection from an electrode is normally taken as the energy difference between the electrode work function and the ionization potential of the organic. This is generally a very poor approximation and has been shown to be quantitatively incorrect for many

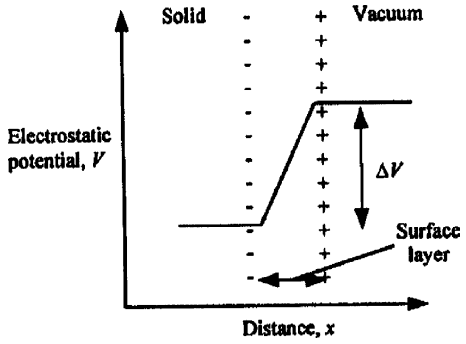

Fig. 30. Variation in electrostatic potential by a surface dipolar layer [255].

electrode/organic interfaces. Moreover, recent experiments on some new hole-transport materials showed that with OLEDs on ITO glass the device turn-on voltage and quantum efficiency were not correlated well with the ionization potential of the hole-transport materials, indicating that injection of carriers cannot be fully controlled by simply varying the energy-offset barrier at the electrode [54]. Other factors, such as good adhesion between the organic layers and ITO and the function of defect states at the interface between the organic layer and the electrode, need to be taken into consideration. Even so, limited data on ITO still indicate that the barrier to hole-injection does appear to qualitatively track the anode work function. Since work function is a surface property, there is some latitude in ''engineering'' its value by surface treatment.

4.4.1. Surface treatments of ITO

The work function of a metal is strongly influenced by the electrostatic conditions at its surface. The work function shift $\Delta\phi$ induced by a uniform dipolar surface layer is determined by the change in electrostatic potential (ΔV) created at the surface and can be derived from classical electrostatics as $\Delta\phi = -\Delta V = -eN(\mu_{mol}/\varepsilon_r\varepsilon_0)$, where N is the surface number density, ε_r the dielectric constant of the polar adsorbate molecules, and μ_{mol} is the molecular dipole normal to the surface [249]. In Fig. 30, the dipole is directed into the surface, thus reducing the work function. When the direction of the dipole is reversed, the work function is increased. Therefore, by using polar adsorbate molecules on ITO with the dipole oriented outward from the surface, an artificial dipolar layer is formed and the work function can be manipulated. The approaches include appropriate surface treatments of ITO by acids, SAMs and oxygen plasma.

4.4.1.1. Acid and base treatments. The chemical adsorption of acids and bases on ITO significantly affects its work function. Acid treatments yield work function shifts to higher values with respect to the non-treated cleaned ITO surface [250,251]. The shift is highest for phosphoric acid (H_3PO_4) with a value of $\Delta\phi = 0.7$ eV. In base treatments, the work function shifts to lower values. The biggest shift is obtained from tetrabutylammonium hydroxide ($N(C_4H_9)_4OH$) with a value of $\Delta\phi = -0.7$ eV. These dramatic shifts are indicative of a double ionic surface layer. Fig. 31 is a schematic illustration of the monolayer absorption of acids and bases on the ITO surface. A mineral acid will protonate the surface, and the remaining anion is likely to assemble on top of the adsorbed protons, giving rise to a surface dipole. Such a construction is shown schematically in Fig. 31a indicating the associated vacuum level shift. Similarly, the base will dissociate into a surface bound hydroxyl group and its conjugate base, forming an ionic double layer of opposite sign to the one formed by the acids (Fig. 31b). The associated vacuum level shift is now in the opposite direction.

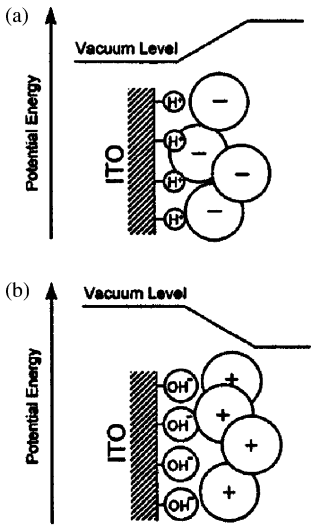

Fig. 31. Schematic illustration of the monolayer absorption of (a) acids and (b) bases onto ITO surface. The corresponding qualitative vacuum level shifts are also indicated in the graph [250].

However, the acid treatment is not a reliable approach to enhance hole-injection in OLEDs. For instance, the vacuum level drops rapidly when a thin layer of NPB is deposited on a treated ITO [252]. The abrupt decrease of the work function is attributed to the reaction of the NPB nitrogen with the proton of the adsorbed acid at the ITO surface. As a consequence of this reaction, the initial dipole at the acid-treated ITO surface partly loss its strength, resulting in a decrease in the ''effective'' work function. Tuning the work function of ITO has also been demonstrated by chemical modification of its surface with $–SO_2Cl$, –COCl, and $–PO_2Cl_2$ binding groups of *p*-substituted benzene derivatives [253].

4.4.1.2. SAMs. Hole-injection in OLEDs can be improved using SAMs to manipulate the energy level offset at the ITO–HTL interface. By using polar adsorbate molecules with the dipole oriented outward from the surface such as (4-nitrophenyl)phosphonic acid (4-NPPA), an artificial dipolar layer is formed and the work function is increased in excess of 0.3 eV [254]. Hatton reported a protocol for the reproducible silylation of ITO-coated glass using small molecule chlorosilanes, resulting in superior device performance. Unlike phosphonic acids, chlorosilanes are known to adhere to oxide surfaces via a covalent bond, and so the silylated ITO electrodes are expected to exhibit improved durability [255].

SAMs provide a method of tuning the work function of the ITO electrode to the HOMO of the HTL, thus improving device performance. However, unlike the atomically flat crystal surfaces used in most investigations with SAMs, ITO has a rugged surface, which is expected to limit adsorbate mobility and disrupt the circulation of solution over the surface, which are necessary for achieving long-range order.

4.4.1.3. Plasma treatments. It is well recognized that oxidative treatments such as oxygen plasma or UV ozone could dramatically enhance hole-injection and increase device reliability [256]. Neither addition nor removal of surface hydroxyl functionality account for the observed performance changes. Mason et al. reported that oxidative treatments incorporate more oxygen onto the surface, and the work function correlates well with the oxygen addition. The increase in the work function is attributed to the

presence of an interfacial dipole resulting from a surface rich in negatively charged oxygen [257]. Milliron et al. proposed that an increase in the ITO surface dipole layer by simple oxidation of Sn^{IV}–OH may account for the observed change in O-plasma-treated ITO [258]. The ability of modifying only the near surface region of the ITO allows us to maintain the bulk conductivity necessary for low-voltage operation and increase the work function of the ITO surface to enhance the hole-injection properties of the anode.

The use of Ar plasma has no pronounced chemical effects on the ITO surface, and consequently offers merely a slight improvement to device performance through surface cleaning. On the other hand, SF_6 and CHF_3 plasma treatments of ITO greatly improve the injection of holes and the stability of OLEDs [259,260]. The major effect is attributed to the surface incorporation of fluorine.

4.4.2. Buffer layers between ITO and HTL

Besides surface treatments the other approach to enhance hole-injection is the insertion of a nanometer thick organic interlayer (such as CuPc) with its HOMO between the ITO Fermi level and the HOMO of the HTL. This creates a ''ladder-type'' energy structure, which has shown to improve hole-injection. One may also interpose an ultrathin conductive layer with its work function matching the HOMO of the HTL (such as Pt and C).

4.4.2.1. CuPc. Both device stability and efficiency can be dramatically enhanced by interposing a CuPc layer between an ITO anode and a HTL, while its effect on hole-injection strongly depends on processing conditions. Forsythe et al. [261] demonstrated that the hole-transport from the ITO anode to the NPB is injection limited and that the hole-injection efficiency is reduced progressively as the CuPc thickness is increased in the range of 0–30 nm. The increase in device efficiency induced by inserting a CuPc layer is correlated with a decrease in hole-injection efficiency, which leads to an improved balance between hole and electron currents arriving at the recombination zone. Hill and Kahn [262] studied the TPD/CuPc/ITO interfaces by UPS and *I–V* characteristics of a single layer hole-only device, and pointed out that a CuPc layer interposed between an ITO anode and a HTL may improve hole-injection if the CuPc/TPD barrier is smaller than the ITO/TPD barrier. Therefore, the work function of the ITO being used will determine whether the CuPc interlayer improves or degrades hole-injection. As the work function of ITO is known to depend strongly on the processing conditions, the effects of CuPc on hole-injection may vary considerably.

4.4.2.2. Platinum. Platinum has the largest work function of 5.7 eV among metals. A dramatic increase in the injected current was achieved by interposing a 0.5 nm thick Pt layer between ITO and TPD [263]. Surprisingly, the modification of the ITO with Pt layers did not affect the quantum efficiency, even though holes are presumably the dominant carriers in OLEDs. It was postulated that the enhancement of hole-injection from the anode led to a higher hole density at the TPD side of the interface, which resulted in a high electric field drop across the Alq_3 layer. This strong field enhanced electron injection and transport in Alq_3 and consequently restored the ratio of charge densities at the interface. Therefore, the modification of ITO with an ultrathin Pt layer resulted in a lowering of the operating voltage without deteriorating the device efficiency. It is not clear at present whether the work function of Pt is indeed the primary factor, because the presence of a dipole at the Pt/TPD interface may substantially alter the energy level offset.

4.4.2.3. Carbon. A 10 nm thick carbon layer was inserted between ITO and a HTL in an OLED by dc magnetron sputtering in an argon–nitrogen ambient [264]. The resistivity of the carbon films was in the range of $(4-3) \times 10^3\ \Omega$ cm, and the work function was around 5.2 eV. Similar to Pt, the threshold

voltage of the OLED decreased considerably with no differences in EL efficiency. The improvement was explained in terms of high ionization potentials and effectiveness in adhesion.

4.4.2.4. SiO_2 and Si_3N_4. SiO_2 and Si nitride as a hole-injecting buffer layer behave differently from Pt and C [34,265]. In the presence of the ultrathin buffer layer, the enhancement in luminance efficiency was observed and attributed to an improved balance of charged carriers due to blocking the injected holes and a homogeneous adhesion of the HTL to the anode. Correspondingly, the insertion of a buffer layer commonly results in an increase in drive voltages and a less beneficial effect on power efficiency.

4.4.3. Non-ITO anodes

Over the past few years, increasing activity has focused on improving charge injection efficiency at electrode/organic interfaces in OLEDs. As described before, a number of low-work function metals and their combinations with other atmospherically stable metals have been implemented as a cathode to offer improved quantum efficiencies and low operating voltages. In contrast, relatively few materials have been explored as alternatives to ITO as OLED anodes. ITO has the virtue of optical transparency, but it is not a well-controlled material. Several alternative materials have been recently examined as anodes, however all suffer from some unfavorable characteristics.

4.4.3.1. Fluorine-doped tin oxide. Both Ge-doped ITO and fluorine-doped tin oxide (FTO) have been used as an alternative to ITO for hole-injection in PLEDs [266,267]. There are several advantages to using FTO instead of ITO electrodes: (1) FTO is less expensive than ITO, (2) FTO is less sensitive to surface cleaning methods than ITO, and most importantly, (3) more light is obtained at a given voltage. One drawback with the FTO-based devices is the high leakage current on the order of 1 mA/cm^2.

4.4.3.2. Al-doped zinc oxide. Unlike ITO, zinc oxide is a non-toxic and inexpensive materials. It is an n-type semiconductor with a bandgap of approximately 3.3 eV at room temperature. Zinc oxide doped with group III elements shows stable electrical and optical properties. Al-doped zinc oxide (AZO) films have low resistivity of $(2-4) \times 10^{-4}\ \Omega\,cm$ and good transmission in the visible region, comparable to ITO films. Various thin film deposition techniques have been employed to grow AZO films, including chemical vapor deposition, magnetron sputtering, and pulsed laser deposition [268–270]. In the latter two cases, good quality films can be achieved at room temperature due to the high kinetic energy of atoms and ionized species in plasma. In general, when the AZO films are used as an anode contact for OLEDs, the device performance is similar to or worse than that with an ITO anode possibly due to its relatively low-work function.

4.4.3.3. Transparent conductive oxides (TCO). Cui et al. [271] reported initial observations on the implementation of four new highly transparent, high work function TCO materials as OLED anodes: $Ga_{0.12}In_{1.88}O_3$ (GIO), $Ga_{0.08}In_{1.28}Sn_{0.64}O_3$ (GITO), $Zn_{0.5}In_{1.5}O_3$ (ZIO), and $Zn_{0.46}In_{0.88}Sn_{0.66}O_3$ (ZITO) [271]. Besides exhibiting high electrical conductivities (10^{-3} to $3 \times 10^{-4}\ \Omega\,cm$) and broad, outstanding optical transparencies (>90%), the TCO films possess unusually high work functions (5.2–6.1 eV versus 4.5–4.7 eV for ITO). OLED devices fabricated with these materials as anodes exhibited luminance efficiency comparable or superior to ITO-based devices, however, the turn-on voltages were considerable higher than their competitor. It is of importance to determine the physical origin of their relatively poor injection properties before applications.

4.5. Carrier transport

Organic molecular materials have low mobility (10^{-8} to 10^{-2} $cm^2/(V\ s)$). Electron mobility in organic materials is generally orders of magnitude lower than hole mobility [272,273]. As a consequence, low-voltage operation and high power efficiency are strongly controlled by the electron current from the cathode to the emissive zone. This argument has been further proved by the measurement of internal electric field in an OLED, in which the field in a NPB layer is considerably smaller than that in the Alq_3 layer at forward bias voltages [274].

4.5.1. Limiting factors in electrical properties

The current that flows through a semiconductor can either be limited by the semiconductor bulk or by the contact. In the first case, the contact serves as an infinite reservoir of charge to satisfy the demands of the bulk, and the current is limited by intrinsic transport properties of the semiconductor. This is the SCLC for a trap-free material given by the Mott–Gurney law: $J_{SCLC} = (9/8)\varepsilon\varepsilon_0\mu V^2/L^3$, where $\varepsilon\varepsilon_0$ is the dielectric constant of the organic layer, μ the mobility, L its thickness, and V is the applied bias [275,276]. In other cases, however, the contact might not be able to supply the semiconductor with enough current to sustain a SCLC. The process of charge injection determines the current flow through the sample. A quantitative figure-of-merit for describing contact behavior is the injection efficiency, η, defined as the ratio between the current that is supplied by the contact (the current that flows under forward bias) to the SCLC. By definition, $\eta = 1$ for an Ohmic contact and, $\eta < 1$ for a current-limiting contact.

In general, the experiment consists of three steps: First, the mobility of a sample is measured by the TOF technique. Second, the space charge limited current is calculated for that sample. Third, the current is measured in an electron- or hole-only device, and the injection efficiency η is calculated. From the limited data reported in the literature, the cathode contact of Alq_3/LiF (0.1–0.2 nm)/Al [233] and the anode contact of ITO/Pt (0.5 nm)/TPD [263] and ITO/m-MTDATA [277] are Ohmic at high electric fields, while the cathode contact of Alq_3/MgAg [233] and the anode contact of ITO/TPD [60] and ITO/NPD [60] are injection limited.

The study of anode contacts is described here in detail as an illustration. Three different HTL materials (m-MTDATA, TPD, and NPD) were used to form three single-layer hole-only devices, respectively [60]. The single layer devices had a silver cathode for TPD and NPD and a gold cathode for m-MTDATA. The trap-free space charge limited (TFSCL) current was calculated based on a trap-free hole carrier drift mobility, which is 3×10^{-5} $cm^2/(V\ s)$ for m-MTDATA and 10^{-3} $cm^2/(V\ s)$ for TPD and NPD. The measured current density of m-MTDATA single-layer device is in good agreement with the theoretically predicted TFSCL current (Fig. 32). The current densities for TPD and NPD single-layer devices are similar to each other but are three orders of magnitude lower than the current density of the device with m-MTDATA, even though the hole mobilities in TPD and NPD are sufficiently higher than that in m-MTDATA. Moreover, they are four to five orders of magnitude lower than the calculated TFSCL current.

The results indicate that the m-MTDATA forms an Ohmic contact with ITO at high electric fields, in which the current through the device is limited only by the hole mobility of the m-MTDATA layer, the applied voltage, and the thickness of the organic layer. The Ohmic contact between the ITO and the m-MTDATA explains the good agreement between the measured and the theoretically predicted TFSCL current densities for the ITO/m-MTDATA/Au device. On the other hand, the measured current in the TPD and NPD devices is orders of magnitude lower than the calculated TFSCL current. From that it can be concluded that the ITO/TPD and ITO/NPD interfaces have to be the limiting factor for hole-injection in the devices.

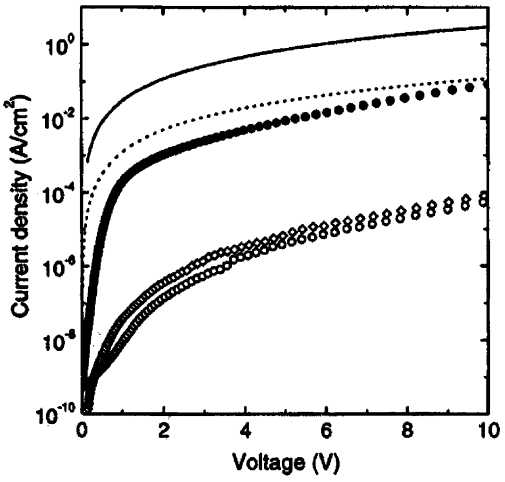

Fig. 32. *J–V* characteristics of single-layer hole-only devices for m-MTDATA (closed circles), TPD (open diamonds), and NPD (open circles). For comparison, the theoretically predicted TFSCL current for m-MTDATA (dotted line) and TPD (continuous line) are also displaced [60].

Theoretical derivation indicates that the rate of injection at a contact limited electrode is proportional to the charge mobility in the organic material [278]. An experiment was conducted by Shen et al. [279] to measure charge injection from ITO into a TPD-doped polycabonate (PC:TPD) and revealed that the current injected at the contact was indeed proportional to the hole mobility in the doped material when the hole mobility was varied from 10^{-6} to 10^{-3} $cm^2/(V\ s)$ by adjusting the concentration of TPD in the PC host [279].

4.5.2. Current–voltage characteristics

Typical Alq_3-based OLEDs show a power-law dependence of $I \sim V^{8-9}$ over a large current and voltage range, which is inconsistent with the theory of SCLC in insulating solids. Because of the large trap concentration and low mobility in organic semiconductors it has been proposed that the carrier transport in OLEDs is trap charge limited (TCL). Based on the assumption of an exponential trap energy distribution the current–voltage relationship has been shown to have the power-law dependence $I \sim V^{m+1}$, where $m = T_t/T \sim 6$–8 with T being the absolute temperature and T_t being the characteristic temperature of the trap distribution [280,281]. It was then considered that current in this regime was determined by the bulk properties of the solid rather than contact effects. Increasing bias resulted in an increase in injected charge, thereby filling the limited number of traps. The reduction in empty traps resulted in a rapid increase in the effective carrier mobility, and therefore a rapid, power-law increase in current.

Burrows and Forrest measured *I–V* characteristics under forward bias of a series of devices with 200 A of TPD and 400 A of Alq_3, Gaq_3 or Inq_3 (Fig. 33) [282]. The *I–V* characteristic for each material was described by $I \sim V^{m+1}$, as expected for bulk-limited conduction in the presence of traps at high current injection. Thus, they concluded that TCL conduction was a general property of Mq_3-based devices.

Hung et al. [226] measured the *I–V* characteristics of Alq_3-based devices with a cathode of Al, $Mg_{0.9}Ag_{0.1}$ and Al/LiF, and found that all *I–V* curves could be described by $I \sim V^{m+1}$ with $m = 7$, independent of the contact material (Fig. 34). The Al-contact device shows no noticeable deviation from the power-law, although Al has a much higher barrier than Mg with Alq_3 and thus the electron

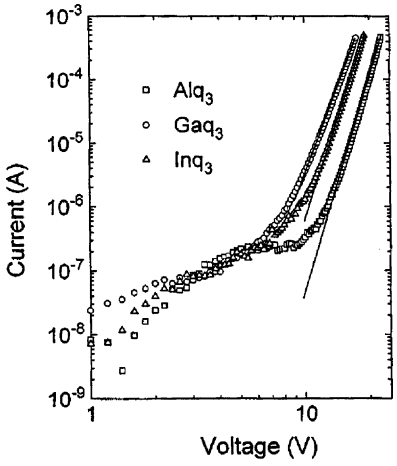

Fig. 33. Forward bias current–voltage characteristics of OLEDs with a 20 nm thick layer of TPD and a 40 nm thick layer of Mq_3, where M = Al, Ga, and In. Solid lines show fits to the TCL model [280].

current is expected to be injection limited. There is also a parallel shift in the *I–V* curves, indicating a different threshold voltage for the various electrodes. If the power-law dependence were indeed the characteristic for a trap-limited transport process in Alq_3 bulks, one would have to assume that the trap density in Alq_3 varies substantially with the electrode properties in order to account for the large separation of the *I–V* curves. However, this assumption is inconsistent with the picture that the high defect density is a consequence of structural disorder in Alq_3 rather than impurity incorporation due to metallization. The model of discrete traps may hold only at one circumstance where the metal ions diffuse in and introduce discrete trap levels in the Alq_3 layer [283].

Baldo and Forrest [284] re-examined the power-law dependence by using single-layer electron-only devices, and confirmed the results by Hung et al. It is thus concluded that injection processes at the metal/organic contact dominate the current–voltage characteristics. Moreover, when varying the

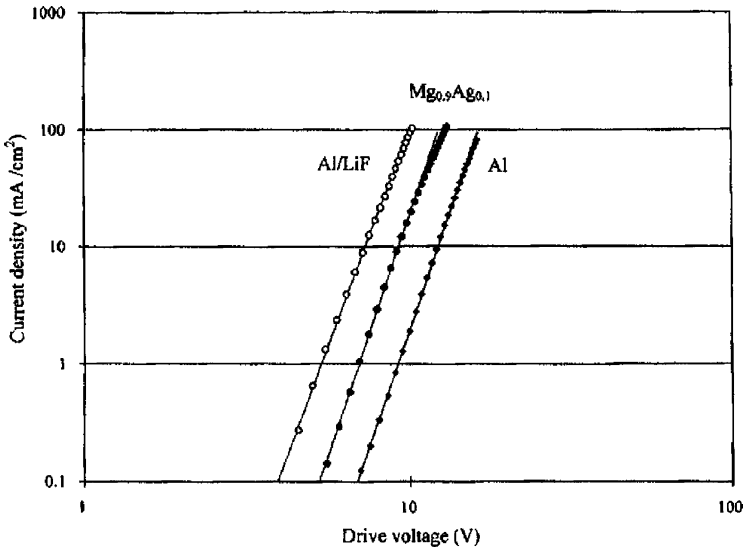

Fig. 34. Fits (solid lines) to the current–voltage characteristics of three OLEDs with a cathode of Al, MgAg and LiF/Al, respectively [226].

thickness of the Alq_3 layer a linear dependence of the voltage on the thickness of Alq_3 was found for all three cathodes at a given current density, demonstrating that injection processes overwhelm bulk space charge effects in these devices.

It is well known that strong interactions between the metals of Li, Mg and Al and the organic films of Alq_3 cause interfacial states adjacent to LiF/Al, MgAg and Al cathodes. Some randomness in the interface dipole orientation is likely given by cathode metal diffusion into the organic. Hence, a new model is proposed, in which the interface dipoles significantly broaden the energy distribution of Alq_3 transport states in the interfacial layer, resulting in a situation similar to trap limited transport at the metal/organic interface [285]. Charges from the metal are injected into a broad distribution of interfacial trap states, from which they then hop into a narrower distribution of transport states in Alq_3 bulk.

4.5.3. New electron-transport materials

Current glassy and amorphous organic molecular materials have low-electron mobility in the range of 10^{-6} $cm^2/(V\ s)$. Moreover, effective electron-transport molecules are usually more chemically sensitive to their environments; hence, very few useful materials with superior electron mobility have been developed.

Oxadiazole-containing organic materials generally possess good electron-transport properties, and a number of oxadiazole derivatives have been utilized as electron-transport materials in OLEDs [286–289]. The oxadiazole with naphthyl substituent (BND) was reported to possess high potential of electron-transport, and the electron mobility of 50 wt.% BND-doped polycarbonate (PC) was 2.2×10^{-5} $cm^2/(V\ s)$ at an electric field of 7.5×10^5 V/cm at room temperature.

Electron and hole mobilities in bipolar molecular composites of *N*,*N*′-bis(l,2-dimethyl-propyl)-1,4,5,8-naphthalenetetracarboxylic dimide (NTDI) and tri-*p*-tolylamine (TTA) have been studied [290]. Molecular glasses of NTDI have the electron mobility of $\sim 4 \times 10^{-5}$ $cm^2/(V\ s)$, while the electron mobility in bipolar composites prepared by co-sublimation is found to be enhanced by a factor of 4–6 compared to pure NTDI in the range of fields investigated.

Two soluble tris(phenyl)quinoxalines have been identified in the literature as the effective electron-transport materials, which are tris(phenyl)quinoxalines 1,3,5-tris[(3-phenyl-6-trifluoromethyl)quinoxaline-2-yl]benzene (TRQ 1) and 1,3,5-tris[{3-(4-*tert*-butylphenyl)-6-trifluoromethyl}-quinoxaline-2-yl]benzene (TRQ 2) [291]. The electron mobilities for both compounds approach 10^{-4} $cm^2/(V\ s)$ at electric fields of 10^6 V/cm at room temperature.

The electron mobility for 4,7-diphenyl-1,10-phenanthroline (bathophenanthroline, or BPhen) is in the range 3.9×10^{-4} $cm^2/(V\ s)$ (2×10^5 V/cm) to 5.2×10^{-4} $cm^2/(V\ s)$ (5.5×10^5 V/cm) with a weak dependence on the electric field, that is about two orders of magnitude more mobile than in Alq_3 [292]. In comparison with other electron-transport materials: oxadiazole derivatives, bipolar molecular composites and starburst phenylquinoxalines, BPhen has the highest electron mobility. Phenanthroline is a small, rigid and planar molecule with extended π-electrons and short hopping lengths that facilitate electron motion in BPhen.

Although the electron mobilities in those materials are one to two orders of magnitude greater than that in Alq_3, only a few experiments have been carried out to replace Alq_3 with the new materials in OLEDs. Moreover, limited data on the use of these materials for OLEDs indicate no significant beneficial effects on voltage reduction. The possible explanations are based on the importance of a perfect match of the energy levels between the new electron-transport materials and the materials used for the emissive layers and cathodes. Any electron-injection barriers introduced by these materials could lead to an increase in operating voltages. It can be best illustrated by the use of CuPc as an ETL in OLEDs.

CuPc was identified as an effective electron-transport material with its electron mobility substantially greater than that of Alq_3 and was successfully utilized to replace Alq_3 for electron-transport [293]. However, the CuPc layer forms an electron-injection barrier with the Alq_3 layer in the OLED with a configuration of ITO/NPB/Alq_3/CuPc/MgAg, resulting in increased electron–hole recombination in the non-emissive CuPc layer, and thus a substantial reduction in EL efficiency. Incorporation of an ultrathin bilayer LiF/Al at the Alq_3/CuPc interface was found to reduce the injection barrier at the interface and recover the overall device efficiency. As a result, the device with a doped Alq_3 emissive layer exhibited a luminance of 120 cd/m^2 at 3 V. CuPc has a high absorption coefficient at wavelengths longer than 550 nm, implying that this electron-transport material is not suitable for use in red emission. For the application of OLEDs to full-color flat panel displays it remains challenging to develop new electron-transport materials that have superior electron mobilities, wide bandgaps, and appropriate energy levels.

4.5.4. Doping

4.5.4.1. Doping in ETLs. One of the promising solutions to reduce bias voltages in OLEDs is the use of n-type doping in ETLs [294]. Bright OLEDs have been achieved by using a Li-doped organic layer as an ETL with a molecular ratio of Li/Alq_3 at unity. In OLEDs with a configuration of ITO/NPB/Alq_3/Li-doped Alq_3/Al, the current density increases dramatically with increasing the thickness of the doped Alq_3 layer when the total thickness of the Alq_3 layer is constant. It is of importance to note that this approach not only increases the conductivity of the doped Alq_3 layer but also reduces the barrier to electron injection at the Alq_3/Al interface. Similar n-type doping was applied to an OLED having a distyrylarylene derivative as an EML/ETL [295]. Ca, Li, Na, K or Cs was doped into the EML near the EML–Al interface. As the work function of the metal decreased, the driving voltage was correspondingly reduced.

Recently, Li-doped BPhen was used as an electron-transport layer for the construction of a pin OLED. The conductivity of Li-doped BPhen at room temperature was approximately 10^{-4} S/cm, orders of magnitude higher than that of undoped films ($<10^{-9}$ S/cm), thus leading to substantial voltage reduction. The operating voltage was 2.55 V for 100 cd/m^2 and 3 V for 1400 cd/m^2 [296].

The Li diffusion and the effects of Li incorporation in various organic media have been studied [297]. A thermally evaporated surface layer of metallic Li was found to diffuse through and subsequently dope the underlying organic thin films. A diffusion length of 30 nm for Alq_3 and 70 nm for BCP was inferred from analyses of the current–voltage and secondary ion mass spectrometry data. The conductivity of the Li-doped organic films was $\sim 3 \times 10^{-5}$ S/cm. Photoemission spectroscopy suggests that Li lowers the barrier to injection at the organic/cathode interface, introduces gap states in the bulk of the organic semiconductor, and dopes the bulk to facilitate efficient charge transport. The Fermi level of the organic was found to move towards the LUMO, indicating an increase in the carrier density in the bulk, and the carrier density of the doped film was approximately 10^{18} cm^{-3}, as inferred from conductivity measurements.

Although the use of n-type doping is able to increase the conductivity of doped organic materials and thus achieve voltage reduction in OLEDs, the optimum dopant concentration and the diffusion length of Li atoms vary substantially with the materials of interest. In addition, the formation of quenching centers in the emissive layer by rapid Li diffusion is a prime issue of concern in the development OLEDs with low drive voltages and high operational stability by Li doping.

4.5.4.2. Doping in HTLs. The use of p-type doping into hole-transport materials has also been investigated, and the results showed that the doping considerably increased the bulk conductivity of

the HTLs and led to a thinner space charge layer which could enable efficient tunnel injection of holes from the ITO to the doped HTL [298,299]. A hole-transport material of vanadyl-phthalocyanine (VOPc) was doped with tetrafluoro-tetracyano-quinodimethane (F_4-TCNQ) by co-sublimation [37]. The conductivity increased by many orders of magnitude, and electrical measurements showed a smooth shift of the Fermi level towards the valence states with increasing doping. Doping was found to strikingly improve the properties of OLEDs.

5. Quantum efficiency

In OLEDs, the following processes take place successively: the injection of the oppositely charged carriers, the formation of excitons, and light emitted during recombination of the electron and hole (Fig. 35). Quantum efficiency $\eta(q)$ is defined as the ratio of the number of emitted light quanta per unit area per unit time to the number of carriers flowing across unit area per unit time. In Fig. 35 the internal quantum efficiency is described as $\eta_{\text{int}} = \gamma\eta_1\eta_2$, and the external quantum efficiency is shown as $\eta_{\text{ext}} = \gamma\eta_1\eta_2\eta_3$.

The variable γ is the number of electron–hole pairs (excitons) formed per unit volume per unit time divided by the carriers flowing across unit area. The number of excitons formed is determined by the number of minority carriers. It is physically quite obvious that γ can never be larger than 0.5. In an alternative way, quantum efficiency is defined as the ratio of the number of emitted light quanta to the number of electrons, and then γ is approximately equal to 1.

The quantity η_1 represents the luminance efficiency of the excitons. Spin-symmetric excitons with a total spin of $S = 1$ have a multiplicity of three and are known as triplets. Spin-anti-symmetric excitons ($S = 0$) have a multiplicity of one and are known as singlets [300]. During electrical excitation approximately one singlet exciton is created for every three triplet excitons, but only relaxations of singlet excitons conserve spin and generate fluorescence because the ground state is typically also spin-anti-symmetric. Therefore, one can expect to lose 75% of the electron–hole pairs to triplet excitons, which do not decay radiatively with high efficiency.

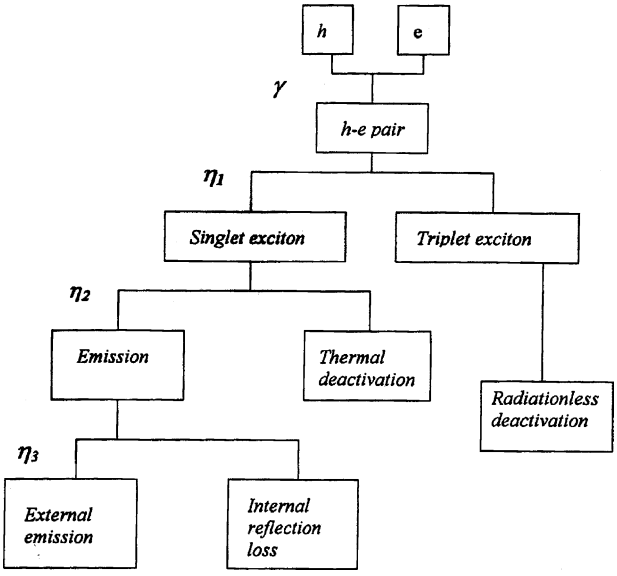

Fig. 35. Schematic diagram showing EL process.

The quantity η_2 is defined as the ratio of radiative transition from the singlet excitons. In the absence of competing radiationless transitions, its value is approximately 1.

The variable η_3 represents the fraction of the light emitted at the surface relative to the light produced in the bulk. It is determined by the device structure and the refractive indices (n) of the composed layers since in thin film light-trapping caused by total reflection is inevitable. This factor can be estimated by Fresnel loss ($1/2n^2$) to be about 20% as most indices of organic materials are about $n \sim 1.6$. By adding all factors together, the maximum external quantum efficiency is estimated to be 2–3%. The efficiency is primarily limited by coupling losses and restrictions imposed by spin conservation.

5.1. Phosphorescent OLEDs

In compounds consisting of lighter elements, such as conventional organic materials, the decay of a triplet state is generally forbidden by the conservation of spin symmetry. It becomes weakly allowed by introducing heavier elements due to spin-orbit coupling. In such cases, the decay of the triplet state may still be very slow, but phosphorescence is generated.

The solution to the utilization of phosphorescent materials in OLEDs is found by doping the phosphorescent material into a charge transport host material. Baldo et al. have described the major differences between fluorescence and phosphorescence in terms of materials and devices [301]. Emission occurs by exciton formation in the host and energy transfer to the luminescent guest through triplet–triplet transfer (Dexter energy transfer). This is a short-range process where excitons diffuse from donor (host) to acceptor (dye) sites via intermolecular electron exchange at a rate proportional to the orbital overlap of the donor and acceptor molecules. It differs from the mechanism described for singlet–singlet transfer (Forster energy transfer), which is a long range (~40 A), dipole–dipole coupling of donor and acceptor. The doping concentrations required to maximize quantum efficiency are extremely high compared to devices doped with fluorescent dyes and excited by long-range Forster transfer. High efficiencies are obtained by transition from the host singlet and triplet states to the phosphor triplet states via energy transfer and intersystem crossing and by direct trapping of charge on the phosphor dyes.

High efficiency has been demonstrated in OLEDs using the phosphorescent dyes. The OLED consists of a HTL, a light-emitting layer doped with phosphorescent dyes, a barrier layer to exciton diffusion, and an ETL (Fig. 36). Owing to long lifetimes, the diffusion lengths of triplets in organic materials are substantially longer than that of singlets. To optimize efficiency, OLEDs are then modified to trap triplets within the luminescent layer, thereby increasing the probability for energy transfer from the host to the phosphor. A material suitable for this purpose is a hole blocking layer (HBL), which has a large ionization potential. Furthermore, because of its wide bandgap, it should act as a barrier to exciton diffusion. The use of a barrier layer to exciton diffusion is particularly important when the orbital overlap of the donor and acceptor molecules is weak.

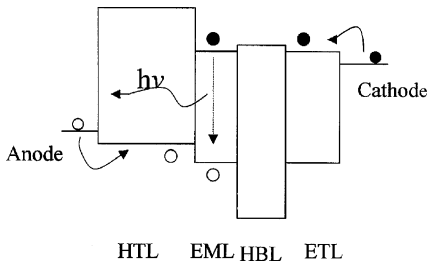

Fig. 36. Schematic energy diagram of an electrophosphorescent OLED.

One notable difference between OLEDs based on fluorescence and phosphorescence is that phosphorescent efficiency decreases rapidly at high current densities. Long phosphorescent lifetimes cause saturation of emissive sites, and triplet–triplet annihilation also results in significant efficiency losses. Triplet–triplet annihilation and saturation can be minimized if the phosphorescent lifetime is short by increasing spin state mixing.

The description in the following paragraphs is mainly focused on some physical insights, as both molecular structures of some phosphorescent materials and device performance of phosphorescent OLEDs have been described in detail in Section 3.

5.1.1. Red emission

Both red-emitting fluorescent and phosphorescent dopants have shown promise for use in OLEDs. While fluorescent dyes, including DCJT have been investigated, their maximum external quantum efficiencies are limited to 1–2%. The red phosphorescent europium complexes have also been studied [302–304]. Although the complexes show very strong red Eu^{3+} ion emission (with an internal quantum efficiency $\eta_{int} > 80\%$), the high triplet energy of the ligands causes backward energy transfer to the host molecule, leading to $\eta_{ext} < 1.4\%$.

PtOEP is a red-emitting phosphorescent dye. The Alq_3-based devices with 6% PtOEP generate red emission with peak external and internal quantum efficiencies of 4 and 23%, respectively [167]. The efficiency can be optimized by the selection of the host materials. Internal quantum efficiencies of up to 32% at low brightness are obtained from PtOEP doped in a blue host of 4,4′-*N*,*N*′-dicarbazole-biphenyl (CBP) [168], which is higher than the value of 25% if only singlet excitons are transferred to PtOEP molecules. Due to weak overlap between excitonic states in PtOEP and CBP, luminance efficiency is increased. Under such a circumstance, there is a much lower probability for exciplex formation and reverse energy transfer, both of which could lead to non-radiative quenching of PtOEP emission. However, energy transfer between the species is also poor. In compensation, a thin layer of 2,9-dimethyl-4,7-diphenyl-l,10-phenanthroline (bathocuproine, or BCP) is used as a barrier to exciton diffusion in CBP, improving the energy transfer to PtOEP. By blocking the triplets from leaving the luminescent layer, it increases their residence time in this region, thereby increasing the probability for energy transfer from CBP to the phosphorescent dye. The benefits of the BCP barrier are most noticeable for the thinner (25 nm) luminescent layers, where energy collection by PtOEP is particularly inefficient.

High-efficiency red electrophosphorescent OLEDs have been demonstrated employing bis(2-(2′-benzo[4,5-*a*]thienyl)pyridinato-N,C3′)iridium(acetylacetonate) ($Btp_2Ir(acac)$) as a red phosphor [305]. The short phosphorescence lifetime ($\sim$4 μs) of $Btp_2Ir(acac)$ leads to a significant improvement in η_{ext} at high currents as compared to the red phosphor PtOEP with a lifetime of $\sim$50 μs.

5.1.2. Green emission

A green phosphorescent OLED was constructed by employing the green electrophosphorescent material, *fac*-tris(2-phenylpyridine)iridium ($Ir(ppy)_3$) doped into a CBP host [172,301]. The lifetime of $Ir(ppy)_3$ in CBP is short and indicative of strong spin-orbit coupling, and there is strong intersystem crossing from the singlet to the triplet state in $Ir(ppy)_3$. This efficient transfer of both singlet and triplet excited states in the host to $Ir(ppy)_3$ leads to a high internal efficiency.

A maximum external quantum efficiency η_{ext} of 15.4% and power efficiency of 40 lm/W are obtained from a OLED having an emitter of 7% $Ir(ppy)_3$-doped into 3-phenyl-4-(1′-naphthyl)-5-phenyl-l,2,4-triazole (TAZ) and using an Al–Li cathode [306]. The device exhibits a gradual decrease in quantum efficiency with increasing current, however, a high luminance of $\sim$4000 cd/m^2

with $\eta_{ext} = 10.0\%$ was maintained even at $J = 10$ mA/cm^2. The maximum value of $\eta_{ext} = 15.4\%$ corresponds to $\eta_{int} = 80\%$ and is almost double compared with that reported for the devices of Ir(ppy)$_3$ in CBP. The room temperature transient phosphorescent lifetime of 7% Ir(ppy)$_3$ in TAZ is $\tau = 650$ ns, compared with $\tau = 380$ ns in 7% Ir(ppy)$_3$:CBP. Since the phosphorescence efficiency is approximately proportional to the lifetime, the longer lifetime in TAZ is consistent with the higher EL efficiencies of these devices.

Since the green phosphorescent OLEDs show a strong dependence on the concentration of Ir(ppy)$_3$ in hosts, a new tris-*ortho*-cyclometalated compound of iridium based on the pinene-substituted 2-phenylpyridine has been synthesized [174]. This novel material exhibits very strong green phosphorescence emission with a PL quantum yield of 0.71 in solution and a relative short triplet lifetime of 0.33 μs in solid. Self-quenching is significantly reduced for this iridium compound in solution even at very high concentrations because the sterically hindered pinene spacer in the phosphor molecule leads to minimum bimolecular interaction. Bright green emission was observed from EL devices based on this iridium compound, and the external quantum efficiency increased with increasing Ir(mppy)3 concentration (up to 26% Ir(mppy)$_3$ in CBP), thus further confirming that the aggregation quenching is almost negligible in the phosphorescent devices.

5.1.3. Blue emission

In phosphorescent OLEDs, high efficiencies were obtained by energy transfer from both the host singlet and triplet states to the phosphor triplet and by direct trapping of charge on the phosphor. These transfers entail a resonant, exothermic process. As the triplet energy of the phosphor increases in blue, it becomes less likely to find an appropriate host with a suitably high-energy triplet state. One approach is to employ the phosphorescent material as an undoped film, with an attendant loss in efficiency. Furthermore, this material layer may not have appropriate energy-level alignments with other materials used in an OLED structure, hence resulting in a further reduction in efficiency. This problem has been partially solved by utilizing the endothermic energy transfer from a near-resonant excited state of the host to the higher triplet energy of the phosphor, when the energy required in the transfer is not significantly greater than the thermal energy.

Blue electrophosphorescence using energy transfer from a conductive organic host to the iridium complex: iridium(III)-bis(4,6-di-fluorophenyl-pyridinato-*N*,C$^{2'}$) picolinate (Firpic) is demonstrated [307]. For the OLED structure of ITO/CuPc (10 nm)/α-NPD(30 nm)/6% Flrpic-doped CBP (30 nm)/BAlq$_3$ (30 nm)/LiF (1 nm)/Al (100 nm), the EL spectrum has a maximum at 475 nm and additional subpeaks at 495 and 540 nm, yielding CIE coordinates of $x = 0.16$, $y = 0.29$. A maximum external quantum EL efficiency (η_{ext}) of 5.7% and a luminous power efficiency (η_p) of 6.3 lm/W are achieved at 0.1 mA/cm^2, representing a significant improvement of the efficiencies compared with the blue fluorescent emitters reported to date. For comparison the data taken on those reported OLEDs are summarized in Table 2.

5.1.4. Energy transfer from triplets to singlets

It is highly desirable to find a process whereby triplets formed after excitation are not wasted, but are instead transferred to singlet excited states of a fluorescent dye. One approach is to dope both the phosphorescent material and the fluorescent acceptor into a conductive organic host, where the phosphor is acting as a sensitizer for energy transfer from the host to the fluorescent acceptor.

Baldo et al. [308] used CBP as the host and exciton donor, the green phosphor Ir(ppy)$_3$ as the sensitizer, and the red fluorescent dye DCM as the acceptor. However, a mixture may possess increased losses from Dexter transfer from the sensitizer to the triplet state of the fluorescent dye. To reduce this loss, the red fluorescent dopant and the phosphorescent sensitizer were separately doped

Table 2
Performance of various electrophosphorescent OLEDs

Dopant	Host	CIE	τ (μs)	$(\eta_{ext})_{max}$ (%)[a]	$(\eta_p)_{max}$ (lm/W)	η_{ext} (%)	η_p (lm/W)	I or L at η_{ext} and η_p[b]
PtOEP	Alq_3		55	4		0.7		100 cd/m^2
PtOEP	CBP		100	5.6		2.2		100 cd/m^2
$Btp_2Ir(acac)$	CBP	0.68, 0.32	6.5	7	4.6	4.4	1.3	10 mA/cm^2
$Ir(ppy)_3$	CBP	0.27, 0.63	0.38	8	31	7.5	19	100 cd/m^2
$Ir(ppy)_3$	TAZ		0.65	15.4	40	10	9	10 mA/cm^2
$Ir(mppy)_3$	CBP		0.33			3		60 mA/cm^2
Flrpic	CBP	0.16, 0.29		5.7	6.3	4.5	3	10 mA/cm^2

[a] The values are acquired at a low current density ranging from 0.002 to 0.1 mA/cm^2.
[b] I (current density) and L (luminance).

in alternating host layers. The peak efficiency of the DCM emission in the device containing the phosphorescent sensitizer was 3.3%. An ideal system for energy transfer from triplets to singlets may incorporate a sterically hindered fluorescent dye or phosphorescent sensitizer. Adding spacer groups could decrease the probability of Dexter transfer to the dye while minimally affecting its participation in Forster transfer or its luminescence efficiency.

5.1.5. Operational stability

Burrows et al. [309] investigate the continuous operating lifetime of OLEDs using the phosphorescent dopant PtOEP as the light-emitting molecule. The OLEDs lose ~25% of their luminance in the first 50 h of operation, followed by extremely slow degradation. The device lifetime of CBP-based phosphorescent OLEDs projected to 50% initial brightness is $>10^7$ h at a mean current density of 10 mA/cm^2 under 50% duty cycle pulsed operation. However, the results reported in the literature are somewhat inconsistent. For instance, recent preliminary data using the green phosphor $Ir(ppy)_3$ indicate a decay to half initial luminance of less than 1000 h at 100 cd/m^2 although it was postulated that the instability of the hole blocking BCP material may have an adverse effect on operational stability [310].

5.2. Optical coupling

A considerable portion of the light originating from emissive centers buried in a solid film never escapes due to internal reflection at the air–film interface and is scattered as edge emission or dissipated within the solid film. This is one of the major reasons why the luminous power efficiency of OLEDs remains relatively low. Although several approaches to increase the extraction efficiency have been reported, none of them is applicable to OLED displays.

5.2.1. General consideration

The typical OLED consists of a multi-layer sandwich of a planar glass substrate ($t_{sub} \sim 1$ mm, $n_{sub} = 1.51$), a layer of ITO ($t_{ITO} \sim 100$ nm, $n_{ITO} \sim 1.9$), a organic medium ($t_{org} \sim 0.1$ nm, $n_{org} = 1.6$–1.8), and a reflecting cathode, where t refers to the layer thickness and n refers to the index of refraction. The coupling problem can be easily analyzed provided that one can ignore both the microcavity effect and diffuse scattering at interfaces. If all surfaces are planar, light emitted from the backside of the substrate will originate only from light emitted at angles less than the organic-air critical angle, θ_1, given by $\sin^{-1}(n_{air}/n_{org})$ (ray I in Fig. 37). Light emitted at angles larger than θ_1 but smaller than the organic-substrate critical angle, θ_2, given by $\sin^{-1}(n_{sub}/n_{org})$ is trapped in

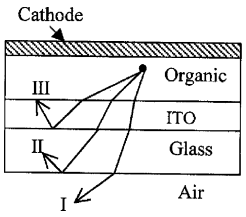

Fig. 37. Ray diagrams in planar OLEDs demonstrating losses by light-trapping in the substrate (ray II) and in the organic/anode layers (ray III). Only light emitted at sufficiently small angles will escape (ray I) [311].

the substrate (ray II in Fig. 37). Light emitted at angles larger than θ_2 is trapped in the organic and ITO layers collectively (ray III in Fig. 37), and will likely be quickly absorbed by the ITO or at the cathode [311]. It can be determined that the fraction of light escaping from the substrate (coupling efficiency), the fraction of light trapped in the substrate, and the fraction of light trapped in the organic/ITO layers are 18.9, 34.2 and 46.9%, respectively, for glass substrate and $n_{org} = 1.7$.

A model based on a quantum mechanical microcavity theory has been established to compute the distribution of light emission among the three modes, and to examine the effects of the ITO thickness and the refraction index of the substrate on this distribution [312]. Finally, the modeling results are correlated with experimental measurements determined both by the far-field emission pattern and the edge emission of light trapped in the glass substrate. The coupling efficiency is found to range from 24 to 52%, which is much larger than the 18.9% expected from classical ray optics. The main difference between the classical and QM models arises from the relative suppression of modes at large angles from the normal by the microcavity effect.

5.2.2. *Reduction in internal optical loss*

5.2.2.1. Microcavity. The use of microcavities to alter the EL characteristics of organic materials has been studied by several groups [313–317]. Jordan et al. [318] proposed the use of an optical microcavity to spatially and spectrally redistribute the EL emission of an OLED. The device employed an optical microcavity, which was formed by the highly reflecting back Al electrode and the quarter wave dielectric stack output mirror. By tuning the cavity resonance to wavelengths near the peak (non-cavity) EL wavelength, the emission of the device could be spatially redistributed to increase the amount of light emitted into this escape cone, and thus, increase the amount of light collected outside the device. The results indicated that for Alq_3 emission the 560 nm cavity was the optimum cavity location for net efficiency enhancement $\sim$2 and possessed no noticeable color variation.

5.2.2.2. Shaped substrates. For OLEDs, most internal generated light is trapped within the device, and the external coupling efficiency is only $\sim$18%. The coupling efficiency has been improved by a factor of 2 by etching grooves in the glass around the OLED to redirect light trapped in the substrate and organic/ITO layers [319]. This method does not lend itself well to the fabrication of device arrays, however, where metal lines and/or circuitry for passive or active-matrix drivers would have to cross the deep grooves.

A solution to the light-trapping problem, which preserves a planar surface for device processing, is to pattern the backside of the glass substrate in the shape of a sphere with the emitting area at its center. For spherical shapes subtending a large solid angle of emitted rays, light previously trapped in the substrate would be emitted. To capture the light waveguided in the organic/ITO layers, the use of a substrate with a high index of refraction is required. When OLEDs were made on polycarbonate

substrates ($n = 1.59$) and a lens made from molded epoxy ($n = 1.61$) was applied to the PC substrate, the total emitted intensity was increased by a factor of 3 [312].

5.2.2.3. Silica microspheres. Periodic dielectric structures, consisting of hexagonally close-packed arrays of silica microspheres were incorporated into OLEDs [320]. The arrays acted as a two-dimensional diffraction lattice, which behaved as a light scattering medium for the light propagated in waveguiding modes within the device. Monolayers of the ordered array of silica spheres (diameter of 550 nm) were placed on both sides of the stripe of the ITO electrode or coated on the front side of the glass. The results show that waveguided light components can be taken out from the inside of a device by using scattering due to the ordered array of silica spheres. This method is not applicable to OLED displays, as the emission color strongly depends on both scattering positions and observation angles.

5.2.2.4. Silica aerogel. A thick hydrophobic silica aerogel [321] layer with a refractive index of less than 1.03 was formed on a glass substrate, and a 50 nm thick SiO_2 buffer layer was deposited on top of this layer, then a 100 nm thick ITO layer was formed by sputtering [322]. The external quantum efficiency of an OLED with a 10 μm thick aerogel spacer layer was 1.39%, while the reference OLED on glass was 0.765%, yielding an enhancement factor of 1.8. The physical origin of this enhancement is not clear at present.

6. Reliability

Commercialization of the OLEDs depends on many factors such as efficiency, color, and most importantly stability. There have been extensive research efforts aimed at understanding the degradation mechanisms of small molecule-based OLEDs. The majority of these reliability studies concerned OLEDs employing the common electron-transport material, Alq_3. The operational instability is a long-term ''intrinsic'' decay in EL intensity leading to a uniform loss of efficiency over the device emitting area. The storage instability occurs through formation and growth of non-emissive regions or ''dark spots.''

6.1. Operational stability

Fig. 38 shows the variation of luminance and operating voltage with time at constant current operation. Two noteworthy features are: (1) the occurrence of two distinctly separate time scales in the luminance decay, with an early rapid decay, followed by a slower period and (2) the gradual rise in drive voltage required to maintain a constant current. Although the Kodak group has announced a lifetime of more than 50,000 h at 100 cd/m^2, the average lifetimes of an OLED in many research laboratories are considerably lower. Several causes for the degradation of OLEDs have been suggested, still more work is needed to understand and optimize the operational stability.

6.1.1. Anode contacts

Numerous data reported in the literature indicate the close relation between the operational stability and anode contacts. Adachi et al. [323] have examined a series of hole-transport materials and reported that the durability of their OLEDs was well correlated with the IP of the hole-transport materials. The stability was inversely related to the energy barrier of the hole-injection contact, and no relationships of melting point and glass transition temperature of the hole-transport materials with durability of the OLEDs were observed. It was postulated that with a large energy barrier, large Joule heat was produced at the interface, and consequently caused the local aggregation of molecules.

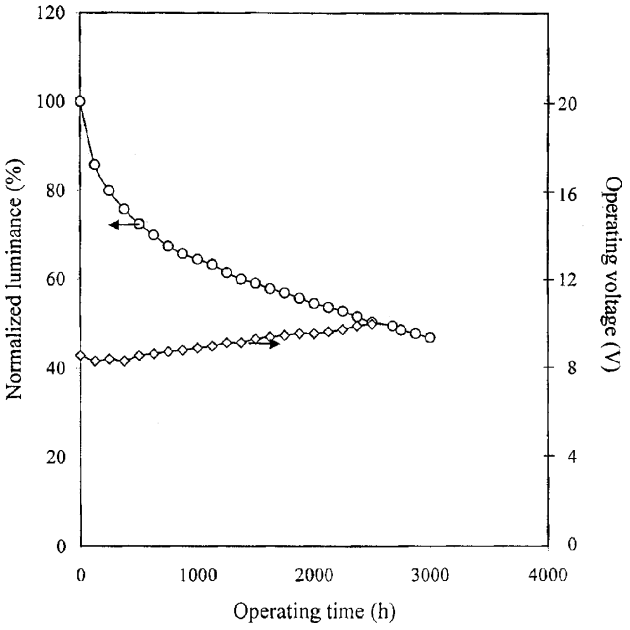

Fig. 38. Plots of luminance decay and voltage rise as a function of operating time at a constant current of 20 mA/cm^2.

The improvement of an ITO anode contact via oxygen plasma treatments has been well recognized. Enhanced hole-injection dramatically improves the performance of OLEDs, including voltage reduction, efficiency enhancement, and improved reliability [256,324]. The lifetime is enhanced by orders of magnitude as compared to the device having an untreated anode, and the rate of the voltage increase is substantially reduced. However, device performance strongly relies on processing conditions, such as O_2 partial pressure, plasma power density, and exposure time.

Another approach to anode modification is the use of a hole-injecting layer overlying the ITO anode. VanSlyke et al. [30] reported an OLED with a half-lifetime of about 4000 h at 20 mA/cm^2 by interposing a 15 nm thick CuPc layer between an ITO anode and a HTL of NPB. The improvement was largely attributed to using a low-barrier ITO/CuPc-injecting contact and enhancing adhesion of organic films to ITO [325].

The insertion of a CuPc layer commonly results in an increase in the drive voltage because of a hole-injection barrier at the CuPc–NPB interface. Plasma polymerization of CHF_3 at low frequencies was utilized for anode modification in OLEDs [326]. The polymerized fluorocarbon films have a high IP and are somewhat conductive. The devices with a polymer-coated ITO anode exhibited enhanced hole-injection and superior operational stability. The operational stability of the device with a 6 nm thick polymer layer at 20 mA/cm^2 was represented by a half-lifetime of 7000 h and a slow increase in operating voltages at a rate of 0.1 mV/h (Fig. 39). It is of interest to note that the use of a polymer layer on ITO can substantially reduce the initial luminance drop. The drop in the first 150 h was 1% and 15% measured on the device with a fluorocarbon coated ITO anode and a control device with an O_2 plasma-treated anode, respectively.

6.1.2. Excited state reactions

Excited state formation is intrinsic to the operation of OLEDs. Irreversible chemistry of the excited states can remove emissive species from the device. Even worse, these reaction products may form quench centers for excitons formed on nearby unaffected sites. So the selection and purification

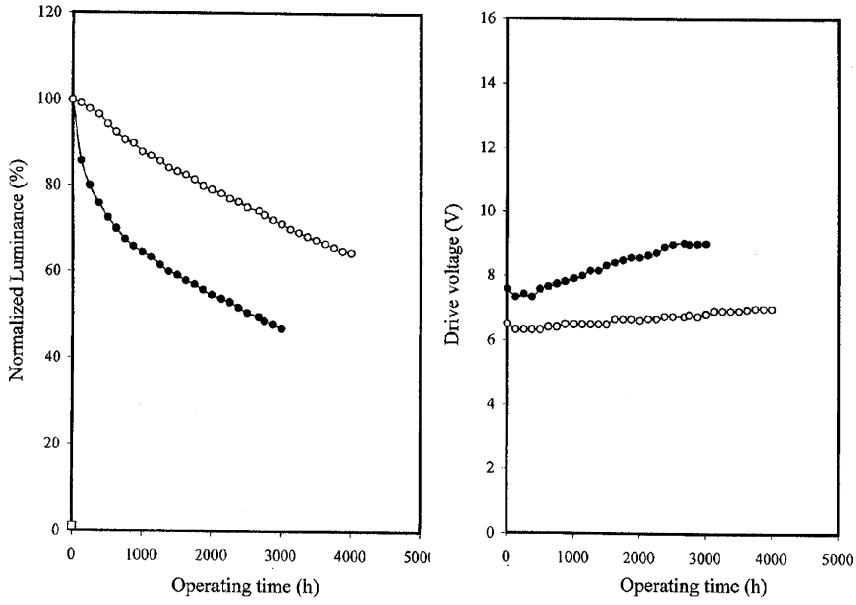

Fig. 39. Operational stability of an OLED with a fluorocarbon coated ITO anode (open circles) and a control device with an O_2 plasma-treated anode (closed circles).

of materials are an important factor in the rate of emitter degradation, and the operational stability of OLEDs can be substantially improved by introducing a stable dopant.

Rubrene is a commonly used dopant to improve device durability [327]. Doping of both the HTL and EML generated superior reliability, in which 85% of the initial luminance was successfully maintained even after 1000 h of continuous operation at 10 mA/cm^2 [328]. One simple explanation is that the excited states of rubrene molecules are more stable than that of hosts, and the suppression of the excited states of hosts by energy transfer contributes to the stability enhancement. Rubrene has also been used as a stabilizer and sensitizer to enhance energy transfer from Alq_3 to DCJTB. As a consequence, the device with an Alq_3 emitter doped with 2% DCJTB and 5% rubrene showed a half-lifetime of 3500 h at 20 mA/cm^2, significantly better than a device with a 2% DCJTB-doped Alq emitter [127].

Remarkable improvement in stability has been demonstrated in an OLED using a doped emitter consisting of Alq_3 as the host and DMQA as the emissive dopant [108]. A luminance half-life on the order of about 7500 h has been achieved in the DMQA-doped device at a high luminance of 1400 cd/m^2, that represents an increase by a factor of 2 as compared to an undoped OLED at the same current density. However, doping an OLED with unsubstituted QA yields a half-life of about 400 h. Both molecules are planar and the major structural difference lies in the substitution at the nitrogen atoms. The results clearly demonstrate that the operational stability of a doped OLED is dominated by the stability of dopants when sufficient energy transfer takes place.

6.1.3. Crystallization

Since organic thin films prepared by vapor evaporation are glassy and amorphous, crystallization is considered as one of the dominant degradation mechanisms. In particular, most organic materials commonly used in an OLED, especially those used for the HTL, have relatively low glass transition temperatures (T_g). Because of this, many methods have been employed to prevent or minimize the crystallization of the organic layers. The introduction of bulky molecules

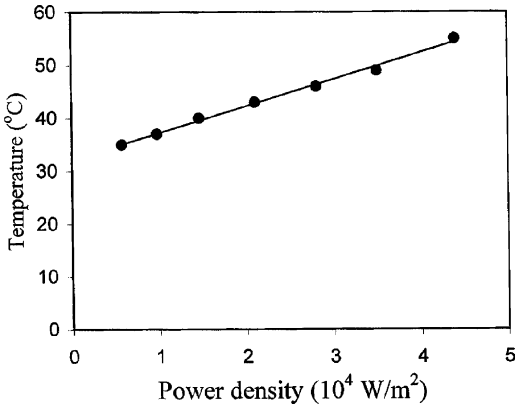

Fig. 40. Temperature rise owing to self-heating [329].

resistant to crystallization offers one solution to this problem. Molecular dopants were also proven to suppress crystallization, along with other benefits, such as improved emission efficiency and color tuning.

6.1.3.1. Self-heating in operation. Two critical issues for applications are the thermal stability and operational stability of OLEDs. It is of interest to study self-heating due to the power dissipation of the devices themselves. Real-time temperature measurements on OLEDs were conducted by using an infrared thermal imaging and analysis system. With an active area of approximately 0.1 cm^2, the surface temperature of an OLED was continuously monitored [329]. From observation, the temperature rise due to the Joule heating effect inside the device was significant under a high forward bias condition (Fig. 40). In a standard stability test (20 mA/cm^2 at 7.5 V), one can expect the temperature rise of about 7–8 °C for a power density of 1.5×10^4 W/m^2, which is qualitatively in agreement with that reported by Sturm et al. [330]. The results indicate that crystallization caused by self-heating may not play an important role in luminance decay at room temperature, unless other factors such as moisture may speed up the process.

6.1.3.2. Thermal stability. With an OLED having a TPD hole-transport layer, light output was gradually decreased with increasing temperature and dramatically dropped at 70 °C, which corresponds well to the glass transition temperature (60 °C). When using various hole-transport materials, a linear relationship was found between the T_g and the critical temperature [331]. This undoubtedly indicates that the thermal stability of the OLEDs with an Alq_3 emitting layer is dominated by the crystallization of the hole-transporting layer.

Alq_3 has risen to a prominent position in the development of robust OLEDs due to its relative stability with a high T_g of 174 °C. Annealing Alq_3 films at 175 °C resulted in a decrease of PL intensity. This was also accompanied by a slight red shift of the emission peak [332]. The observations were attributed to the formation of aggregates or crystals, which promoted formation of excimers or ground state complexes. The observed luminance decay of Alq_3 devices can be slowed with molecular doping. However, humidity may induce crystallization of Alq_3 at much lower temperatures and leads to OLED failure. This phenomenon is largely responsible for the rapid failure of OLEDs in humid atmospheres [333].

The thermal evolution of OLEDs has been measured by using X-ray specular reflectivity [334]. As-grown Alq_3/TPD heterostructures had molecular flat interfaces. Thermally induced failure of

these structures was found to be related to the large thermal expansion of the TPD layer associated with its low glass transition temperature, thus suggesting a strain-driven failure mechanism instead of a phase change mechanism.

One of the recent interesting experiments was the fabrication of an OLED having a crystalline HTL prepared at 120 °C, which showed considerable increase in luminance efficiency [335]. In such a device the HTL is already in the crystalline form before depositing an emissive layer, so that the high strain and surface roughness commonly observed in crystallization may not impose a significant impact on device performance [336]. Therefore, the role of crystallization in device degradation at elevated temperatures could not been simply ruled out by this experiment.

6.1.4. Quenching by Alq_3 cations

One of the most striking observations in device degradation was reported by the Xerox group, who found that the operation stability could be significantly improved by using a light-emitting layer of mixed Alq_3 and NPB [71,337]. Compared to a conventional bilayer device, the new device structure led to ~50% higher efficiency and an order of magnitude increase in the operational lifetime. The results imply that injection of holes in Alq_3 is the main factor responsible for device degradation.

The transport and recombination processes of charge carriers in the mixed device are pronouncedly different from that in the conventional bilayer device. In the mixed structure, the molecular orbitals of both NPB and Alq_3 remain unchanged because of the weak van der Waals coupling between molecules. The electrons and holes hop through the LUMO bands of Alq_3 and the HOMO bands of NPB, respectively, until they recombine with each other. Consequently, the formation of Alq_3 cations by injection of holes into Alq_3 is most unlikely.

The results have been further verified by analyses of a device with a configuration of ITO/NPB/Alq_3 (5 nm)/NPB/MgAg [338]. Because of a high-electron injection barrier at the NPB/MgAg interface holes are the predominant charge carriers through the 5 nm thick Alq_3 layer. These devices showed a significant decrease in photoluminescence efficiency after prolonged current flow. However, the studies on Alq_3 layers through which only electrons were transported did not show a decrease in photoluminescence efficiency under similar current-driving conditions. It is, therefore, concluded that Alq_3 cations are unstable and their degradation products are fluorescence quenchers.

The above mechanism can be employed to explain other phenomena pertaining to OLED stability. In the correlation between a lower IP of a HTL and higher device stability, a lower IP of the HTL leads to a more difficult injection of holes into the Alq_3 as a result of a higher hole-injection barrier at the HTL–Alq_3 interface [323]. Introducing a layer of CuPc at the ITO contact forms a barrier to hole-injection from CuPc to NPB and thus reduces hole-injection into the HTL [30]. Doping the HTL with rubrene forms hole traps and thus leads to reduction in the hole mobility [327].

In all the three cases, hole-injection into Alq_3 is reduced and a high density of electrons forms in the Alq_3 regions adjacent to the HTL/Alq_3 interface. The higher density of electrons in these Alq_3 regions leads to a shorter lifetime of the cationic Alq_3 species as a result of rapid recombination with electrons. High concentration of electrons at the HTL/Alq_3 interface also promotes direct formation of the excited states, further reducing the density of cationic Alq_3 species. As a result, Alq_3 degradation is reduced, leading to an improved OLED stability. It should be pointed out that the work does not exclude morphological stability as a factor influencing device lifetime, particularly for hole-transport molecules with low glass transition temperatures and for devices operated or stored at high temperatures. The argument based on Alq_3 cations, however, fails in explaining the improvement of operational stability by treatments of ITO in oxygen or fluorine-containing plasma, where both enhanced hole-injection and improved durability are simultaneously observed, indicating that several mechanisms are operating [256,326].

6.1.5. Mobile ionic impurities

An appropriate driving scheme has recently been considered to be one of the important factors for the improvement in the performances of OLEDs. It has been found that at a constant current the operational stability could be improved using an ac excitation scheme, which provided a reverse bias voltage component in the temporal waveform [30]. Similar effects have been observed by using a constant voltage-driving mode where a decrease of both luminance and current density was observed, while device performance was partially recovered when the bias was reversed and reapplied [339,340]. However, the reversed bias application did not cause a change in the quantum efficiency, even though it significantly contributed to the improvement in luminance–voltage characteristics.

Ionic impurities are considered to be a dominant factor, which cause recoverable degradation in OLEDs through the formation of an internal electric field in the opposite direction to the applied external field [341]. The strength of the internal electric field may become comparable to that of the external electric field. The formation of an internal field leads to a decrease in the effective electric field for charge injection and transport and thus requires a relatively high operating voltage. In this model, the overall luminance decay is partly attributed to the increased ion concentration in the OLED. Possible mobile ion species include In, Sn, Mg, etc. from the electrodes, or other contaminants incorporated during the fabrication process.

Fast indium diffusion at the In/perylenetetracarboxylic diahydride interface has been reported [342], and attributed to ion repulsion originating from metal ionization. In small molecule OLEDs, only little or no indium diffusion was detected when the devices were stored at room temperature. However, it was found that indium diffused almost throughout the entire organic films after prolonged operation, and the presence of indium in organic films significantly reduced quantum efficiency [343]. This is likely to be one of the sources of mobile ion species observed in the reverse bias test.

Although the mobile ionic impurities can be used to explain the early rapid decay of luminance, it may originate from the reaction of OLEDs with contamination introduced into the package at the time of construction: either water/oxygen adsorbed on to the surface of the devices or out-gassed products of the epoxy cure. Once this initial contamination is scavenged by reactions at the contact, the subsequent degradation is slowed.

6.2. Non-emissive sites

OLEDs are extremely sensitive to moisture. Without encapsulation the evolution of device failure can be clearly observed. Non-emissive spots or dark spots develop initially and continuously grow with time (Fig. 41). The increase in diameter is roughly proportional to the square root of time, indicating a diffusion-controlled process. Several mechanisms have been proposed to account for the formation and growth of dark spots. The growth of dark spots can be substantially reduced by the combination of encapsulation and desiccants.

6.2.1. High local field

In early models, the formation of dark spots was attributed to high local fields or high local Joule heating. (1) High local fields in areas of electrode non-uniformity cause hot spots in OLEDs, and consequently result in pinholes in the top electrode, enhanced oxidation, and/or ablation of the top electrode [344]. (2) High local Joule heating by high local currents causes interdiffusion at the HTL/ETL interface and leads to a reduction of currents in the mixed area [345]. The models have no longer been considered as they are in disagreement with later observations.

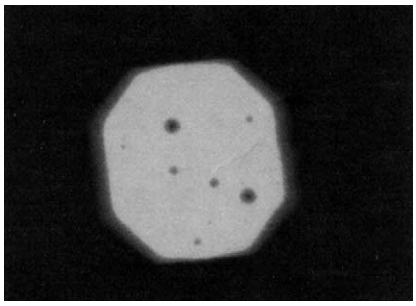

Fig. 41. Dark spots of an Alq_3-based OLED.

6.2.2. Reaction of cathodes with moisture

The formation and growth of dark spots have been thoroughly studied and understood on Alq_3-based OLEDs with MgAg cathodes. The following observations have been reported in the literature [346–349]:

1. The dark spots do not grow in number, but only in size, and are circular in shape, indicating that the dark regions are presumably created by initial conditions.
2. The growth of dark spots is independent of the electrical bias of the OLEDs but is accelerated by increasing the humidity in the ambient.
3. After continuous operation the non-emissive regions of the stressed device have the same dimension as those on the unstressed sample when exposed to the same ambient conditions. This is clear evidence that the growth of these regions is not an electric field-dependent process.
4. Increasing the metal thickness decreases the density of black spots, but could not completely eliminate them. On the other hand, smoothening substrates results in fewer dark spots.
5. The dark spots exhibit photoluminescence, indicating that the dark regions are still active. Further examinations of the devices with a Nomarski optical microscope reveal that the dark spots coincide with hemispheric dome-like textures centered around micron-sized defects. These observations indicate that dark spots originate from lack of carrier injection, rather than from a luminescence quenching process.
6. In photofluorescence by UV excitation, the dark spots appear slightly brighter than the surrounding background. Microscopic infrared spectroscopy reveals the growth of cathode metal hydroxide sites at the metal/organic interface for a majority of the dark spots.
7. When the cathode is peeled off and a new cathode is deposited, the sites of previous dark spots are now emissive, except for a tiny non-emissive central spot. This observation agrees with the finding, in which the Alq_3 at the sites of the dark spots is still functional and that the growth of dark spots is caused by the formation of metal oxides or hydroxides. However, bright circular features, which precisely correspond to the previous dark spot sites, are now observed by fluorescence microscopy. The presence of these features implies that the growth of dark spots is associated with some changes in the underlying Alq_3 layers.

Based on the above observations one model has been proposed, in which dark spots result from the formation of metal oxides or hydroxides at the Alq_3/metal interface initiated by moisture through the pre-existing pinholes on the cathode. A particle or an asperity may exist on the surface of ITO/glass before device construction, or an organic chunk may be deposited on the substrate by spitting of the organic material upon deposition. Both types of particles may have sizes exceeding the thickness of the organic layer, thus causing shadowing effects during deposition. The interruption of complete coverage will give rise to entry points for water and oxygen.

Lim et al. [350,351] used silica micro-particles to intentionally create size-controllable pinholes on the cathode layer in OLEDs, and observed initial formation of dark spots and progressive growth in time. Due to usage of particles of various diameters, they were able to linearly correlate the growth rate with pinhole size. The areas of the dark spots increased almost linearly with the time, and the slope showed a linear dependence on particle size. The studies provide an addition support to the model, in which dark spot formation is due to pinholes on the protective layer that creates pathways for water or oxygen permeation. Moreover, the diameter of the dark spots increased proportionally with the square root of the time, suggesting a diffusion-limited process.

A real-time study has been conducted on the evolution of dark spots during device operation by using a transparent OLED [352]. The transparent cathode has degradation characteristics similar to those of conventional OLEDs, while the transparency makes possible the real-time study of dark spot growth by simultaneously measuring optical microscopy images and atomic force microscopy (AFM) images. The morphology of the cathode film was monitored by AFM at the cathode side in the region corresponding to the formation and growth of a dark spot identified by EL imaging taken from the glass side. The results showed that there were no identifiable defects in the AFM scans where the dark spots were present, and no topographical differences between the dark spots and the bright area surrounding them. The result constitutes a supplementary to the existing model as it reveals that moisture may also diffuse into the device through microscopic pinholes, cracks, or grain boundaries in the cathode, which are too small to be detected by AFM.

Dark spots have been reported for OLEDs with various cathode metals [353]. Since the formation of dark spots are related to the growth of metal oxide and hydroxide at cathode/organic interfaces, the growth rates are expected to have a dependence on the chemical stability of the metals. Kanai et al. [354] found that the dark spot growth rate, during storage in dry N_2, decreased from 1.7% per day in the structure ITO/α-NPD/Alq_3/MgAg to 0.04% per day in the structure ITO/α-NPD/Alq_3/Cz-TPD/Ag. The improvement of storage stability is mainly due to the use of Ag, which is chemically inert.

7. OLED displays

7.1. Displays on glass

Emerging as the leading next-generation flat panel display technology, OLED technology offers some novel display solutions. OLEDs are bright, emissive, colorful devices that offer low-power consumption, wide viewing angle, good contrast, and video rate operation. OLEDs are also thermally stable with adequate operating lifetime for certain applications. OLED displays can be organized as either passive or active-matrix displays. The passive-matrix OLED displays utilize a simple structure well suited for low cost, low information applications such as alphanumeric displays. However, this does require that pixels are driven under pulsed conditions at high current density, and both resistive losses in the conductive tracks and efficiency reductions for the diodes at high current densities limit the number of pixels. In contrast, active-matrix OLED displays use an integrated electronic backplane as its substrate, which lends itself to high-resolution, high-content applications such as videos and graphics.

Today, many companies are focused on introducing monochrome and multicolor passive-matrix OLED displays for various users. Pioneer is currently shipping passive-matrix OLED displays for use in automotive applications. The displays use a simple matrix with 256×64 dots at 100 cd/m^2 with a contrast of 100:1 or higher. More recently, Motorola introduced a cellular phone with an

OLED display from Pioneer. Sanyo also demonstrated the use of passive-matrix OLED displays in cellular phones. These devices have a 1.3 in. display diagonal and a dot count of 120 × 60.

Rapid progress has also been made to develop full-color, passive- or active-matrix OLED displays. Pioneer has developed a 5.2 in. full-color passive-matrix display with 320 × 240 pixels, 260,000 colors and targeted at car navigation systems. NEC has prototyped a 5.7 in. full-color display with a brightness of 100 cd/m^2. Eastman Kodak Company signed an inclusive alliance contract in February 1999 with Sanyo Electric to develop, manufacture, and sell OLED displays. In this cooperative effort, the two companies concentrated on developing and producing the active-matrix display expected to be the standard for OLED displays in the future. The company's first success occurred in September 1999 with a demonstration of the first 2.4 in. active-matrix full-color OLED display. The device contains an RGB delta arrangement with a dot count of 852 × 222. This was followed by the first 5.5 in. active-matrix full-color OLED display demonstration on 10 May 2000. The display has 320 × RGB × 240 (QVGA) pixels at a 0.116 mm × 0.348 mm pitch in an RGB stripe arrangement with more than 150 cd/m^2 of brightness. Sony demonstrated a full-color 13.0 in. SVGA active-matrix OLED display with 800 × RGB × 600 pixels [355], and Toshiba Matsushita Display Technology announced a 17 in. full-color OLED display offering a resolution of 1280 × 768 pixels.

Other developers on molecular OLED-base displays include eMagin Corporation and Universal Display Corporation (UDC). Currently, eMagin is fabricating microdisplays for head-wearable displays, viewfinders and some military applications, and UDC is developing stacked OLEDs, a vertical stack of red, green, and blue pixels based on transparent cathode technology.

7.1.1. Matrix addressing

In passive-matrix OLED displays, the individual pixels are defined by the overlap of ITO columns (anodes) and metal rows (cathodes). The formation of anode strips involves applying photoresist on the ITO, using a photomask during exposure, and then etching the materials. However, it is very difficult to create fine-definition patterns for the cathode by photolithography because the developer and the etching solution damage the underlying organic compounds. The simplest approach to form cathode patterns is vacuum evaporation of the cathode metal through a shadow mask. However, this method cannot form fine-definition patterns because there are limits to the manufacturing precision and to the strength of the metal mask. It is, therefore, important that engineers must produce the cathode patterns before forming the organic layers. An integral shadow mask approach has been used to pattern the cathode. The integral shadow mask structure consists of inverse, tapering cathode separators, which are formed of photopolymer or inorganic materials. Then organic and cathode materials are deposited onto the substrate, and these separators serve as the shadow masks for automatic cathode patterning. The integrated shadow mask is applicable to a passive-matrix full-color display as well when RGB materials are respectively coated on different portions between two neighboring separators. In autumn 1997, engineers in Pioneer formed the inverse, taping cathode separators using negative photopolymer for automatic cathode patterning, and introduced to the market a world premier monochrome OLED display driven passively [356].

Passive-matrix 120 × 60 OLED displays with a pixel size 0.19 mm × 0.42 mm have been fabricated in Kodak [357]. An integral shadow mask consists of pillar and base structures, as indicated in Fig. 42. The pillars serve as the separators for automatic organic and cathode patterning. The insulating base layer is required to prevent shorting between the cathode and anode layers in regions where the organic layers are absent (or thin) as a consequence of unavoidable shadowing by the pillar during organic deposition. AZ5200 series positive photoresist is used for both the base and pillar layers. This ''dual-tone'' resist is processed in the positive mode to pattern the base layer and in

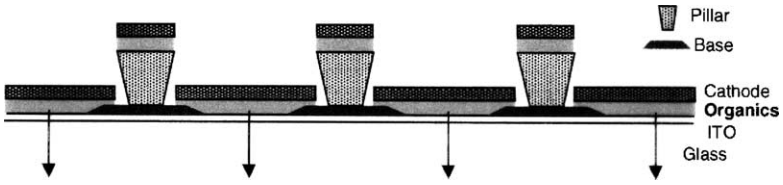

Fig. 42. Integral shadow mask structure used for cathode row isolation [357].

the negative mode (image reversal) to create the retrograde profile pillar structure. In the positive mode (base), the areas exposed to the image defining exposure become more soluble in developer. For the negative mode process (pillar), the areas exposed during the image defining exposure are cross-linked by a post-exposure bake step, becoming less soluble in developer compared to the regions that are subsequently exposed during a flood exposure step. A common commercial developer is used for both the base and pillar processing. Use of the same photoresist and developer for both the base and pillar layers has been found to be convenient, and avoids potential contamination and incompatibility issues.

Fig. 43 shows the pillar edge profile and resulting cathode isolation. Process conditions were optimized to yield the approximately 45° retrograde pillar profile. The retrograde angle of the pillar must be sufficient to ensure that the cathode metal does not coat the sidewalls and electrically short adjacent rows. The required pillar profile is primarily dependent on the relative orientation of the cathode source to the substrate. After deposition of the organic and cathode layers, the display is encapsulated.

Active-matrix OLED displays can be manufactured from a conventional LCD low temperature polysilicon thin film transistor (TFT) process. The standard process requires that a transparent (glass or plastic) substrate first be carefully cleaned, smoothed, and polished. Traditional photolithography and deposition techniques are used to form metal interconnections and silicon thin films. Etching processes pattern the device to create digital circuitry and remove the silicon in areas where OLEDs are to be placed. Then a dielectric layer deposited covers all of the silicon and active device areas on the substrate except the transparent conductors. The transparent conductors are cleaned and the organic materials are deposited using a mask placed over the substrate. Various materials are coated in sequence and on different portions of the substrate to obtain the various colors, and to optimize performance of the light emitters.

The power consumption of an OLED display is proportion to the number of pixels that are turned on, the grayscale levels at each pixel, and the overall luminance needed for the display. In the

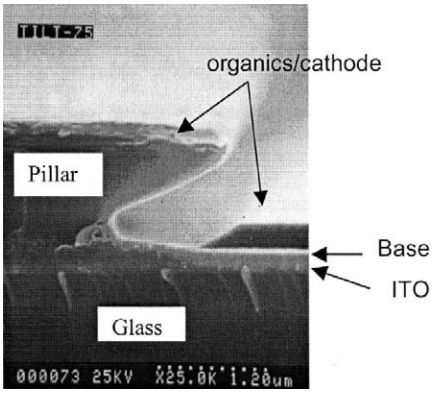

Fig. 43. Cross-sectional SEM image showing cathode isolation by the integral shadow mask [357].

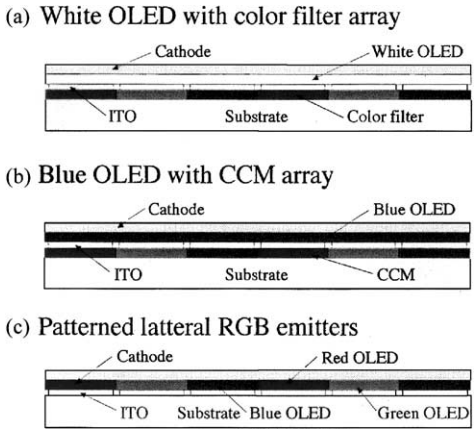

Fig. 44. Three approaches to form full-color OLED displays.

case of the active-matrix OLED display, the internal luminance operating point is governed by the aperture ratio at each pixel. The TFT pixel circuits used for controlling each pixel occupy space and may result in a low aperture ratio.

7.1.2. Color

In recent years, applications aiming at a full-color OLED display are making steady progress. Prototypes have been demonstrated or reported by several research organizations, and each of them took a different approach to the fabrication (Fig. 44). For example, the first approach uses white OLEDs with color filter arrays (Fig. 44a). This method has no need to pattern organic materials and is able to adopt the color filter technique used in a LCD panel [358]. But the efficiency of emitting light has a significant drop by passing through the color filters. The second one utilizes blue OLEDs as a light source with fluorescent color arrays as color-changing media (CCM) to obtain RGB colors (Fig. 44b) [359,360]. This method does not require organic layer patterning, but its low color change efficiency especially for red color is undesirable. The third approach employs patterned lateral RGB emitters (Fig. 44c) [361]. This method has a good possibility of high luminous efficiency although patterning of organic layers is difficult. Furthermore, there are other methods such as stacked RGB emitters, color changed emitters by finite-source dye-diffusion, and so on.

7.1.2.1. Color filter. Coumarin 6-doped Alq_3 and rubrene-doped TPD formed a white OLED with a CIE color coordinate of (0.39, 0.55). Based on this double-emitting layer cell, a passive-matrix full-color display was formed with a pixel number of 256×64 and a luminance of 100 cd/m^2. ITO anodes were formed in vertical stripes, and the cathode was prepared in horizontal stripes after depositing organic layers. The display panel was then encapsulated, and a color filter plate formed on a glass substrate was stacked onto the display panel with adhesive. When the luminance of the cell was 1000 cd/m^2, the luminance of green, yellow and red colors with a color filter was 400, 400 and 150 cd/m^2, respectively.

7.1.2.2. Color change media. A full-color organic display with 10 in. diagonal size and high-resolution (VGA) was reported. This display was based on blue OLEDs with color-changing media. A tapered In_2O_3–ZnO with an Al auxiliary electrode was used as both an anode and separator. The emitting layer was formed of distyrylarylene derivatives. By introducing a fluorescent dopant into the emitting layer, a high efficiency of 6 lm/W was achieved. Color-changing media were composed of a transparent resin or

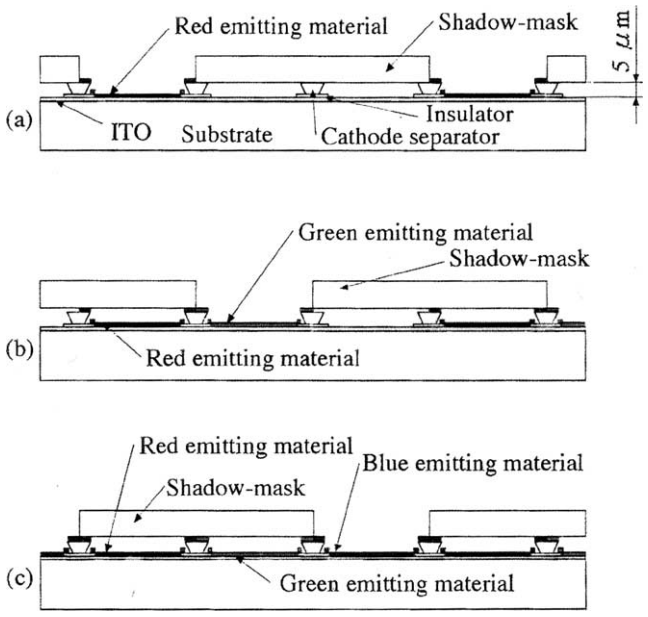

Fig. 45. Schematic of patterning lateral RGB pixels by using a shadow mask moving mechanism.

photoresist and organic fluorescent dyes. The fabrication processes are similar to those in a pigments dispersed color filter used for LCD.

7.1.2.3. Patterned lateral RGB emitters. Pioneer prototyped a 5.2 in. 1/4 VGA passive-matrix OLED display using the integral shadow masks, coupled with selective deposition of RGB emitters using an automatic high accuracy shadow mask moving mechanism in a vacuum chamber (Fig. 45) [362]. The display has $(320 \times 3) \times 240$ pixels with an aperture ratio of 83%. The power consumption is 1.4 W at a luminance of 60 cd/m^2. In October 1999, Eastman Kodak and Sanyo Electric jointly announced the development of a high quality, 2.4 in. diagonal full-color active-matrix OLED display using the same mask moving mechanism [363]. The display has $(284 \times 3) \times 240$ pixels with an aperture ratio of 25%. The power consumption is 0.4 W at a luminance of 150 cd/m^2.

Selective deposition of RGB emitters using an automatic high accuracy shadow mask moving mechanism is most promising because it fully utilizes the high efficiency of OLEDs. The difficulties in this approach are how to prepare a metal shadow mask with several tens of micron openings and how to align the mask to a glass panel in vacuum chamber with a tolerance of several microns. This tolerance is the sum of the errors in mask, mask alignment and shadowing caused by substrate to source geometries. Accurate placement of high precision color pixels requires careful design of mechanical subsystems for glass substrate/precision mask handling [122].

7.1.2.4. Commonly used EL materials. The color purity (or CIE coordinates) in OLED displays is of importance, which is controlled by the selection of organic materials and appropriate device structures. The other important requirements are efficiency and luminance stability. The performance of red, green, and blue OLEDs is summarized in Table 3 [357]. The OLED is composed in order of an ITO anode, a NPB HTL, an emitter, an Alq_3 ETL, and a MgAg or LiF/Al cathode. The performance is characterized at 20 mA/cm^2. Some recently reported materials have CIE coordinates more close to NTSC standards.

Table 3
Device performance characteristics

Color	Emitter		Voltage (V)	Efficiency (cd/A)	Half-lifetime (h)	CIE	
	Dopant	Host				*x*	*y*
Red	DCJTB	Alq_3	8.7	3	8000	0.62	0.38
Green	C545T	Alq_3	7.4	8.5	7000	0.31	0.63
Blue	Perylene	ADN	7.6	3.4	4000	0.17	0.26

7.1.3. Encapsulation

After deposition of the organic and cathode layers, the display is encapsulated. Encapsulation is accomplished by bonding a sheet metal canister containing an alkaline earth oxide desiccant (typically CaO or BaO) to the substrate glass using a commercially available UV cured epoxy (Fig. 46) [364]. Encapsulation prevents or limits the enlargement of dark spots and edge growth. Similar to darks spots caused by pinholes in the cathode, edge growth results from moisture penetrating below the cathode at the discontinuity created by the pillar and leads to a reduction in the emitting area of the pixel. A simple calculation indicates that at 20 °C and 60% RH it approximately takes 4 days to transmit 4 μg of H_2O through a 1 mm wide and 40 μm thick adhesive layer. Such amount of water is sufficient to form 3 nm of Al_2O_3 provided that the OLED has an Al cathode with an area of 25 mm × 25 mm [365]. Therefore, desiccants are required to absorb water that permeates through the adhesive seal.

7.1.4. Thin film transistors

An active-matrix comprises a TFT in series with each pixel. These elements are incorporated primarily to create a sharp threshold to improve the multiplexibility of the display. They are capable of transferring the maximum charge to the pixel capacitance during the address time, and they do not allow significant leakage during the frame time. The active-matrix addressing scheme has several advantages over the passive one, such as no crosstalk, continuous excitation, low-power consumption, continuous cathode configuration, and integrated drive electronics.

Active-matrix OLEDs are currently fabricated using polysilicon (poly-Si) on glass. Two primary issues were encountered during the active-matrix OLED display design. First, the electron mobility in poly-Si is substantially lower than that measured on single crystal silicon, and the mobility exhibits a strong dependence on grain size. Secondly, the poly-Si TFTs suffer from large variations in electrical properties due to the nature of the poly-Si crystal growth, making it difficult to generate a uniform current source at each pixel. Several techniques are currently employed for

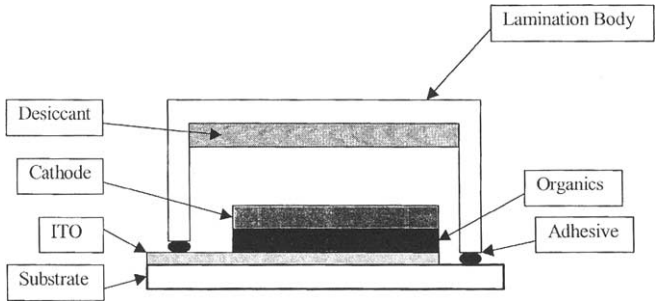

Fig. 46. Cross-sectional view of an encapsulated OLED [365].

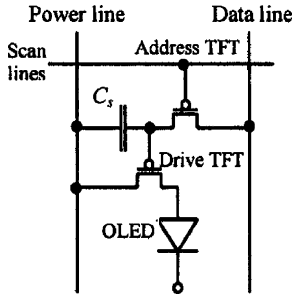

Fig. 47. A two-transistor active-matrix OLED pixel.

crystallization of amorphous films, including low temperature solid phase crystallization, excimer laser annealing and metal seeding [366]. Low temperature solid phase crystallization offers improved performance at the expense of low throughput. Excimer laser annealing can form poly-Si grains of excellent structural quality, while it demands tight control to avoid spatial non-uniformity and suffers from a very narrow process window. The grain-size variation can be reduced by using multiple laser shots, but at a cost to process throughput. With metal seeding, the presence of residual metals in TFTs may result in high leakage currents.

Unlike the driver of a liquid crystal (LC) pixel that can be voltage-switched using a single "address" transistor, the current-controlled emission of an OLED pixel requires at least two transistors to maintain the necessary continuous diode current in the emitting state [367]. In Fig. 47, the drive transistor drives the current for the OLED, and is operated in saturation to overcome the OLED threshold variation. The address transistor acts as a switch to sample and hold a voltage on the gate of the drive transistor. The major cause of luminance non-uniformity is the variation in the drive transistor. This transistor has a high level of output characteristic variation due to the nature of the polysilicon grain growth. A four-transistor circuit has been proposed to reduce the effects of the transistor threshold voltage variation, resulting in a four-fold improvement in luminance uniformity as compared to the basic two-transistor circuit.

The trend towards flexible displays will lead to more demanding requirements for TFT technology in the future [368]. In flexible displays, the substrate temperature is limited to 150 °C for polyethyleneterephthalate (PET) and 200 °C for polyethersulphone (PES). This poses a significant challenge for Si TFTs, because much higher temperatures are typical required. Several approaches to attaining high-performance CMOS transistors on plastic are presently being pursued by various groups in the world. These include the direct fabrication on plastic and the transfer of TFTs onto plastic. The fabrication of poly-Si TFTs on PET substrates by laser crystallization and laser doping of sputtered Si films was recently demonstrated [369], and the transfer of transistors or circuitry from a glass substrate to PES by using excimer laser irradiation was also reported [370]. It is likely that with future process optimization, they will be able to meet the performance requirement.

7.1.5. Technology development

7.1.5.1. Equipment for production. It is highly desirable to develop OLED deposition equipment for increasing machine throughput (for instance, 4 min per glass substrate) and for large-size glass substrates (for instance, 300–500 mm). The challenge lies in the fabrication of error-free and high strength masks because the mask requires millions of precision apertures when scaled up to a 300 mm × 400 mm glass size.

A key requirement for fabrication of OLED displays is uniform film deposition over large areas because of the sensitivity of emission color and efficiency on film thickness. Conventional deposition using point sources is unattractive because of the requirement of a large source to substrate separation and the use of substrate rotation to achieve acceptable thin film uniformity. By using a novel extended linear evaporation source translating in a single direction, film non-uniformity of less than 5% has been demonstrated over a 300 mm × 400 mm substrate with a source to substrate separation of 100 mm [371].

7.1.5.2. Phosphorescent OLED displays. More recently, scientists in Princeton University demonstrated light emission from the triplet states through the use of phosphorescent dyes. These phosphorescent OLEDs enable extremely high internal quantum efficiency. Interest is increasing for exploring the application of phosphorescent OLEDs to flat panel displays. Simulations of a full-color active-matrix display (approximately 2 in. diagonal) show that a fluorescent OLED display consumes about 110 mW at 100 cd/m^2, while the use of phosphorescent materials decreases consumption to about 65 mW [372].

It is known that phosphorescent efficiency decreases rapidly at high current densities. This becomes a particular concern for passive-matrix display applications, since these require OLED to be strongly excited by short electrical pulses at high current density. Also, as mentioned previously, problems remain in blue phosphorescent OLEDs, where wide-gap (∼3.5 eV) host materials are required.

7.1.5.3. Flexible OLED displays. In a normal configuration, the OLED is constructed on a glass substrate through which the light is viewed. Recently, OLEDs have been fabricated on plastic or thin-glass substrates to form a flexible OLED. The use of flexible substrates will significantly reduce the weight of flat panel displays and provide the ability to conform, bend or roll a display into any shape. Moreover, it will open the possibility of fabricating displays by continuous roll processing, thus providing the basis for very low-cost mass production.

Gu et al. disclosed a flexible OLED on plastic in a US patent. A flexible OLED display has been demonstrated at Sixth Annual Strategic and Technical Symposium in 1999. The 128 × 64 pixel display (0.4 mm × 0.5 mm pixel size), operating at 100 cd/m^2, was made on a standard PET tape (0.18 mm thick). The display was shown to bend to a radius of curvature of <1 cm [373].

Although for many commercial applications the fabrication of flexible OLEDs is of great importance, technical challenges exist in the process of flexible OLEDs, such as protecting plastic-based OLEDs from moisture and oxygen and utilizing TFT process technology for plastic.

7.2. Displays on Si

7.2.1. Surface-emitting OLEDs

Conventional OLEDs have a transparent substrate, typically ITO glass, through which the light is emitted, and the surface electrode such as MgAg is normally opaque. A surface-emitting OLED structure is definitely required for an active-matrix OLED display fabricated on a Si substrate, which has an important advantage of having on-chip data and scan drivers, allowing for ultrahigh pixel resolution (<10 μm). Despite such importance, there were only a few investigations on surface-emitting OLEDs reporting limited success in fabricating a suitable transparent top electrode.

7.2.1.1. Reversed structures. A surface-emitting OLED can be formed in a reversed structure, where light emits from its top surface through a transparent ITO anode [374]. This device has a novel

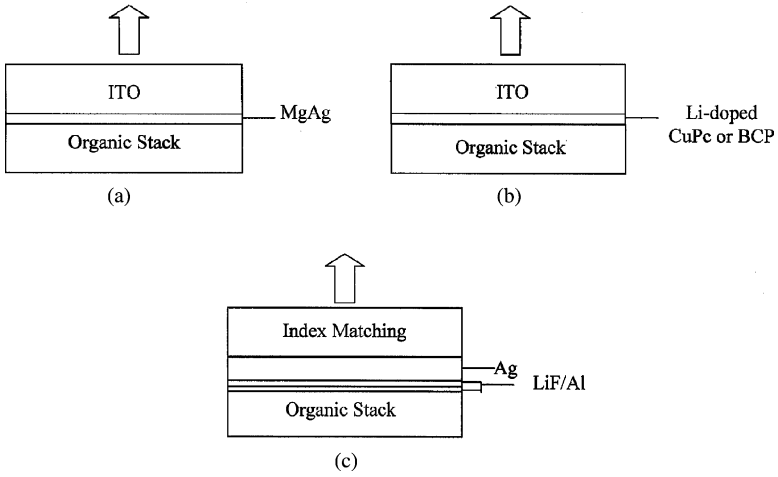

Fig. 48. Various structures of surface-emitting OLEDs.

protective cap layer, which prevents damage to the organic layers during sputter deposition of the anode. An OLED of Si/MgAg/Alq_3/TPD/PTCDA or CuPc/ITO was fabricated and showed an external quantum efficiency of $\eta = 0.15\%$. The low efficiency is mainly attributed to the facts that electron-injection is commonly weak when Alq_3 is deposited on MgAg.

7.2.1.2. Conventional structures

7.2.1.2.1. MgAg/ITO transparent cathodes. A surface-emitting OLED can be formed with a transparent top electrode consisting of a 10 nm thick MgAg layer and a thicker overlying ITO film (Fig. 48a). The MgAg forms a semitransparent cathode with its overlaying ITO film, and is also used as a buffer layer to protect the underlying organic structure from irradiation [375,376]. The OLED after ITO deposition is often leaky, indicative of interelectrode shorts, even though computer simulation indicates that the 10 nm thick MgAg is sufficient to protect the underlying organic structure. Electrical analysis and AFM measurements reveal that catastrophic failure is attributed to the presence of pinholes in the MgAg protective layer [377]. A short-free yield of 90% was achieved at a high deposition rate for ITO by taking several steps to improve the coverage of MgAg on Alq_3.

7.2.1.2.2. Li-doped organic/ITO transparent cathodes. A new transparent top electrode structure was introduced employing a thin film of CuPc instead of MgAg, overlaid by a sputter-deposited ITO film (Fig. 48b) [378]. The CuPc acts as a buffer in reducing the shorting problem caused by the ITO sputtering process. However, the buffer layer forms an electron-injection barrier with both the underlying Alq_3 ETL and the top ITO electrode. Efficient surface-emitting OLEDs are achieved by depositing an ultrathin Li film on the CuPc buffer layer prior to the sputter deposition of ITO [379]. As the CuPc/Li cathode is only 65–85% transparent in the visible spectrum, it is desirable to have a material with high transparency across the entire visible spectrum, thus motivating the use of a ~90% transparent BCP/Li cathode instead of CuPc/Li [380]. In all the cases, incorporation of Li in the buffer layer by Li diffusion is necessary because Li donates electrons to the buffer layer, increasing its conductivity and reducing the barrier to electron injection.

7.2.1.2.3. ITO-free transparent cathodes. A multi-layer cathode structure for OLEDs has been reported, that is both optically transmissive and electrically effective as an electron-injecting

contact [381]. It consists of an ultrathin layer of LiF/Al as the electron-injecting contact, a highly conductive silver layer for sheet resistance reduction, and a transparent index-matching layer for enhancement of optical transmission (Fig. 48c). The structure is prepared by conventional thermal evaporation, and yields surface-emitting OLEDs with superior electrical and optical characteristics. The luminance efficiency is 2.75 cd/A as measured from the cathode surface with a reflecting Ag mirror on the ITO glass, which is practically equivalent (∼90%) to a conventional OLED having a thick MgAg cathode. Another critical advantage of this surface-emitting structure is that the transparent cathode struc-ture can be easily prepared by conventional thermal evaporation without incurring radiation damage.

7.2.2. Color stacked OLEDs

Current research on OLEDs is focusing on the integration of OLEDs into full-color, flat panel displays. The recent success in surface-emitting OLEDs has led to a new kind of integrated full-color pixel: the stacked OLED [382,383]. In this technique, the layers that emit different colors are stacked on top of each other along with the required electrodes to independently address each layer. The advantages of this approach in processing are that the patterning steps and process control requirements are now essentially the same as for a monochrome display. Assuming that the patterning and addressing issues could be satisfactorily resolved, stacked OLEDs will triple the resolution offered by conventionally patterned RGB sub-pixels [384]. In the stacked OLEDs, various transparent cathode structures have been employed [385–387].

7.2.3. Microdisplays

A microdisplay, defined as a display having a diagonal typically less than 1 in., generally relies on active-matrix architecture. Thin film EL displays played a role in microdisplays for monochrome military market applications despite its higher price and power consumption. Reflective liquid crystal displays on Si were beginning to be demonstrated in 1995–1997, and showed promise for higher resolutions and improved power consumption. These displays still required a significant amount of external components and circuitry with moderately high power consumption to operate in a color sequential mode.

IBM Research and eMagin Corporation have jointly developed OLEDs on silicon chip technology for direct view applications [388]. The display was fabricated combining OLED

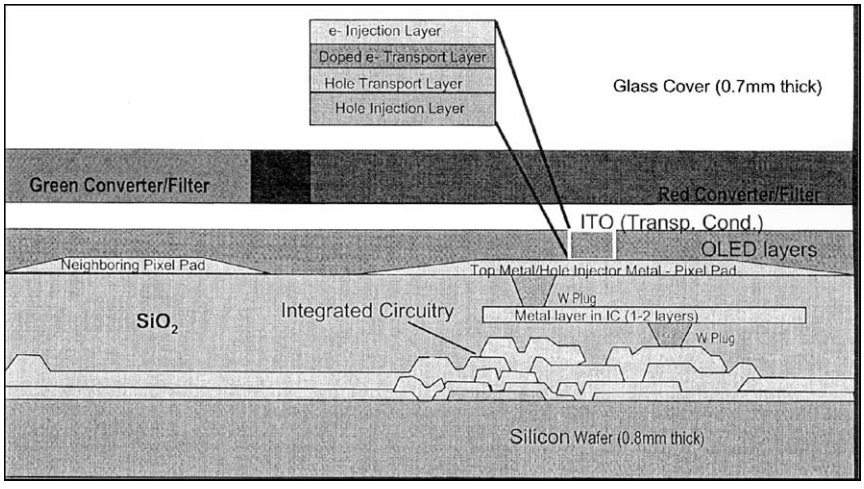

Fig. 49. A full-color active-matrix OLED microdisplay [390].

technology from eMagin with IBM's single crystal silicon chip electronics. The use of silicon chip technology allows a number of functions to be integrated within the display including SRAM memory function at each pixel. The white monochrome microdisplay has SXGA resolution with 1280×1024 pixel format and 12 μm pitch [389]. The size of the display is 19.6 mm in diagonal with an active viewing area of 15 mm × 12 mm and weighing only about 8 g. This active-matrix OLED on Si display has demonstrated real-time video with 256 gray levels. It consumes less than 400 mW of power at a brightness of 200 cd/m^2. A projected half-life in excess of 5000 h at 20 mA/cm^2 is estimated. In parallel, eMagin Corporation is developing a full-color SVGA (852×600 pixels) microdisplay having an analog RGB interface compatible with that of typical desktop monitors. This was accomplished by processing triad color filters over the surface of a white display (Fig. 49) [390,391].

8. Summary and outlook

A great deal of progress has been made in organic electroluminescent materials and devices. Intensive research activities in EL materials over the last three to four years have yielded OLEDs with remarkable color fidelity, device efficiencies and operational stability.

Charge injection and transport are critical in determining operating voltage and luminance efficiency. Photoelectron spectroscopy has been extensively employed to study the electronic structures and chemistry of the electrode/organic interface, and the results provide physical insights to the nature of the interface. Various cathode materials and different surface treatments of ITO have been developed, leading to substantial enhancement of charge injection. In OLEDs the hole current is limited by injection, and the electron current is strongly influenced by the presence of traps owing to metal–organic interactions. It is thus important in the future to develop Ohmic contacts with excellent injection properties and high interface stability. For low-power consumption, it is highly desirable to design EL materials with superior electron mobilities. This task is challenging, considering that there are additional constraints on other material parameters such as appropriate energy-level alignments with other materials. Doping is an effective approach to voltage reduction, but the formation of quenching centers in the emissive zone by rapid dopant diffusion is a prime concern.

Luminance efficiency is mainly limited by non-radiative decay of excited states and internal optical loss of light. The recombination in a fluorescent OLED is mainly non-radiative due to the selection law of spin conservation. Light emission through phosphorescent dyes has been utilized in OLEDs, and a maximum luminous efficiency of 40 lm/W has been demonstrated. However, the efficiency drops significantly with current density, posing a limitation to passive-matrix addressing. Long-term operational stability also needs to be further investigated before extending its application to flat panel displays. For improving extraction efficiency, current research activity is directed toward various surface modifications, whereas a structure fitted to the fabrication of a device array is still lacking.

OLEDs have achieved long operational stability. Operation at display-level brightness to beyond 10,000 h is commonly achieved with little loss of brightness. While these capabilities are adequate for some products, new materials and structures need to be developed for increased brightness and longer lifetimes for use in more demanding applications. There are many studies of degradation processes now in the literature, and particularly important is the identification of Alq_3 cations responsible for the device instability. Several approaches to improve operational stability have been proposed, including optimizing anode contacts, introducing appropriate dopants, and reducing Alq_3

cations, but a well-accepted model has not been established. Material advances such as increasing the upper temperature over which OLEDs can operate without accelerated deterioration will also be needed. The formation and growth of non-emissive spots are well understood and attributed to the formation of metal oxides or hydroxides at the ETL/cathode interface initiated by moisture penetration. The growth of dark spots can be substantially reduced by the combination of encapsulation and desiccant.

The performance of organic LEDs meets many of the targets necessary for applications in displays. Passive-matrix addressed displays are attractive, as the device construction is relatively simple, but both resistive losses in the conductive tracks and efficiency reductions for the diodes at high current densities limit its application. Advanced active-matrix displays have been demonstrated and are expected to be the standard for OLED displays in the future. Color pattering to form lateral RGB emitters using a shadow mask moving mechanism offers the advantages of high luminance efficiency, while the challenge lies in the fabrication of error-free and high strength masks for large-size glass substrate. The trend toward low-power, lightweight and rugged displays leads to the development of flexible OLEDs, while technical challenges exist in protecting plastic-based OLEDs from moisture and adopting TFT process technology for plastic.

Acknowledgements

The author, L.S. Hung would like to acknowledge the grant (Project #9380017) from City University of Hong Kong for his research on OLEDs and C.H. Chen would like to thank the National Sciences Council of Taiwan and the Microelectronics & Information Systems Research Center of National Chiao Tung University for support of his OLED materials & device research and technology development. Literature survey on molecular organic materials was aided by many talented graduate students of his OLED team of NCTU whose names can be found at the website: http://oled.eic.nctu.edu.tw of NCTU.

References

[1] E. Gurnee, R. Fernandez, US Patent 3172862 (1965).
[2] M. Pope, H. Kallman, P. Magnante, J. Chem. Phys. 38 (1963) 2042.
[3] C.W. Tang, US Patent 4356429 (1982).
[4] C.W. Tang, S.A. VanSlyke, Appl. Phys. Lett. 51 (1987) 913.
[5] R. Friend, J. Burroughes, D. Bradley, WO Patent 90/13148 (1990).
[6] R. Friend, J. Burroughes, D. Bradley, US Patent 5247190 (1993).
[7] M.A. Baldo, M. Deutsch, P.E. Burrows, H. Gossenberger, M. Gerstenberg, V. Ban, S.R. Forrest, Adv. Mater. 10 (1998) 1505.
[8] S. Hufner, Photoelectron Spectroscopy, 2nd ed., Springer, Berlin, 1996.
[9] N. Karl, K.H. Kraft, J. Marktanner, M. Munch, F. Schatz, R. Stehle, H.M. Uhde, J. Vac. Sci. Technol. A17 (1999) 2318.
[10] D.J. Pinner, R.H. Friend, N. Tessler, J. Appl. Phys. 86 (1999) 5116.
[11] M. Pope, H.P. Kallmann, P. Magnante, J. Chem. Phys. 38 (1963) 2042.
[12] S.A. VanSlyke, C.W. Tang, US Patent 4,539,507 (1985).
[13] C.W. Tang, S.A. VanSlyke, Appl. Phys. Lett. 51 (1987) 913.
[14] C.W. Tang, C.H. Chen, R. Goswami, US Patent 4,769,292 (1988).
[15] C.W. Tang, S.A. VanSlyke, C.H. Chen, Appl. Phys. Lett. 51 (1987) 913.
[16] Y. Shirota, J. Mater. Chem. 10 (2000) 1.
[17] U. Mitschke, P. Bauerle, J. Mater. Chem. 10 (2000) 1471.
[18] J. Kido, Phys. World 12 (1999) 27.
[19] J. Salbeck, Ber. Bunsenges. Phys. Chem. 100 (1996) 1667.

[20] C.H. Chen, J. Shi, C.W. Tang, Macromol. Symp. 125 (1997) 1.
[21] C.H. Chen, J. Shi, Coord. Chem. Rev. 171 (1998) 161.
[22] D. Zou, T. Tsutsui, Funct. Mater. 18 (1998) 36(in Japanese).
[23] P.E. Burrows, S.R. Forrest, M.E. Thompson, Curr. Opin. Solid State Mater. Sci. 2 (1997) 236.
[24] Y. Ohmori, K. Yoshino, Denki Zairyo Gijutsu Zasshi 6 (1997) 2.
[25] A. Kraft, A.C. Gimsdale, A.B. Holmes, Angew. Chem. Int. Ed. 37 (1998) 402.
[26] M. Grell, D.D.C. Bradley, Adv. Mater. 11 (1999) 895.
[27] R.H. Friend, R.W. Gymer, A.B. Holmes, J.H. Burroughes, R.N. Marks, C. Taliani, D.D.C. Dos Santos, D.A. Bradley, J.L. Bredas, M. Logdlund, W.R. Salaneck, Nature 397 (1999) 121.
[28] M. Thelakkat, H.-W. Schmidt, Polym. Adv. Technol. 9 (1998) 429.
[29] I.-M. Chan, W.-C. Cheng, F.C. Hong, Asia Display/IDW'01, 2001, p. 1483.
[30] S.A. VanSlyke, C.H. Chen, C.W. Tang, Appl. Phys. Lett. 69 (1996) 2160.
[31] Y. Shirota, Y. Kuwabara, H. Inada, Appl. Phys. Lett. 65 (1994) 807.
[32] Y. Yang, A.J. Heeger, Appl. Phys. Lett. 64 (1994) 1245.
[33] Y. Cao, G. Yu, C. Zhang, R. Menon, A.J. Heeger, Synth. Met. 87 (1997) 171.
[34] Z.B. Deng, X.M. Ding, S.T. Lee, W.A. Gambling, Appl. Phys. Lett. 74 (1999) 2227.
[35] D.B. Romero, M. Schaer, L. Zuppiroli, B. Cesar, B. Francois, Appl. Phys. Lett. 67 (1995) 1659.
[36] F. Huang, A.G. MacDiamid, B.R. Hsieh, Appl. Phys. Lett. 71 (1997) 2415.
[37] J. Blochwitz, M. Pfeiffer, T. Fritz, K. Leo, Appl. Phys. Lett. 73 (1998) 729.
[38] A. Yamamori, C. Adachi, T. Koyama, Y. Taniguchi, Appl. Phys. Lett. 72 (1998) 2147.
[39] Y. Sato, T. Ogata, S. Ichinosawa, M. Fugono, H. Kanai, Proc. SPIE Org. Light Emitting Mater. Dev. III 3797 (1999) 198.
[40] A. Elschner, F. Bruder, H.-W. Heuer, F. Jonas, A. Karbach, S. Kirchmeyer, S. Thurm, R. Wehrmann, Synth. Met. 111 (2000) 139.
[41] T.M. Brown, J.S. Kim, R.H. Friend, F. Cacialli, R. Daik, W.J. Feast, Appl. Phys. Lett. 75 (1999) 1679.
[42] A. Elschner, F. Jonas, S. Kirchmeyer, K. Wussow, Asia Display/IDW'01, vol. 1427, Nagoya, Japan, 2001.
[43] F. Nuesch, F. Rotzinger, L. Si-Ahmed, L. Zuppioli, Chem. Phys. Lett. 288 (1998) 861.
[44] F. Nuesch, E.W. Forsythe, Q.T. Le, Y. Gao, L.J. Rothberg, J. Appl. Phys. 87 (2000) 7973.
[45] S.F.J. Appleyard, M.R. Willis, Opt. Mater. 9 (1998) 120.
[46] S.F.J. Appleyard, S.R. Day, R.D. Pickford, M.R. Willis, J. Mater. Chem. 10 (2000) 169.
[47] C. Ganzorig, M. Fujihira, Appl. Phys. Lett. 77 (2000) 4211.
[48] X. Zhou, M. Pfeiffer, J. Blochwitz, A. Werner, A. Nollau, T. Fritz, K. Leo, Appl. Phys. Lett. 78 (2001) 410.
[49] D.-M. Shin, S.-T. Lim, J.S. Choi, J.S. Kim, Thin Solid Films 363 (2000) 268.
[50] S. Funaoka, I. Imae, N. Noma, Y. Shirota, Synth. Met. 101 (1999) 600.
[51] S.A. VanSlyke, C.W. Tang, US Patent 5,061,569 (1991).
[52] Y. Sato, S. Ichinosawa, H. Kanai, IEEE J. Selected Top. Quantum Electron. 4 (1998) 40.
[53] Y. Sato, S. Ichinosawa, T. Ogata, M. Fugono, Y. Murata, Synth. Met. 111 (2000) 25.
[54] D.F. O'Brien, P.E. Purrows, S.R. Forrest, B.E. Koene, D.E. Loy, M.E. Thompson, Adv. Mater. 10 (1998) 1108.
[55] K. Yamashita, T. Mori, T. Mizutani, H. Miyazaki, T. Takeda, Thin Solid Films 363 (2000) 33.
[56] Y. Shirota, K. Okumoto, H. Inada, Synth. Met. 111 (2000) 387.
[57] I.-Y. Wu, J.T. Lin, Y.-T. Tao, E. Balasubramaniam, Adv. Mater. 12 (2000) 668.
[58] I.-Y. Wu, J.T. Lin, Y.-T. Tao, E. Balasubramaniam, Y.Z. Su, C.-W. Ko, Chem. Mater. 13 (2001) 2626.
[59] I.D.L. Albert, T.J. Marks, M.A. Ratner, J. Am. Chem. Soc. 119 (1997) 6575.
[60] C. Giebeler, H. Antonladis, D.D.C. Bradley, Y. Shirota, J. Appl. Phys. 85 (1999) 608.
[61] J. Salbeck, N. Yu, J. Bauer, F. Weissotel, H. Bestgen, Synth. Met. 91 (1997) 209.
[62] U. Bach, K.D. Cloedt, H. Spreitzer, M. Gratzel, Adv. Mater. 12 (2000) 1060.
[63] U. Mitschke, P. Bauerle, J. Mater. Chem. 10 (2000) 1471.
[64] M. Kimura, S.-I. Inoue, K. Shimada, S. Tokito, K. Noda, Y. Taga, Y. Sawaki, Chem. Lett. (2000) 192.
[65] S. Tokito, K. Noda, K. Shimada, S.-I. Inoue, M. Kimura, Y. Sawaki, Y. Taga, Thin Solid Films 363 (2000) 290.
[66] J.F. Hartwig, M. Kawatsura, S.I. Hauck, K.H. Shaughnessy, L.M. Alcazar-Roman, J. Org. Chem. 64 (1999) 5575.
[67] M.C. Harris, S.L. Buchwald, J. Org. Chem. 65 (2000) 5327.
[68] Y.T. Ao, E. Balasubramaniam, A. Danel, P. Tomasik, Appl. Phys. Lett. 11 (2000) 933.
[69] K.R.J. Thomas, J.T. Lin, Y.-T. Tao, C.-W. Ko, Adv. Mater. 12 (2000) 1949.
[70] S. Tokito, K. Noda, H. Fujikawa, Y. Taga, M. Kimura, K. Shimada, Y. Sawaki, Appl. Phys. Lett. 77 (2000) 160.
[71] H. Aziz, Z.D. Popovic, N.-X. Hu, A.-M. Hor, G. Xu, Science 283 (1999) 1900.
[72] Z.D. Popovic, S. Xie, N.-X. Hu, A.-M. Hor, D. Fork, G. Anderson, C. Tripp, Thin Solid Films 363 (2000) 6.
[73] H. Aziz, Z.D. Popovic, Appl. Phys. Lett. 80 (2002) 2180.
[74] Z.D. Popovic, H. Aziz, A. Ioannidis, N.-X. Hu, P.N.M. dos Anjos, Synth. Met. 123 (2001) 179.
[75] N.-X. Hu, S. Xie, Z.D. Popovic, B. Ong, A.-M. Hor, Synth. Met. 111 (2000) 421.
[76] F. Santerre, I. Bedja, J.P. Dodelet, Y. Sun, J. Lu, A.S. Hay, Chem. Mater. 13 (2001) 1739.
[77] Y. Hamada, N. Matsusue, H. Kanno, H. Fujii, Jpn. J. Appl. Phys. 40 (2001) L753.

[78] J. Kido, T. Mizukami, US Patent 6,013,384 (2000).
[79] Z. Liu, J. Pinto, J. Soares, E. Pereira, Synth. Met. 122 (2001) 177.
[80] M. Brinkmann, G. Gadret, C. Taliani, N. Masciocchi, A. Sironi, M. Muccini, Synth. Met. 121 (2001) 1499.
[81] G. Yu, D. Shen, Y. Liu, D. Zhu, Synth. Met. 121 (2001) 1433.
[82] B.J. Chen, W.Y. Lai, Z.Q. Gao, C.S. Lee, S.T. Lee, W.A. Gambling, Appl. Phys. Lett. 75 (1999) 4010.
[83] M. Stoßel, J. Staudigel, F. Steuber, J. Blassing, J. Simmerer, A. Winnacker, H. Neuner, D. Metzdorf, H.-H. Johannes, W. Kowalsky, Synth. Met. 111 (2000) 19.
[84] M.D. Hall, H.B. Schlegel, Chem. Mater. 13 (2001) 2632.
[85] M. Sugimoto, M. Anzai, K. Sakanoue, S. Sakaki, Appl. Phys. Lett. 79 (2001) 2348.
[86] J. Szmytkowski, W. Stampor, J. Kalinowski, Z.H. Kafafi, Appl. Phys. Lett. 80 (2002) 1465.
[87] S. Yin, Y. Hua, S. Chen, X. Yang, Y. Hou, X. Xu, Synth. Met. 111 (2000) 109.
[88] H. Jang, L.-M. Do, Y. Kim, J.G. Kim, T. Zyung, Y. Do, Synth. Met. 121 (2001) 1669.
[89] Y. Shao, Y. Qiu, N.-X. Hu, X. Hong, Chem. Lett. (2000) 1068.
[90] Y. Qiu, Y. Shao, D. Zhang, X. Hong, Jpn. J. Appl. Phys. 39 (2000) 1151.
[91] T. Sano, Y. Nishio, Y. Hamada, H. Takahashi, T. Usuki, K. Shibata, J. Mater. Chem. 10 (2000) 157.
[92] Y. Liu, J. Guo, J. Feng, H. Zhang, Y. Li, Y. Wang, Appl. Phys. Lett. 78 (2001) 2300.
[93] S. Anderson, M.S. Weaver, A.J. Hudson, Synth. Met. 111 (2000) 459.
[94] C. Schmitz, H.-W. Schmidt, M. Thelakkat, Chem. Mater. 12 (2000) 3012.
[95] S. Tokito, K. Noda, H. Tanaka, Y. Taga, T. Tsutsui, Synth. Met. 111 (2000) 393.
[96] N. Johansson, J. Salbeck, J. Bauer, F. Weissortel, P. Broms, A. Andersson, W.R. Salaneck, Adv. Mater. 10 (1998) 1136.
[97] T. Noda, Y. Shirota, J. Am. Chem. Soc. 120 (1998) 9714.
[98] T. Noda, H. Ogawa, Y. Shirota, Adv. Mater. 11 (1999) 283.
[99] G. Gigli, G. Barbarelia, L. Favaretto, F. Cacialli, R. Cingolani, Appl. Phys. Lett. 75 (1999) 439.
[100] S.B. Heidenhain, Y. Sakamoto, T. Suzuki, A. Miura, H. Fujikawa, T. Mori, S. Tokito, Y. Taga, J. Am. Chem. Soc. 122 (2000) 10240.
[101] Y. Sakamoto, T. Suzuki, A. Miura, H. Fujikawa, S. Tokito, Y. Taga, J. Am. Chem. Soc. 122 (2000) 1832.
[102] Y.-T. Tao, E. Balasubramaniam, A. Danel, B. Jarosz, P. Tomasik, Appl. Phys. Lett. 77 (2000) 1575.
[103] Y.T. Tao, E. Balasubramaniam, A. Danel, P. Tomasik, Appl. Phys. Lett. 77 (2000) 933.
[104] P. Lu, H. Hong, G. Cai, P. Djurovich, W.P. Weber, M.E. Thompson, J. Am. Chem. Soc. 122 (2000) 7480.
[105] S. Yamaguchi, T. Endo, M. Uchida, T. Izumizawa, K. Furukawa, K. Tamao, Chem. Lett. (2001) 98.
[106] M. Uchida, T. Izumizawa, T. Nakano, S. Yamaguchi, K. Tamao, K. Furukawa, Chem. Mater. 13 (2001) 2680.
[107] C.W. Tang, S.A. VanSlyke, C.H. Chen, J. Appl. Phys. 65 (1989) 3610.
[108] J. Shi, C.W. Tang, Appl. Phys. Lett. 70 (1997) 1665.
[109] M.A. Baldo, M.E. Thompson, S.R. Forrest, Nature 403 (2000) 750.
[110] J.L. Fox, C.H. Chen, US Patent 4,736,032 (1988).
[111] T. Inoe, K. Nakatani, Japanese Patent 6,009,952 (1994).
[112] J. Ito, Japanese Patent 7,166,160 (1995).
[113] T.G. Pavlopoulos, P.R. Hammond, J. Am. Chem. Soc. 96 (1974) 6568.
[114] C.H. Chen, C.W. Tang, J. Shi, K.P. Klubek, US Patent 6,020,078 (2000).
[115] C.H. Chen, C.-H. Chien, T.-H. Liu, in: Proceedings of the International Conference on Mater. Adv. Tech. (ICMAT 2001), Singapore, 2001, p. 221 (Abstracts).
[116] C.H. Chen, C.-H. Chien, T.-S. Liu, Thin Solid Films (submitted).
[117] K. Yamashita, J. Futenma, T. Mori, T. Mizutani, Synth. Met. 111 (2000) 87.
[118] H. Murata, C.D. Merritt, H. Inada, Y. Shirota, Z.H. Kafafi, Appl. Phys. Lett. 75 (1999) 3252.
[119] Y. You, Y. He, P.E. Burrows, S.R. Forrest, N.A. Petasis, M.E. Thompson, Adv. Mater. 12 (2000) 1678.
[120] H. Yanai, D. Yoshizawa, S. Tanaka, T. Fukuda, M. Akazome, K. Ogura, Chem. Lett. (2000) 238.
[121] S. Capecchi, O. Renault, D.-G. Moon, M. Halim, M. Etchells, P.J. Dobson, O.V. Salata, V. Christou, Adv. Mater. 12 (2000) 1591.
[122] G. Rajeswaran, M. Itoh, M. Boroson, S. Barry, T.K. Hatwar, K.B. Kahen, K. Yoneda, R. Yokoyama, T. Yamada, N. Komiya, H. Kanno, H. Takahashi, SID'00 Digest 40 (2000) 1.
[123] Y. Fukuda, T. Watanabe, T. Wakimoto, S. Miyaguchi, M. Tsuchida, Synth. Met. 111 (2000) 1.
[124] C.H. Chen, J. Shi, K.P. Klubek, US Patent 5,908,581 (1999).
[125] N. Komiya, R. Nishikawa, M. Okuyama, T. Yamada, Y. Saito, S. Oima, K. Yoneda, H. Kanno, H. Takahashi, G. Rageswaran, M. Itoh, M. Boroson, T.K. Hatwar, in: Proceedings of the 10th International Workshop on Inorg. and Org. EL (EL'00), Hamamatsu, Japan, 4 December 2000, p. 347.
[126] Y. Hamada, H. Kanno, H. Fujii, T. Tsujioka, H. Takahashi, ACS Poly Millennial 2000 Abs., 2000, p. 167.
[127] T.K. Hatwar, G. Rajeswaran, J. Shi, Y. Hamada, H. Kanno, H. Takahashi, in: Proceedings of the 10th International Workshop on Inorg. and Org. EL (EL'00), Hamamatsu, Japan, 4 December 2000, p. 31.
[128] R.H. Young, C.W. Tang, A.P. Marchetti, Appl. Phys. Lett. 80 (2002) 874.
[129] Z.Y. Xie, L.S. Hung, S.T. Lee, Appl. Phys. Lett. 79 (2001) 1048.

[130] C.H. Chen, C.W. Tang, J. Shi, K.P. Klubek, Thin Solid Films 363 (2000) 327.
[131] B. Chen, X. Lin, L.F. Cheng, C.-S. Lee, W.A. Gambling, S.-T. Lee, J. Phys. D: Appl. Phys. 34 (2001) 30.
[132] X.H. Zhang, B.J. Chen, X.Q. Lin, O.Y. Wong, C.S. Lee, H.L. Kwong, S.T. Lee, S.K. Wu, Chem. Mater. 13 (2001) 1565.
[133] X.Q. Lin, B.J. Chen, X.H. Zhang, C.S. Lee, H.L. Kwong, S.T. Lee, Chem. Mater. 13 (2001) 456.
[134] X.T. Tao, S. Miyata, H. Sasabe, G.J. Zhang, T. Wada, M.H. Jiang, Appl. Phys. Lett. 78 (2001) 279.
[135] M. Mitsuya, T. Suzuki, T. Koyama, H. Shirai, Y. Taniguchi, Appl. Phys. Lett. 77 (2000) 3272.
[136] L.C. Picciolo, H. Murata, Z.H. Kafafi, Appl. Phys. Lett. 78 (2001) 2378.
[137] S. Toguchi, Y. Morioka, H. Ishikawa, A. Oda, E. Hasegawa, Synth. Met. 111 (2000) 57.
[138] M. Ichimura, T. Ishibashi, N. Ueda, S. Tamura, in: Proceedings of the 3rd International Conference on EL Mol. Mater. Relat. Phenom. (ICEL-3), O-29, Los Angelos, CA, USA, 5–8 September 2001 (Abstracts).
[139] D.U. Kim, S.H. Paik, S.-H. Kim, T. Tsutsui, Synth. Met. 123 (2001) 43.
[140] J. Zhang, R.-G. Xiong, Z.-F. Chen, X.-Z. You, G.-H. Lee, S.M. Peng, Chem. Lett. (2001) 676.
[141] W. Hu, M. Matsumura, M. Wang, L. Jin, Appl. Phys. Lett. 77 (2000) 4271.
[142] W. Hu, M. Matsumura, M. Wang, L. Jin, Jpn. J. Appl. Phys. 39 (2000) 6445.
[143] G.E. Jabbour, J.-F. Wang, B. Kippelen, N. Peyghambarian, Jpn. J. Appl. Phys. 38 (1999) L1553.
[144] L. Huang, K.-Z. Wang, C.-H. Huang, F.-Y. Li, Y.-Y. Huang, J. Mater. Chem. 11 (2001) 790.
[145] Y. Kawamura, Y. Wada, M. Iwamuro, T. Kitamura, S. Yanagida, Chem. Lett. (2000) 280.
[146] Y. Sato, Semicond. Semimetals 64 (2000) 209.
[147] H. Tokailin, M. Matsuura, H. Higashi, C. Hosokawa, T. Kusumoto, SPIE 1910 (1995) 38.
[148] C. Hosokawa, S. Sakamoto, T. Kusumoto, US Patent 5,389,444 (1995).
[149] T. Kofuji, in: Proceedings of the Electro. J. 6th FPD Seminar, vol. 81, Tokyo, 1999.
[150] C. Hosokawa, H. Higashi, H. Nakamura, T. Kusumoto, Appl. Phys. Lett. 67 (1995) 3853.
[151] TDK, in: Proceedings of the Electro. J. 6th FPD Seminar, vol. 31, Tokyo, 1999.
[152] J. Shi, C.W. Tang, C.H. Chen, US Patent 5,935,721 (1999).
[153] B.X. Mi, Z.Q. Gao, C.S. Lee, S.T. Lee, H.L. Kwong, N.B. Wong, Appl. Phys. Lett. 75 (1999) 4055.
[154] B. Chen, X.H. Zhang, X.Q. Lin, H.L. Kwong, N.B. Wong, C.S. Lee, W.A. Gambling, S.T. Lee, Synth. Met. 118 (2001) 193.
[155] Y.T. Tao, E. Balasubramaniam, A. Danel, B. Jarosz, P. Tomasik, Appl. Phys. Lett. 77 (2000) 1575.
[156] Z. Lu, Q. Jiang, W. Zhu, M. Xie, Y. Hou, X. Chen, Z. Wnag, D. Zou, T. Tsutsui, Synth. Met. 111 (2000) 425.
[157] K. Okumoto, T. Ohara, T. Noda, Y. Shirota, Synth. Met. 121 (2001) 1655.
[158] Y.-H. Kim, D.-C. Shin, S.-H. Kim, C.-H. Ko, H.-S. Yu, Y.-S. Chae, S.-K. Kwon, Adv. Mater. 13 (2001) 1690.
[159] Y. Geng, D. Katsis, S.W. Culligan, J.J. Ou, S.H. Chen, L.J. Rothberg, Chem. Mater. 14 (2002) 463.
[160] L.-H. Chan, H.-C. Yeh, C.-T. Chen, Adv. Mater. 13 (2001) 1637.
[161] Y. Liu, J. Guo, H. Zhang, Y. Wang, Angew. Chem. Int. Ed. 41 (2002) 182.
[162] Y. Ohmori, T. Tsukagawa, H. Kajii, Displays 22 (2001) 61.
[163] Y.T. Tao, E. Balasubramaniam, A. Danel, A. Wisla, P. Tomasik, J. Mater. Chem. 11 (2001) 768.
[164] L.M. Leung, W.Y. Lo, S.K. So, K.M. Lee, W.K. Choi, J. Am. Chem. Soc. 122 (2000) 5640.
[165] J. Yu, Z. Chen, Y. Sakuratani, H. Suzuki, M. Tokita, S. Miyata, Jpn. J. Appl. Phys. 38 (1999) 6762.
[166] M. Wind, U.-M. Wiesler, K. Saalwachter, K. Mullen, H.W. Spiess, Adv. Mater. 13 (2001) 752.
[167] M.A. Baldo, D.F. O'Brien, Y. You, A. Shoustikov, S. Sibley, M.E. Thompson, S.R. Forrest, Nat. London 395 (1998) 151.
[168] D.F. O'Brien, M.A. Baldo, M.E. Thompson, S.R. Forrest, Appl. Phys. Lett. 74 (1999) 442.
[169] M.D. McGehee, T. Bergstedt, C. Zhang, A.P. Saab, M.B. O'Regan, G.C. Bazan, V.I. Srdanov, A.J. Heeger, Adv. Mater. 11 (1999) 1349.
[170] C. Adachi, M.A. Baldo, S.R. Forrest, S. Lamansky, M.E. Thompson, R.C. Kwong, J. Am. Chem. Soc. 78 (2001) 1622.
[171] X. Jiang, A.K.-Y. Jen, B. Carlson, L.R. Dalton, Appl. Phys. Lett. 80 (2002) 713.
[172] M.A. Baldo, S. Lamansky, P.E. Burrows, M.E. Thompson, S.R. Forrest, Appl. Phys. Lett. 75 (1999) 4.
[173] T. Tsutsui, M.-J. Yang, M. Yahiro, K. Nakamura, T. Watanabe, T. Tsuji, Y. Fukuda, T. Wakimoto, S. Miyaguchi, Jpn. J. Appl. Phys. 38 (1999) L1502.
[174] H.Z. Xie, M.W. Liu, O.Y. Wang, X.H. Zhang, C.S. Lee, L.S. Hung, S.T. Lee, P.F. Teng, H.L. Kwong, H. Zheng, C.M. Che, Adv. Mater. 13 (2001) 1245.
[175] M. Ikai, S. Tokito, Y. Sakamoto, T. Suzuki, Y. Taga, Appl. Phys. Lett. 79 (2001) 156.
[176] B.W. D'Andrade, M.A. Baldo, C. Adachi, J. Brooks, M.E. Thompson, S.R. Forrest, Appl. Phys. Lett. 79 (2001) 1045.
[177] R.C. Kwong, L. Michalski, M. Nugent, K. Rajan, T. Ngo, J.J. Brown, M.E. Thompson, S.R. Forrest, in: Proceedings of the 3rd International Conference on EL Mol. Mater. Relat. Phenom. (ICEL-3), O-14, Los Angelos, CA, USA, 5–8 September 2001 (Abstracts).
[178] S. Lamansky, P. Djurovich, D. Murphy, F. Abdel-Razzaq, H.-E. Lee, C. Adachi, P.E. Burrows, S.R. Forrest, M.E. Thompson, J. Am. Chem. Soc. 123 (2001) 4304.

[179] V.V. Grushin, N. Herron, D.D. LeCloux, W.J. Marshall, V.A. Petrov, Y. Wang, Chem. Commun. (2001) 1494.
[180] S. Lamansky, R.C. Kwong, M. Nugent, P.I. Djurovich, M.E. Thompson, Org. Electronics 2 (2001) 53.
[181] Y. Wang, N. Herron, V.V. Grushin, D. LeCloux, V. Petrov, Appl. Phys. Lett. 79 (2001) 449.
[182] P.I. Djurovich, A. Tamayo, M.E. Thompson, in: Proceedings of the 3rd International Conference on EL Mol. Mater. Relat. Phenom. (ICEL-3), P-45, Los Angelos, CA, USA, 5–8 September 2001 (Abstracts).
[183] B.W. D'Andrade, M.E. Thompson, S.R. Forrest, Adv. Mater. 14 (2002) 147.
[184] X. Jiang, Z. Zhang, W. Zhao, W. Zhu, B. Zhang, S. Xu, J. Phys. D: Appl. Phys. 33 (2000) 473.
[185] S. Liu, J. Huang, Z. Xie, Y. Wang, B. Chen, Thin Solid Films 363 (2000) 294.
[186] S. Tasch, E.J.W. List, O. Ekstroem, W. Graupner, G. Leising, P. Schlichting, U. Rohr, Y. Geerts, U. Sherf, K. Muellen, Appl. Phys. Lett. 71 (1997) 2883.
[187] A.W. Freeman, S.C. Koene, P.R.L. Malenfant, M.E. Thompson, J.M.J. Frechet, J. Am. Chem. Soc. 122 (2000) 12385.
[188] J.M. Lupton, I.D.W. Samuel, R. Beavington, P.L. Burn, H. Bassler, Adv. Mater. 13 (2001) 258.
[189] J.P.J. Markham, S.-C. Lo, S.W. Magennis, P.L. Burn, I.D.W. Samuel, Appl. Phys. Lett. 80 (2002) 2645.
[190] I.G. Hill, A. Rajagopal, A. Kahn, Y. Hu, Appl. Phys. Lett. 73 (1998) 662.
[191] H. Ishii, K. Sugiyama, E. Ito, K. Seki, Adv. Mater. 8 (1999) 605.
[192] H. Ishii, K. Seki, IEEE Trans. Electron. Devices 44 (1997) 1295.
[193] H. Ishii, K. Sugiyama, K. Seki, Proc. SPIE 3148 (1997) 228.
[194] C. Shen, A. Kahn, J. Schwartz, J. Appl. Phys. 89 (2001) 449.
[195] N.J. Watkins, L. Yan, Y. Gao, Appl. Phys. Lett. 80 (2002) 4384.
[196] S.T. Lee, X.Y. Hou, M.G. Mason, C.W. Tang, Appl. Phys. Lett. 72 (1998) 1593.
[197] H. Ishii, K. Sugiyama, D. Yoshimura, E. Ito, Y. Ouch, K. Seki, IEEE J. Selected Top. Quantum Electron. 4 (1998) 24.
[198] I.G. Hill, A. Rajagopal, A. Kahn, J. Appl. Phys. 84 (1998) 3236.
[199] T. Shimada, K. Korna, A. Hamaguchi, F.S. Ohuchi, Appl. Phys. Lett. 72 (1998) 1869.
[200] R. Schfaf, C.D. Merritt, L.A. Crisafulli, H. Kafafi, J. Appl. Phys. 86 (1999) 5678.
[201] I.G. Hill, A.J. Makinen, Z.H. Kafafi, J. Appl. Phys. 88 (2000) 889.
[202] K. Seki, N. Hayashi, H. Oji, E. Ito, Y. Ouchi, H. Ishii, Thin Solid Films 393 (2001) 298.
[203] A. Rajagopal, A. Kahn, Appl. Phys. Lett. 84 (1998) 355.
[204] N. Johansson, T. Osada, S. Stafstrom, W.R. Salaneck, V. Parente, D.A. dos Santos, X. Crispin, J.L. Bredas, J. Chem. Phys. 111 (1999) 2157.
[205] Y. Gao, Acc. Chem. Res. 32 (1999) 247.
[206] Y.E. Choong, M.G. Mason, C.W. Tang, Y. Gao, Appl. Phys. Lett. 72 (1998) 2689.
[207] M.G. Mason, C.W. Tang, L.S. Hung, P. Raychaudhuri, J. Madathil, D.J. Giesen, L. Yan, Q.T. Le, Y. Gao, S.T. Lee, L.S. Liao, L.F. Cheng, W.R. Salaneck, D.A. dos Santos, J.L. Bredas, J. Appl. Phys. 89 (2001) 2756.
[208] Q.T. Le, L. Yan, V.-E. Choong, E.W. Forythe, M.G. Mason, C.W. Tang, Y. Gao, Synth. Met. 102 (1999) 1014.
[209] Q.T. Le, M.G. Mason, L. Yan, V.-E. Choong, E.W. Forythe, C.W. Tang, Y. Gao, Proc. SPIE 3628 (1999) 64.
[210] P. He, C.K. Au, Y.M. Wang, L.F. Cheng, C.S. Lee, S.T. Lee, Appl. Phys. Lett. 76 (2000) 1422.
[211] R.Q. Zhang, X.Y. Hou, S.T. Lee, Appl. Phys. Lett. 74 (1999) 1612.
[212] Q.T. Le, L. Yan, Y. Gao, M.G. Mason, D.J. Giesen, C.W. Tang, J. Appl. Phys. 87 (2000) 375.
[213] M.B. Huang, K. McDonald, J.C. Keay, Y.Q. Wang, S.J. Rosenthal, R.A. Weller, L.C. Feldman, Appl. Phys. Lett. 73 (1998) 2914.
[214] M. Stossel, J. Staudigel, F. Steuber, J. Simmerer, A. Winnacker, Appl. Phys. A 68 (1999) 387.
[215] M. Stoßel, J. Staudigel, F. Steuber, J. Blassing, J. Simmerer, A. Winnacker, H. Neuner, D. Metzdorf, H.-H. Johannes, W. Kowalsky, Synth. Met. 111–112 (2000) 19.
[216] C. Shen, I.G. Hill, A. Kahn, Adv. Mater. 11 (1999) 1523.
[217] E.I. Haskal, A. Curioni, P.F. Seidler, W. Andreoni, Appl. Phys. Lett. 71 (1997) 1151.
[218] L.S. Hung, L.S. Liao, C.S. Lee, S.T. Lee, J. Appl. Phys. 86 (1999) 4607.
[219] L.S. Hung, Thin Solid Films 363 (2000) 47.
[220] T. Wakimoto, Y. Fukuda, K. Nagayama, A. Yokoi, H. Nakada, M. Tsuchida, IEEE Trans. Electron. Devices 44 (1997) 1245.
[221] C. Ganzorig, K. Suga, M. Fujihira, Mater. Sci. Eng. B85 (2001) 140.
[222] F. Li, H. Tang, J. Anderegg, J. Shina, Appl. Phys. Lett. 70 (1997) 1233.
[223] H. Tang, F. Li, J. Shinar, Appl. Phys. Lett. 71 (1997) 2560.
[224] Y. Kurosaka, N. Tada, Y. Ohmori, K. Yoshino, Jpn. J. Appl. Phys. 37 (1998) L872.
[225] K.L. Wang, B. Lai, M. Lu, X. Zhou, L.S. Liao, X.M. Ding, X.Y. Hou, S.T. Lee, Thin Solid Films 363 (2000) 178.
[226] L.S. Hung, C.W. Tang, M.G. Mason, Appl. Phys. Lett. 70 (1997) 152.
[227] G.E. Jabbour, V. Kawabe, S.E. Shaheen, J.F. Wang, M.M. Morrell, B. Kippelen, N. Peyghambarian, Appl. Phys. Lett. 71 (1997) 1762.
[228] S.E. Shaheen, G.E. Jabbour, M.M. Morrell, Y. Kawabe, B. Kippelen, N. Peyghambarian, M.-F. Nabor, R. Schlaf, E.A. Mash, N.R. Armstrong, Appl. Phys. Lett. 84 (1998) 2324.

[229] L.S. Hung, C.W. Tang, M.G. Mason, P. Raychaudhuri, J. Madathil, Appl. Phys. Lett. 78 (2001) 544.
[230] L.S. Hung, G. Mason, Appl. Phys. Lett. 78 (2001) 3732.
[231] L.S. Hung, J. Madathil, Adv. Mater. 13 (2001) 1787.
[232] A.N. Krasnov, Appl. Phys. Lett. 80 (2002) 3853.
[233] M. Stoßel, J. Staudigel, F. Steuber, J. Blassing, J. Simmerer, A. Winnacker, Appl. Phys. Lett. 76 (2000) 115.
[234] G.E. Jabbour, B. Kippelen, N.R. Armstrong, N. Peyghambarian, Appl. Phys. Lett. 73 (1998) 1185.
[235] L.S. Hung, R.Q. Zhang, P. He, G. Mason, J. Phys. D: Appl. Phys. 35 (2002) 103.
[236] V.F. Choong, S. Shi, J. Curless, F. So, Appl. Phys. Lett. 76 (2000) 958.
[237] H. Fujikawa, T. Mori, K. Noda, M. Ishii, S. Tokito, Y. Taga, J. Luminescence 87–89 (2000) 1177.
[238] C.H. Lee, Synth. Met. 91 (1997) 125.
[239] M. Matsumura, K. Furukawa, Y. Jinde, Thin Solid Films 331 (1998) 96.
[240] T. Mori, H. Fujikawa, S. Tokito, V. Taga, Appl. Phys. Lett. 73 (1998) 2763.
[241] R. Schlaf, B.A. Parkinson, P.A. Lee, K.W. Nebesny, G. Jabbour, B. Kippelen, N. Peyghambarian, N.R. Armstrong, J. Appl. Phys. 84 (1998) 6729.
[242] H. Heil, J. Steiger, S. Karg, M. Gastel, H. Ortner, H. Von Seggern, M. Stoßel, J. Appl. Phys. 89 (2001) 420.
[243] P. Piromreun, H. Oh, Y. Shen, G.G. Malliaras, J.C. Scott, P.J. Brock, Appl. Phys. Lett. 77 (2001) 2403.
[244] X. Yang, Y. Mo, W. Yang, G. Yu, Y. Cao, Appl. Phys. Lett. 79 (2001) 563.
[245] T.M. Brown, R.H. Friend, I.S. Millard, D.J. Lacey, J.H. Burroughes, F. Cacialli, Appl. Phys. Lett. 79 (2001) 174.
[246] G. Greczynski, M. Fahlman, W.R. Salaneck, J. Chem. Phys. 113 (2000) 2407.
[247] G. Greczynski, M. Fahlman, W.R. Salaneck, J. Chem. Phys. 114 (2001) 8628.
[248] T.M. Brown, R.H. Friend, I.S. Millard, D.J. Lacey, J.H. Burroughes, F. Cacialli, Appl. Phys. Lett. 77 (2000) 3096.
[249] P.A. Cox, The Electronic Structure & Chemistry of Solid, Oxford university Press, Oxford, 1987, p. 231.
[250] F. Nuesch, L.J. Rothberg, E.W. Forsythe, Q.T. Le, Y. Gao, Appl. Phys. Lett. 74 (1999) 880.
[251] Q.T. Le, F. Nuesch, L.J. Rothberg, E.W. Forsythe, Y. Gao, Appl. Phys. Lett. 75 (1999) 1357.
[252] Q.T. Le, E.W. Forsythe, F. Nuesch, L.J. Rothberg, L. Yan, Y. Gao, Thin Solid Films 363 (2000) 42.
[253] C. Ganzorig, K.-J. Kwak, K. Yagi, M. Fujihira, Appl. Phys. Lett. 79 (2001) 272.
[254] R.A. Hatton, S.R. Day, M.A. Chesters, M.R. Willis, Thin Solid Films 394 (2001) 292.
[255] S.F.J. Appleyard, S.R. Day, R.D. Pickford, M.R. Willis, J. Mater. Chem. 10 (2000) 169.
[256] C.C. Wu, C.I. Wu, J.C. Sturm, A. Kahn, Appl. Phys. Lett. 70 (1997) 1348.
[257] M.G. Mason, L.S. Hung, C.W. Tang, S.T. Lee, K.W. Wong, M. Wang, J. Appl. Phys. 86 (1999) 1688.
[258] D.J. Million, I.G. Hill, C. Shen, A. Kahn, J. Schwartz, J. Appl. Phys. 87 (2000) 572.
[259] B. Choi, H. Yoon, H.H. Lee, Appl. Phys. Lett. 76 (2000) 412.
[260] L.S. Hung, US Patent 6208077 (2001).
[261] E.W. Forsythe, M.A. Abkowitz, Y. Gao, J. Phys. Chem. B 104 (2000) 3948.
[262] I.G. Hill, A. Kahn, J. Appl. Phys. 86 (1999) 2116.
[263] Y. Shen, D.B. Jacobs, G.G. Malliaras, G. Koley, M.G. Spencer, A. Ioannidis, Adv. Mater. 13 (2001) 1234.
[264] A. Gyoutoku, S. Hara, T. Komatsu, M. Shirinashihama, H. Iwanaga, K. Sakanoue, Synth. Met. 91 (1997) 73.
[265] H. Jiang, Y. Zhou, B.S. Ooi, Y. Chen, T. Wee, Y.L. Lam, J. Huang, S. Liu, Thin Solid Films 363 (2000) 25.
[266] M. Mizuno, T. Miyamoto, Jpn. J. Appl. Phys. 39 (2000) 1849.
[267] A. Andersson, N. Johansson, P. Broms, N. Yu, D. Lupo, W.R. Salaneck, Adv. Mater. 10 (1998) 859.
[268] H. Kim, C.M. Gilmore, J.S. Horwitz, A. Pique, H. Murata, G.P. Kushto, R. Schlaf, Z.H. Kafafi, D.B. Chrisey, Appl. Phys. Lett. 76 (2000) 259.
[269] H. Kim, A. Pique, J.S. Horwitz, H. Murata, Z.H. Kafafi, C.M. Gilmore, D.B. Chrisey, Thin solid Films 377–378 (2000) 798.
[270] J. Zhao, S. Xie, S. Han, Z. Yang, L. Ye, T. Yang, Synth. Met. 114 (2000) 251.
[271] J. Cui, A. Wang, N.L. Edleman, J. Ni, P. Lee, N.R. Armstrong, T.J. Marks, Adv. Mater. 13 (2001) 1476.
[272] R.G. Kepler, P.M. Beeson, S.J. Jacobs, R.A. Anderson, M.B. Sinclair, V.S. Valencia, P.A. Cahill, Appl. Phys. Lett. 66 (1995) 3618.
[273] B.J. Chen, W.Y. Lai, Z.Q. Gao, C.S. Lee, S.T. Lee, W.A. Gambling, Appl. Phys. Lett. 75 (1999) 4010.
[274] T. Yamada, F. Rohlfing, T. Tsutsui, Jpn. J. Appl. Phys. 39 (2000) 1382.
[275] M. Abkowitz, J.S. Facci, J. Rehm, J. Appl. Phys. 83 (1998) 2670.
[276] Y. Shen, D.B. Jacobs, G.G. Malliaras, G. Koley, M.G. Spencer, A. Ioannidis, Adv. Mater. 13 (2001) 1234.
[277] C. Giebeler, H. Antoniadis, D.D.C. Bradley, Y. Shirota, Appl. Phys. Lett. 72 (1998) 2448.
[278] J.C. Scott, G.G. Malliaras, Chem. Phys. Lett. 299 (1999) 115.
[279] Y. Shen, M.W. Klein, D.B. Jacobs, J.C. Scott, G.G. Malliaras, Phys. Rev. Lett. 86 (2001) 3867.
[280] P.E. Burrows, S.R. Forrest, Appl. Phys. Lett. 64 (1994) 2285.
[281] Z. Shen, P.E. Burrows, V. Bulovic, D.Z. Garbuzov, D.M. McCarty, M.E. Thompson, S.R. Forrest, Jpn. J. Appl. Phys. 35 (1996) L401.
[282] P.E. Burrows, Z. Shen, V. Bulovic, D.M. McCarty, S.R. Forrest, J.A. Cronin, M.E. Thompson, J. Appl. Phys. 79 (1996) 7991.
[283] J.-H. Xu, J. Shen, Appl. Phys. Lett. 83 (1998) 2646.

[284] M.A. Baldo, S.E. Forrest, in: Proceedings of the 10th International Workshop on Inorganic & Organic Electroluminescence, Japan, December 2000, p. 53.
[285] M.A. Baldo, S.R. Forrest, Phys. Rev. B 64 (2001) 85201.
[286] H. Tokuhisa, M. Era, T. Tsutsui, S. Saito, Appl. Phys. Lett. 66 (1995) 3433.
[287] J. Bettenhausen, P. Strohriegl, W. Brutting, H. Tokuhisa, T. Tsutsui, J. Appl. Phys. 82 (1997) 4957.
[288] H. Tokuhisa, M. Era, T. Tsutsui, Adv Mater. 10 (1998) 404.
[289] H. Tokuhisa, M. Era, T. Tsutsui, Appl. Phys. Lett. 72 (1998) 2639.
[290] L.-B. Lin, S.A. Jenekhe, P.M. Borsenberger, Appl. Phys. Lett. 69 (1996) 3495.
[291] M. Redecker, D.D.C. Bradley, M. Jandke, P. Strohriegl, Appl. Phys. Lett. 75 (1999) 109.
[292] S. Naka, H. Okada, H. Onnagawa, T. Tsutsui, Appl. Phys. Lett. 76 (2000) 197.
[293] L.S. Hung, in: Proceedings of the 6th International Conference on Solid-State and Integrated-Circuit Technology, Shanghai, October 2001.
[294] J. Kido, T. Matsumoto, Appl. Phys. Lett. 73 (1998) 2866.
[295] H. Nakamura, H. Ikeda, H. Kawamura, H. Higashi, H. Tokailin, K. Fukuoka, C. Hosokawa, T. Kusumoto, SID Digest, 1999, p. 180.
[296] J.S. Huang, M. Pfeiffer, A. Werner, J. Blochwitz, K. Leo, S. Liu, Appl. Phys. Lett. 80 (2002) 139.
[297] G. Parthasarathy, C. Shen, A. Kahn, S.R. Forrest, J. Appl. Phys. 89 (2001) 4986.
[298] M. Pfeiffer, A. Beyer, T. Fritz, K. Leo, Appl. Phys. Lett. 73 (1998) 3202.
[299] X. Zhou, M. Pfeiffer, J. Blochwitz, A. Werner, A. Nollau, T. Fritz, K. Leo, Appl. Phys. Lett. 78 (2001) 410.
[300] M.A. Baldo, D.F. O'Brien, M.E. Thompson, S.R. Forrest, Phys. Rev. B60 (1999) 1442.
[301] M.A. Baldo, M.E. Thompson, S.R. Forrest, Pure Appl. Chem. 71 (1999) 2095.
[302] J. Kido, H. Hayase, K. Hongawa, K. Nagai, K. Okuyama, Appl. Phys. Lett. 65 (1994) 2124.
[303] C. Adachi, M.A. Baldo, S.R. Forrest, J. Appl. Phys. 87 (2000) 8049.
[304] C.J. Liang, T.C. Wong, L.S. Hung, S.T. Lee, Z.R. Hong, W.L. Li, J. Phys. D.: Appl. Phys. 34 (2001) L61.
[305] C. Adachi, M.A. Baldo, S.R. Forrest, S. Lamansky, M.E. Thompson, R.C. Kwong, Appl. Phys. Lett. 78 (2001) 1622.
[306] C. Adachi, M.A. Baldo, S.R. Forrest, M.E. Thompson, Appl. Phys. Lett. 77 (2000) 904.
[307] C. Adachi, R.C. Kwon, P. Djurovich, V. Adamovich, M.A. Baldo, M.E. Thompson, S.R. Forrest, Appl. Phys. Lett. 79 (2001) 2082.
[308] M.A. Baldo, M.E. Thompson, S.R. Forrest, Nature 403 (2000) 750.
[309] P.E. Burrows, S.R. Forrest, T.X. Zhou, L. Michalski, Appl. Phys. Lett. 76 (2000) 2493.
[310] T. Tsutsui, M.-J. Yang, M. Yahiro, K. Nakamura, T. Watanabe, T. Tsuji, Y. Fukuda, T. Wakimoto, S. Miyaguchi, Jpn. J. Appl. Phys. 38 (1999) L1502.
[311] C.F. Madigan, M.-H. Lu, J.C. Sturm, Appl. Phys. Lett. 76 (2000) 1650.
[312] M.-H. Lu, J.C. Sturm, Appl. Phys. Lett. 78 (2001) 1927.
[313] N. Takada, T. Tsutsui, S. Saito, Appl. Phys. Lett. 63 (1993) 2032.
[314] T. Nakayama, Y. Itoh, A. Kakuta, Appl. Phys. Lett. 63 (1993) 594.
[315] A. Dodabalapur, L.J. Rothberg, T.M. Miller, Electron. Lett. 30 (1994) 100.
[316] U. Lemmer, Appl. Phys. Lett. 66 (1995) 1301.
[317] M. Berggren, Synth. Met. 76 (1996) 121.
[318] R.H. Jordan, L.J. Rothberg, A. Dodabalapur, R.E. Slusher, Appl. Phys. Lett. 69 (1996) 1997.
[319] G. Gu, D.Z. Garbuzov, P.E. Burrows, S. Venkatesh, S.R. Forrest, M.E. Thompson, Optics Lett. 22 (1997) 396.
[320] T. Yamasaki, K. Sumioka, T. Tsutsui, Appl. Phys. Lett. 76 (2000) 1243.
[321] H. Yokogawa, M. Yokoyama, J. Non-Crystalline Solids 186 (1995) 23.
[322] T. Tsutsui, M. Yahiro, H. Yokogawa, K. Kawano, M. Yokoyama, Adv. Mater. 13 (2001) 1149.
[323] C. Adachi, K. Nagai, N. Tamoto, Appl. Phys. Lett. 66 (1995) 2679.
[324] F. Steuber, J. Staudigel, M. Stossel, J. Simmerer, A. Winnacker, Appl. Phys. Lett. 74 (1999) 3558.
[325] Z.L. Zhang, X.Y. Jiang, S.H. Xu, T. Nagatomo, O. Omoto, Synth. Met. 91 (1997) 131.
[326] L.S. Hung, L.R. Zheng, G. Mason, Appl. Phys. Lett. 78 (2001) 673.
[327] Z.D. Popovic, S. Xie, N.-X. Hu, A.-M. Hor, D. Fork, G. Anderson, C. Tripp, Thin solid Films 363 (2000) 6.
[328] G. Sakamoto, C. Adachi, T. Koyama, Y. Taniguchi, C.D. Merritt, H. Murata, Z.H. Kafafi, Appl. Phys. Lett. 75 (1999) 766.
[329] X. Zhou, J. He, L.S. Liao, M. Lu, X.M. Ding, X.Y. Hou, X.M. Zhang, X.Q. He, S.T. Lee, Adv. Mater. 12 (2000) 265.
[330] J.C. Sturm, W. Wilson, M. Iodice, IEEE J. Selected Top. Quantum Electron. 4 (1998) 75.
[331] S. Tokito, H. Tanaka, K. Noda, A. Okada, Y. Taga, Appl. Phys. Lett. 70 (1997) 1929.
[332] F. Papadimitrakopoulos, X.-M. Zhang, K.A. Higginson, IEEE J. Selected Top. Quantum Electron. 4 (1998) 49.
[333] H. Aziz, Z.D. Popovic, S. Xie, A.-M. Hor, N.-X. Hu, C. Tripp, G. Xu, Appl. Phys. Lett. 72 (1998) 756.
[334] P. Fenter, F. Schreiber, V. Bulovic, S.R. Forrest, Chem. Phys. Lett. 277 (1997) 521.
[335] Z.Q. Gao, W.Y. Lai, T.C. Wong, C.S. Lee, I. Bello, S.T. Lee, Appl. Phys. Lett. 74 (1999) 3269.
[336] M. Mandai, K. Takada, T. Aoki, T. Fujinami, Y. Nakanishi, Y. Hatanaka, Synth. Met. 91 (1997) 123.
[337] Z.D. Popovic, H. Aziz, C.P. Tripp, N.-X. Hu, A.-M. Hor, G. Xu, in: Proceedings of the SPIE Conference on Organic Light-Emitting Materials and Devices II, San Diego, CA, July 1998, p. 68.

[338] Z.D. Popovic, H. Aziz, N.-K. Hu, A.-M. Hor, G. Kub, Synth. Met. 111–112 (2000) 229.
[339] D. Zou, M. Yahiro, T. Tsutsui, Appl. Phys. Lett. 72 (1998) 2484.
[340] D. Zou, M. Yahiro, T. Tsutsui, Jpn. J. Appl. Phys. 37 (1998) L1406.
[341] I. Shen, D. Wang, E. Langlois, W.A. Barrow, P.I. Green, C.W. Tang, I. Shi, Synth. Met. 111–112 (2000) 233.
[342] Y. Hirose, A. Kahn, V. Aristov, P. Soukiassian, Appl. Phys. Lett. 68 (1996) 217.
[343] S.T. Lee, Z.Q. Gao, L.S. Hung, Appl. Phys. Lett. 75 (1999) 1404.
[344] P.E. Burrows, V. Bulovic, S.R. Forrest, L.S. Sapochak, D.M. McCarty, M.E. Thompson, Appl. Phys. Lett. 65 (1994) 2922.
[345] M. Fujihira, L.-M. Do, A. Koike, E.-M. Han, Appl. Phys. Lett. 68 (1996) 1787.
[346] J. McElvain, H. Antoniadis, M.R. Hueschen, J.N. Miller, D.M. Roitman, J.R. Sheats, R.L. Moon, J. Appl. Phys. 80 (1996) 6002.
[347] H. Aziz, Z.D. Popovict, S. Xie, A.-M. Hor, N.-X. Hu, C. Tripp, G. Xu, Appl. Phys. Lett. 72 (1998) 756.
[348] H. Aziz, Z.D. Popovic, C.P. Tripp, N.-X. Hu, A.-M. Hor, G. Xu, Appl. Phys. Lett. 72 (1998) 2642.
[349] Y.-F. Liew, H. Aziz, N.-X. Hu, S.-O. Chan, G. Xu, Z.D. Popovic, Appl. Phys. Lett. 77 (2000) 2650.
[350] S.F. Lim, L. Ke, W. Wang, S.J. Chua, Appl. Phys. Lett. 78 (2001) 2116.
[351] S.F. Lim, W. Wang, S.J. Chua, Mater. Sci. Eng. B85 (2001) 154.
[352] D. Kolosov, D.S. English, V. Bulovic, P.F. Barbara, S.R. Forrest, M.E. Thompson, J. Appl. Phys. 90 (2001) 3242.
[353] L.-M. Do, M. Oyamada, A. Koike, E.-M. Han, N. Yamamoto, M. Fujihira, Thin Solid Films 273 (1996) 209.
[354] H. Kanai, S. Ichinosawa, Y. Sato, Synth. Met. 91 (1997) 195.
[355] T. Sasaoka, M. Sekiya, A. Yumoto, J. Yamada, T. Hirano, Y. Iwase, T. Yamada, T. Ishibashi, T. Mori, M. Asano, S. Tamura, T. Urabe, SID Digest, 2001, p. 384.
[356] H. Nakada, T. Tohma, Display Devices '98, 1998, p. 29.
[357] S.A. VanSlyke, M. Hettel, M. Boroson, D. Arnold, N. Armstrong, J. Andre, Y. Saito, H. Matsuki, H. Kanno, H. Takahas, IDRC, 2000, C4.
[358] M. Arai, K. Nakaya, O. Onitsuka, T. Inoue, M. Codama, M. Tanaka, H. Tanabe, Synth. Met. 91 (1997) 21.
[359] C. Hosokawa, M. Eida, M. Matsuura, K. Fukuoka, H. Nakamura, T. Kusumoto, Synth. Met. 91 (1997) 3.
[360] C. Hosokawa, M. Matsuura, M. Eida, K. Fukuoka, H. Tokailin, T. Kusumoto, SID, 1998, 29 (1998) 7.
[361] Y. Fukuda, S. Miyaguchi, S. Ishizuka, T. Wakimoto, J. Funaki, H. Kubota, T. Watanabe, H. Ochi, T. Sakamoto, M. Tsuchida, I. Ohshita, H. Nakada, T. Tohma, SID, 1999, 31 (1999) 430.
[362] Y. Yamagata, in: Proceedings of the 10th International Workshop on Inorganic and Organic Electroluminescence, Hamamatsu, Japan, 4–7 December 2000, p. 9.
[363] A.D. Cropper, R.S. Cok, R.D. Feldman, in: Proceedings of the SPIE Conference on Organic Light-Emitting Materials and Devices IV, San Diego, USA, 2001, p. 18.
[364] Pioneer Patent EP0 776 147 A1, 1997.
[365] M. Boroson, J. Serbicki, in: Proceedings of the FPD Manufacturing Technology Conference, San Jose, 2–3 February 2000.
[366] Z. Meng, C.H. Chen, C. Qiu, H.S. Kwok, M. Wong, SID Digest, 2001, p. 380.
[367] R.M.A. Dawson, Z. Shen, D.A. Furst, S. Connor, J. Hsu, M.G. Kane, R.G. Stewart, A. Ipri, C.S. King, P.J. Green, R.T. Flegal, S. Pearson, W.A. Barrow, E. Dickey, K. Ping, C.W. Tang, S.A. VanSlyke, F. Chen, J. Shi, J.C. Strum, M.H. Lu, SID1998 Digest, 1998, p.11.
[368] T.J. King, SID Digest, 2000, p. 406.
[369] S.D. Thesis, et al., IEDM Tech. Digest, 1998, p. 257.
[370] T. Shimoda, et al., IEDM Tech. Digest, 1999, p. 289.
[371] S.A. VanSlyke, A. Pignata, D. Freeman, N. Redden, D. Waters, H. Kikuchi, T. Negishi, K. Kanno, H. Takahashi.
[372] M.E. Thompson, S. Lamansky, P. Djurovich, D. Murphy, F. Abdel-Razzaq, S.R. Forrest, M.A. Baldo, P.E. Burrows, C. Adachi, T.X. Zhou, L. Michalski, K. Rajan, J.J. Brown, SID Digest, 2000, p. 337.
[373] J.K. Mahon, SID Digest, 2001, p. 59.
[374] V. Buiovic, P. Tian, P.E. Burrows, M.R. Gokhale, S.R. Forrest, M.E. Thompson, Appl. Phys. Lett. 70 (1997) 2954.
[375] G. Gu, V. Bulovic, P.E. Burrows, S.R. Forrest, M.E. Thompson, Appl. Phys. Lett. 68 (1996) 2606.
[376] P.E. Burrows, G. Gu, S.R. Forrest, E.P. Vicenzi, T.X. Zhou, J. Appl. Phys. 87 (2000) 3080.
[377] L.S. Hung, J. Madathil, Thin Solid Films 410 (2002) 101.
[378] G. Parthasarathy, P.E. Burrows, V. Khalfin, V.G. Kozlov, S.R. Forrest, Appl. Phys. Lett. 72 (1998) 2138.
[379] L.S. Hung, C.W. Tang, Appl. Phys. Lett. 74 (1999) 3209.
[380] G. Parthasarathy, C. Adachi, P.E. Burrows, S.R. Forrest, Appl. Phys. Lett. 76 (2000) 2128.
[381] L.S. Hung, C.W. Tang, M.G. Mason, P. Raychaudhuri, J. Madathil, Appl. Phys. Lett. 78 (2001) 544.
[382] P.E. Burrows, G. Gu, V. Bulovic, Z. Shen, S.R. Forrest, M.E. Thompson, IEEE Trans. Electron. Devices 44 (1997) 1188.
[383] P.E. Burrows, V. Khalfin, G. Gu, S.R. Forrest, Appl. Phys. Lett. 73 (1998) 435.
[384] J.R. Sheats, Science 277 (1997) 191.
[385] G. Gu, V. Khalfin, S.R. Forrest, Appl. Phys. Lett. 73 (1998) 2399.
[386] G. Gu, G. Parthasarathy, S.R. Forrest, Appl. Phys. Lett. 74 (1999) 305.

[387] G. Parthasarathy, G. Gu, S.R. Forrest, Adv. Mater. 11 (1999) 907.
[388] G.W. Jones, SID Digest, 2001, p. 134.
[389] K. Pichler, W.E. Howard, O. Prache, in: Proceedings of the SPIE Conference on Organic Light-Emitting Materials and Devices III, Denver, CO, 1999, p. 258.
[390] T. Feng, T.A. Ali, E.S. Ramakrishnan, R. Campos, W.E. Howard, in: Proceedings of the SPIE Conference on Organic Light-Emitting Materials and Devices IV, 2001, p. 30.
[391] O. Pache, SID Digest, 2001, p. 514.